

# Lawrence Berkeley National Laboratory

## Recent Work

### Title

CRYSTALLOGRAPHY OF ""LATH MARTENSITE"" AND STABILIZATION OF RETAINED AUSTENITE

### Permalink

<https://escholarship.org/uc/item/2pw5313w>

### Author

Sarikaya, M.

### Publication Date

1982-10-01



# Lawrence Berkeley Laboratory

UNIVERSITY OF CALIFORNIA

## Materials & Molecular Research Division

RECEIVED  
LAWRENCE  
BERKELEY LABORATORY

OCT 7 1982

LIBRARY AND  
DOCUMENTS SECTION

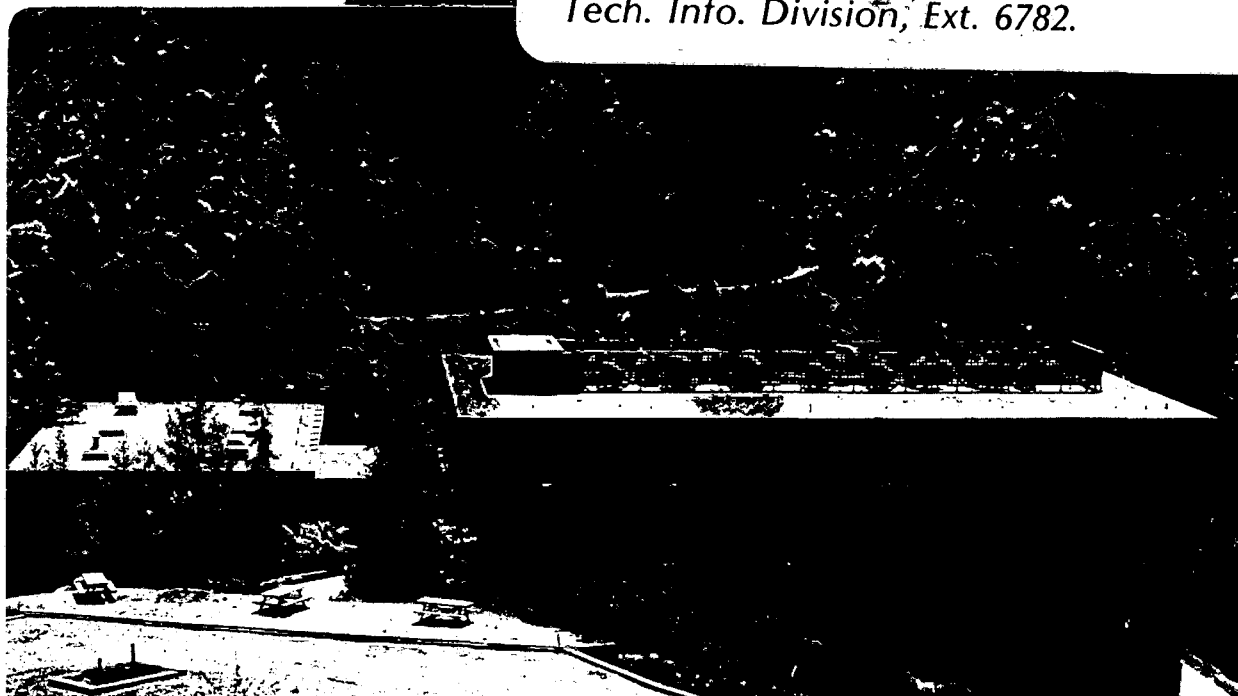
CRYSTALLOGRAPHY OF "LATH MARTENSITE" AND  
STABILIZATION OF RETAINED AUSTENITE

Mehmet Sarikaya  
(Ph. D. thesis)

October 1982

### TWO-WEEK LOAN COPY

*This is a Library Circulating Copy  
which may be borrowed for two weeks.  
For a personal retention copy, call  
Tech. Info. Division, Ext. 6782.*



LBL-15111  
c.2

## DISCLAIMER

This document was prepared as an account of work sponsored by the United States Government. While this document is believed to contain correct information, neither the United States Government nor any agency thereof, nor the Regents of the University of California, nor any of their employees, makes any warranty, express or implied, or assumes any legal responsibility for the accuracy, completeness, or usefulness of any information, apparatus, product, or process disclosed, or represents that its use would not infringe privately owned rights. Reference herein to any specific commercial product, process, or service by its trade name, trademark, manufacturer, or otherwise, does not necessarily constitute or imply its endorsement, recommendation, or favoring by the United States Government or any agency thereof, or the Regents of the University of California. The views and opinions of authors expressed herein do not necessarily state or reflect those of the United States Government or any agency thereof or the Regents of the University of California.

CRYSTALLOGRAPHY OF "LATH MARTENSITE"  
AND STABILIZATION OF RETAINED AUSTENITE

Mehmet Sarikaya  
(Ph.D. Thesis)

Lawrence Berkeley Laboratory  
University of California  
Berkeley, California 94720

October 1982


This work was supported by the Director, Office of Energy Research,  
Office of Basic Energy Science, Material Science Division of the  
U.S. Department of Energy under Contract No. DE-AC03-76SF00098.

CRYSTALLOGRAPHY OF "LATH MARTENSITE"  
AND STABILIZATION OF RETAINED AUSTENITE

Mehmet Sarikaya

Ph.D.

Materials Science and  
Mineral Engineering

  
Professor G. Thomas  
Chairman of Committee

ABSTRACT

Transmission electron microscopy has been used to study the morphology and the crystallography of "lath martensite" in low and medium carbon steels in the "as-quenched" and 200°C tempered conditions. The steels have microduplex structures of dislocated lath martensite ( $a < b \ll c$ ,  $a \approx 0.5 \mu\text{m}$ ) with fairly parallel boundaries and continuous thin films ( $\sim 200 \text{ \AA}$ ) of retained austenite at the lath interfaces. Stacks of laths (i.e., single crystals of martensite) form the packets which are derived from different  $\{111\}_A$  variants of the same austenite grain. The existence of residual parent austenite enables one to perform microdiffraction experiments with small electron beam spot sizes to directly determine the orientation relationships (OR) between austenite and martensite. All three most commonly observed ORs, namely Kurdjumov-Sachs, Nishiyama-Wassermann, and Greninger-Troiano, operate within the same sample. This is

attributed to the increase in the number of variants available during the nucleation process where the nucleation units are individual martensite laths. Relative orientations of the laths change from a low angle boundary ( $1-10^\circ$  rotations perpendicular to  $\langle 110 \rangle_M$ ), to an abrupt change in the orientation by a large rotation, again, about  $\langle 110 \rangle_M$ , which is a common direction in a packet of laths. The habit plane in austenite is  $\{111\}_\gamma$  (parallel to  $\{110\}_\alpha$ ) and the long direction of the laths is in  $\langle \bar{1}11 \rangle_\alpha$  (parallel to  $\langle \bar{1}10 \rangle_\gamma$ ).

Considerable C partitioning into the  $\gamma$ -films ( $\sim 1$  wt%) and to the  $\alpha'/\gamma$ -interface ( $\sim 2$  wt%) has been revealed by convergent beam electron diffraction and atom-probe studies. Partitioning largely occurs during the transformation, although some C diffusion into  $\gamma$  is unavoidable during room temperature holding. Austenite, trapped between the laths is stabilized chemically (by lowering the  $M_s$  temperature) and thermally (by pinning the high-C interface probably by clusters). Austenite is highly deformed to accommodate the stresses created as a result of the shear transformation of the surrounding matrix (mechanical stabilization). Consequently, the overall stabilization is determined by the cooperative operation of all of the above mechanisms.

CRYSTALLOGRAPHY OF "LATH MARTENSITE" AND  
STABILIZATION OF RETAINED AUSTENITE

TABLE OF CONTENTS

	Page
ABSTRACT . . . . .	1
1. GENERAL INTRODUCTION . . . . .	1
2. EXPERIMENTAL MATERIALS AND METHODS . . . . .	4
2.1. ALLOY COMPOSITIONS AND HEAT TREATMENTS . . . . .	4
2.2. SPECIMEN PREPARATION AND THINNING . . . . .	5
2.2.1. Thin Foils for TEM . . . . .	5
2.2.2. Dipping Technique for CBED . . . . .	6
2.2.3. Specimen Preparation for FIM-AP Analysis . . . . .	7
3. PART-I: MORPHOLOGY AND CRYSTALLOGRAPHY OF LATH MARTENSITE IN LOW ALLOY LOW CARBON STEELS . . . . .	11
3.1. BACKGROUND INFORMATION AND INTRODUCTION . . . . .	11
3.2. MORPHOLOGY AND SUBSTRUCTURE . . . . .	14
3.2.1. Morphology . . . . .	14
3.2.2. Substructure . . . . .	14
3.2.3. Retained Austenite . . . . .	19
3.3. CRYSTALLOGRAPHY . . . . .	22
3.3.1. Relative Orientation of Packets . . . . .	22
3.3.2. Relative Orientations of Adjacent Laths in a Packet . . . . .	26
3.3.3. Determination of Orientation Relationships between Martensite and Austenite . . . . .	45
3.3.4. Habit Plane Analysis . . . . .	57

	Page
3.4. SUMMARY AND DISCUSSION . . . . .	60
3.4.1. Morphology of Lath Martensite . . . . .	60
3.4.2. Crystallography . . . . .	61
3.4.3. Formation of Laths . . . . .	69
3.5. CONCLUSIONS . . . . .	71
4. PART-II: THIN FILM RETAINED AUSTENITE . . . . .	73
4.1. INTRODUCTION . . . . .	73
4.2. TEM IDENTIFICATION AND THE OCCURRENCE OF RETAINED AUSTENITE . . . . .	75
4.3. CHEMICAL ANALYSIS OF RETAINED AUSTENITE . . . . .	81
4.3.1. Experimental Techniques . . . . .	81
4.3.2. Converging Beam Electron Diffraction- Austenite Lattice Parameter Measurement . . . . .	87
4.3.3. Measurements of Solute Partitioning into Retained Austenite by Field Ion Microscopy-Atom Probe Analysis . . . . .	94
4.4. DISCUSSIONS - MECHANISMS OF AUSTENITE STABILIZATION . . . . .	113
4.4.1. Chemical Stabilization . . . . .	115
4.4.2. Thermal Stabilization . . . . .	122
4.4.3. Mechanical Stabilization . . . . .	125
4.4.4. Summary . . . . .	128
4.5. MECHANISMS OF DECOMPOSITION OF RETAINED AUSTENITE . . . . .	129
4.5.1. Mechanical Instability . . . . .	129
4.5.2. Thermal Instability . . . . .	134
4.6. CONCLUSIONS . . . . .	143
5. APPENDICES . . . . .	145



	Page
5.1. APPENDIX-1: A COMPUTER PROGRAM TO PLOT STEREOGRAPHIC PROJECTION AND COMPOSITE STEREOGRAPHIC PROJECTIONS FOR MARTENSITE AND AUSTENITE HAVING DIFFERENT ORIENTATION RELATIONSHIPS . . . . .	145
5.2. APPENDIX-2: VARIATION OF THE LATTICE PARAMETERS OF AUSTENITE AND MARTENSITE WITH ALLOYING ADDITIONS AND AN ATTEMPT TO MEASURE LATTICE PARAMETER OF MARTENSITE BY CBED TECHNIQUE . . . . .	147
5.3. APPENDIX-3: CRITICAL DIFFUSION TIME DURING LATH GROWTH AND THE PREDICTION OF THE GROWTH RATE OF MARTENSITE LATHS . . . . .	151
5.4. APPENDIX-4: DIFFUSION COEFFICIENTS OF CARBON IN MARTENSITE AND AUSTENITE . . . . .	154
5.5. APPENDIX-5: EFFECTIVE DIFFUSION DISTANCE FOR CARBON DURING THE TRANSFORMATION WITHIN $M_s - M_f$ RANGE . . . . .	157
5.6. APPENDIX-6: INTERSTITIAL ATOM-DISLOCATION INTERACTION . . . . .	159
6. ACKNOWLEDGEMENTS . . . . .	161
7. REFERENCES . . . . .	162

## 1. GENERAL INTRODUCTION

During cooling many metallic and nonmetallic systems undergo martensitic transformations, i.e., shear of the crystal lattice of a parent phase, stable at high temperatures, to form a new phase as the first or final step towards restoring thermodynamic equilibrium. Although martensite formation is one of the most important phenomenon in Materials Science<sup>(1-4)</sup> and has been widely studied, the details of the mechanisms are still not well understood because the resulting structural features and other characteristics are almost always investigated after the transformation is completed.<sup>(1-6)</sup>

Martensitic transformation, defined as a first order solid-state structural change which is displacive and diffusionless, is dominated in kinetics and morphology by the strain energy arising from the shear-like displacements.<sup>(1-4,8)</sup> The transformation occurs in numerous metallic<sup>(6,9,10)</sup> and ceramic<sup>(11-13)</sup> systems and bears great scientific and technological significance.<sup>(1,2)</sup> The reaction involves the nucleation of the new phase and growth of it into the parent phase during cooling from a high temperature<sup>(6,9,10,14-18)</sup> or during isothermal holding.<sup>(14,19-22)</sup> Since no atomic diffusion is involved<sup>(7)</sup> the parent and product phases have basically the same composition.<sup>(1-7)</sup> The reaction, which usually involves volume change<sup>(23,24)</sup> occurs by shear on certain planes and

directions in each crystal by the cooperative movement of the atoms along the semi-coherent interface. (1,25) As a result parent and product crystals have fixed orientation relationships (26,28) including an unrotated and undistorted plane in the parent phase (habit plane) which is one of the essential features of the crystallography. (1,6,14,27) Another characteristic of the reaction is that the product, unless subsequent decomposition to still other phases has occurred, will transform back to parent phase upon heating ideally without any hysteresis. (19,21)

Martensitic transformation was first recognized in steel systems and the term "martensite" was given to the phase formed in quenched carbon steels. (29) Most subsequent investigations have been performed on steel alloy systems. (4-6,14-18) In general, two types of martensites are classified in steels; (6,13,18,30,31) "plate" and "lath" martensites. Early studies have concentrated on the formation, (16,19-22,32) morphology, (14-18,30-34) crystallography (4,6,15,17,26,31) kinetics (32,36-38) and other properties of plate martensites. (9,10) On the other hand lath martensites attracted little attention until recent years (15,18,39,40) presumably because of the high  $M_s$  temperature and lack of distinctive microstructure as compared to the characteristic "lenticular" plates of martensites which form in alloys with low  $M_s$  temperature. The small size of the average individual martensite laths compounds the difficulty of

morphological and crystallographical studies. The advancement of transmission electron microscopy (TEM) has accelerated studies of the lath martensite which occurs in many technologically important steels. (15,17,30,34,35,39,40)

Part-I of this investigation was devoted to the identification and classification of the important morphological and crystallographic features in a series of low and medium carbon-low alloy steels by transmission electron microscopy. In Part-II thin film retained austenite, which has been found to be an integral part of lath martensitic structures, was studied in detail and the mechanisms of stabilization was examined in order to understand its occurrence and clarify its behavior during tempering or deformation.

## 2. EXPERIMENTAL MATERIALS AND METHODS

### 2.1. ALLOY COMPOSITIONS AND HEAT TREATMENTS

The experimental alloys and most research techniques used in this investigation have been developed at Berkeley during a long range program of "alloy design" of steels for very demanding structural applications. (40-45)

Steels with  $M_s$  temperatures well above room temperature contain carbon content between 0.06 to 0.3 wt% with a total alloy content around 5.0 wt% (see Table 1).

Table 1

<u>Alloy</u>	<u>Alloying Elements (wt%)</u>	<u><math>M_s</math> (°C)</u>
1	0.06C + 2Si	470
2	0.10C + 2Si	450
3	0.17C + 2Si	420
4	0.3C + 3Cr + 2Mn + 0.5Mo	320
5	0.3C + 3Cr + 2Ni + 0.5Mo	340

Samples with dimensions 2mm (or 10mm) by 15mm by 10mm were austenitized at 1100°C for one hour in a vertical tube furnace in a dynamic argon atmosphere to prevent decarburization and quenched into oil or iced brine. Some samples were tempered and quenched in water.

## 2.2. SPECIMEN PREPARATION AND THINNING

2.2.1. Thin Foils for TEM. Foils for transmission electron microscopy (TEM) studies were prepared by a "twin-jet" electropolishing technique. Approximately 15mil slices were "dimet" cut from the heat treated samples and then chemically thinned to a thickness of 4 to 5mils in a 4-8 vol% HF (hydrofluoric acid)--CH<sub>3</sub>COOH (acetic acid) solution in a magnetically stirred bath. Standard 3.0mm discs were punched out by "spark-cutting" and thinned to 1.5 to 2.5mils by grinding through a series of SiC papers using extreme precaution not to deform or overheat the samples. The discs were cleaned with acetone and electropolished with "chrome-acetic" solution (75gm Cr<sub>2</sub>O<sub>3</sub> - 400ml CH<sub>3</sub>COOH and 20ml distilled water). It is absolutely necessary to homogenize the solution which can be used many times if stored well by stirring for an hour at 40-50°C. Final polishing was done at 20°C at 40-55 volts and 20-50mA current (below 10°C and above 30°C causes etching). After performance the foil is quickly rinsed with water and then with CH<sub>3</sub>OH (methyl alcohol) and dried with paper. Foils can be stored either wet (in a 200 proof ethyl alcohol) or dry (in a foil holder kept in a dessicator containing dry atmosphere). Some other electropolishing media were also used such as 10% HClO<sub>4</sub> (perchloric acid) in CH<sub>3</sub>-COOH at -20 to -30°C; 60% CH<sub>3</sub>-COOH-8% HClO<sub>4</sub>-32% C<sub>3</sub>H<sub>5</sub>(OH)<sub>3</sub> (glycerol) at 0°C and both at the same current and voltage settings (these solutions are good to use only once).

2.2.2. "Dipping" Technique for CBED. The foils for retained austenite lattice parameter measurements by Convergent Beam Electron Diffraction (CBED) were prepared by a newly developed "dipping" method which produces foils in which the martensite phase is preferentially etched and the retained austenite films are exposed to the perforations. This method uses perchloric acid-acetic acid-glycerol solution at  $-25^{\circ}\text{C}$  with the same voltage and current settings as above similar to the conventional window technique except that no "painting" is involved. The specimen slice (4-5mils thick) is manipulated by a pair of tweezers to change the direction of the sample to give the best irregular thin periphery. After washing in alcohol selected thin regions are cut by a sharp razor blade and carefully placed in "sandwich" grids and stored for further use. (The same slice can be repolished to obtain more foils if necessary.)

Cu (99.999%) and Ni (99.99%) foils, to calibrate lattice parameter measurement by the CBED technique, were electropolished using a 25%  $\text{HNO}_3$  (nitric acid) in  $\text{CH}_3\text{OH}$  (methanol) solution at  $-25$  to  $30^{\circ}\text{C}$  temperature. Cu and Ni samples were originally homogenized (Cu at  $550^{\circ}\text{C}$  and Ni at  $700^{\circ}\text{C}$ ) and furnace cooled to ensure non-defect structure.

Foils were examined by different transmission electron microscopy techniques in different microscopes. Some conventional bright field (BF) and dark field (DF) imaging and weak beam dark field (WBDF) analysis were done using a

Philips EM301 microscope tilting experiments, micro-diffraction and convergent beam electron diffraction (CBED) experiments were performed with a Philips EM400 TEM/STEM instrument which was also equipped with Energy Dispersive X-ray Analyzer (EDX) and Electron Energy Loss Spectrometer (EELS), all operated at 100kV. Field Ion Microscopy (FIM) "tips" were examined in an RCA-1.2meV high voltage microscope at 800 keV.

### 2.2.3. Specimen Preparation for FIM-AP Analysis.

The "two-stage polishing" technique was used to prepare field ion microscope-atom probe (FIM-AP) from specimens 0.5mm x 0.5mm x 15.0mm square pins which were cut from heat treated samples. The first stage uses a "double layer" polishing solution of 25% perchloric acid in acetic acid floating on carbon tetrachloride ( $\text{CCl}_4$ ) to etch a "neck" in the pin. The "necked" pin is polished in 2% perchloric acid in 2-butoxy-ethanol solution until it separates to form 2 tips. Polishing is continued momentarily in order to remove any deformed layers from the specimens. Both stages of polishing are carried out at 25V D.C. at temperatures which do not exceed 20°C. After cleaning, the tips are then further etched in HCl (hydrogen chloride) to obtain a sharp edge (see the optical micrograph in Fig. 37). They are then stored in a desiccator for future use.

Direct chemical analysis of the phases in the structure were made using atom probe microanalyzer<sup>(46)</sup> which consist



of field ion microscopes equipped with time-of-flight mass spectrometers. The two particular AP-instruments (the Oxford one<sup>(46)</sup> and the U.S. Steel one<sup>(47)</sup>) used in this investigation are similar in design.<sup>(56,57)</sup> The experimental conditions with the Oxford instrument will be described here (a full description of the instrument itself can be found elsewhere, e.g., reference 48).

A needle-shaped tip prepared as described above is mounted on a cryogenic (cooled with liquid N<sub>2</sub>) goniometer stage. The 75mm micro-channel plate intensifier and phosphorous screen assembly has a central hole (1.4mm in dia.) which serves as an entrance aperture to the spectrometer flight tube which is typically of 1-2m in length (Oxford uses 1.2385m). A highly magnified image of atoms at special positions on the tip is projected onto a viewing screen using an "imaging gas" (Ar). For chemical analysis, the system is evacuated ( $\sim 10^{-10}$  torr) and high frequency-high voltage pulses applied to the tip (see below for the typical experimental values). Atoms released by "field evaporation" from microconstituents on the selected areas on the tip pass through the probe hole (whose diameter dictates the diameter of the circular area analyzed on the specimen). They struck a particle detector which identifies every arriving ion according to its m/n (mass to charge) ratio from the flight times. The fast digital timer (159.6 MHz) is interfaced with a PDP 11/10 micro-computer which controls

the experimental cycle, records the data, and provides the on-line output of the accumulated spectra during the experiment.

A typical analysis is carried out under the following conditions:

- a system base pressure of  $< 5 \times 10^{-10}$  torr;
- a background pressure during analysis of  $< 10^{-9}$  torr, i.e., with the image gas removed;
- the specimen cryostat cooled in liquid nitrogen;
- an effective data collection aperture of 20 Å;
- a pulse fraction of 15%;
- a pulse repetition rate of 50 Hz;
- ion collection rates of between  $10^{-2}$  and  $10^{-1}$  ions per pulse;
- a neon (or Ar) image gas pressure of  $4 \times 10^{-5}$  torr.

Two general modes of analysis are possible: selected area or random area (sequential analysis). In the first mode specific regions (a retained austenite film or an interface) are chosen, and analyzed on a point-to-point basis. In the sequential mode a random area is chosen and the ions from a column of material parallel to the specimen axis are analyzed (see Fig. 40). The size of the area of analysis (typically 10-30 Å diam. size) is determined by the sequentiality of the aperture and the magnification of the FIM. As material is removed compositional fluctuation of all elements due to, e.g., retained austenite, an interface

region, a carbide, are recorded in turn. The resulting data chain or time series can then be processed using statistical techniques. For example, simple graphing involves taking an average at every 50 ions at each step (see, e.g., Fig. 36). Note that the number of ions can be related to the distance removed from the tip. Simple geometry shows that for a probe diameter of 10 Å, the area covered for the probe corresponds to about 30 atoms in  $\alpha'$  in  $\langle 111 \rangle_{\text{bcc}}$  orientation. Hence at every 30 atoms 2.5 Å planar material is removed from the tip which corresponds to 80 Å thickness for every 1000 ions. Of course this value is very sensitive, and changes depending on the factors such as the crystallographic orientation of the tip, the radius and the shape of tip, etc.

3. PART-I  
MORPHOLOGY AND CRYSTALLOGRAPHY OF  
LATH MARTENSITE IN LOW ALLOY LOW CARBON STEELS

3.1. BACKGROUND INFORMATION AND INTRODUCTION

Two basically distinct morphologies of martensite form in ferrous alloys; (9,10,15-18,49-61) "plate" and "lath" martensites mainly depending on the composition. Plate martensites (with plate size from few to many microns) occur in high alloy, e.g., 25-30% Ni (9,10,34,60) or 12% Mn (9,10,39,53) or high alloy-high carbon (6,9,10,17,33) (or nitrogen) (54,57-59) steels with  $M_s$  temperatures usually below room temperature. Lath martensites are found in steels containing relatively low alloying elements (total 10-15 wt%) or in low alloy (5-8 wt%)-medium carbon (9,10,15,18,33,39-45, 60,61) (or nitrogen) (16,57-59) with  $M_s$  generally  $>200^\circ\text{C}$ .

Extensive studies of the various aspects of plate martensites have clearly shown that the "plates", which form during cooling (5,6,50-60) or isothermal holding, (20-22,32,60) are lenticular with a "midrib" (consisting of extremely fine twins) at the center lying along  $\{225\}$  or  $\{259\}$  austenite planes (habits). (5,6,9,10,15,17,33-36,56) Inhomogeneous shear during the transformation is accomplished by twins which are usually on  $\{112\}_\alpha$  planes in  $\langle 111 \rangle_\alpha$  direction. (14-18,30-34) Therefore both sides of the midrib is consisted of fine (50-200 Å) structural twins. (6,17,18,31,34) Plate martensitic structures contain a considerable amount

of retained austenite (usually 10 vol% or more) as islands between the plates. (6,18,33,62,63) Other crystallographic aspects have been studied in depth (by X-rays) and various orientation relationships between  $\gamma^*$  and  $\alpha'^*$  have been established (specific to certain alloy systems) (49,64-87) and the results discussed in terms of current phenomenological theories of martensite transformation. (68-72) Finally numerous studies of nucleation characteristics (21,36,73-75) and growth kinetics (33,35-38,76-79) have also been conducted. Despite the above-mentioned accomplishments by many distinguished workers in the field inconsistencies still exist so that plate martensite continues to attract much attention.

Lath martensites, despite their wide-spread occurrence in the technologically more important low carbon-low alloy steels, have not attracted comparable attention until recently. (15,18,36,39,40) Even the shape of the laths has not been established clearly. (15,18,33) It is known that all lath martensites form athermally and that  $M_s$  temperatures are usually well above ambient. There is no study of nucleation, only a few dealing with growth kinetics (18,32,33) with most concentrating on the morphological features. (15,18,33,80-82) The inhomogeneous shear occurs by slip so no micro-twins occur and the parallelepiped-shaped laths contain a high density of dislocations. (15,18,39,40) Since no retained

---

\*  $\alpha'$  and M stand for product martensite (bcc or bct) phase and  $\gamma$  and A stand for parent austenite (fcc) phase.

austenite had been found, the crystallographic studies were done indirectly on martensite. (15,33,36,39,83-87) The main concern has been the relative orientations of adjacent laths which were identified to have low angle or high angle boundaries, (33,39,83-87) or they are interpreted as being either in twin related or near twin related orientations. (15,39,83,84) The macroscopic habit plane was identified to be either  $\{123\}_{\alpha}$ , (84,86,87) or near  $\{557\}_{\alpha}$ , (33,84) or  $\{110\}_{\alpha}$ , (85) or else in the vicinity of  $\{111\}_{\gamma}$ . (15,39,40)

In the current investigation emphasis was placed on the characterization, by TEM, of morphological and crystallographic features (relations between the individual martensite units, i.e., laths and the larger units "packets") in the lath martensitic structures in low carbon (0.06 to 0.3 wt%) -low alloy (total about 5 wt%) steels. Since the present alloys contain retained austenite within the structure (45,88) the important aspects of the crystallography of martensite, such as orientation relationships and habit plane analyses, could be established directly on austenite by some recently developed microdiffraction techniques. The results will be explained on the basis of the overall strain minimization which is a characteristic of martensites and dictates both the morphology and the crystallography of this class of phase transformations. (1-6)

### 3.2. MORPHOLOGY AND SUBSTRUCTURE

3.2.1. Morphology. The microstructure of "as-quenched" low C martensitic steels is composed of several distinct components of rather different dimensions and shapes as illustrated in Fig. 1. The largest are the equiaxed prior austenite grains about 100-200  $\mu\text{m}$  diameter in size. They contain irregular packets about 20-35  $\mu\text{m}$  in size which are composed of many "lath"<sup>(15)</sup> martensite crystals. Individual "laths" in each packet have fairly parallel boundaries and are aligned near to a habit plane variant of the parent austenite. In most instances, the "laths" are separated by continuous thin films ( $\sim 200 \text{ \AA}$  thick) of untransformed austenite (retained austenite). "Laths" are single crystals of martensites and have a roughly parallelepiped shape, i.e.,  $a < b \ll c$ . Typical dimensions are  $a = 0.25 - 0.50 \mu\text{m}$ ,  $b = 1-5 \mu\text{m}$  and  $c = 10-30 \mu\text{m}$  for 0.3C alloys. The "laths" were found to be somewhat wider and longer in 0.1C alloys.

3.2.2. Substructure. The substructure of the laths consists mainly of dislocations with a density estimated as  $10^{12} \text{ cm/cm}^3$ . Because of this high dislocation density, it is generally impossible to resolve the individual dislocations (Fig. 2). Hence detailed dislocation analysis could not be done in any of the alloys. The C content of these alloys is too low to produce much microstructural twinning and they were observed on  $\{112\}_\alpha$ , and only locally in the 0.3 wt% C containing alloys.

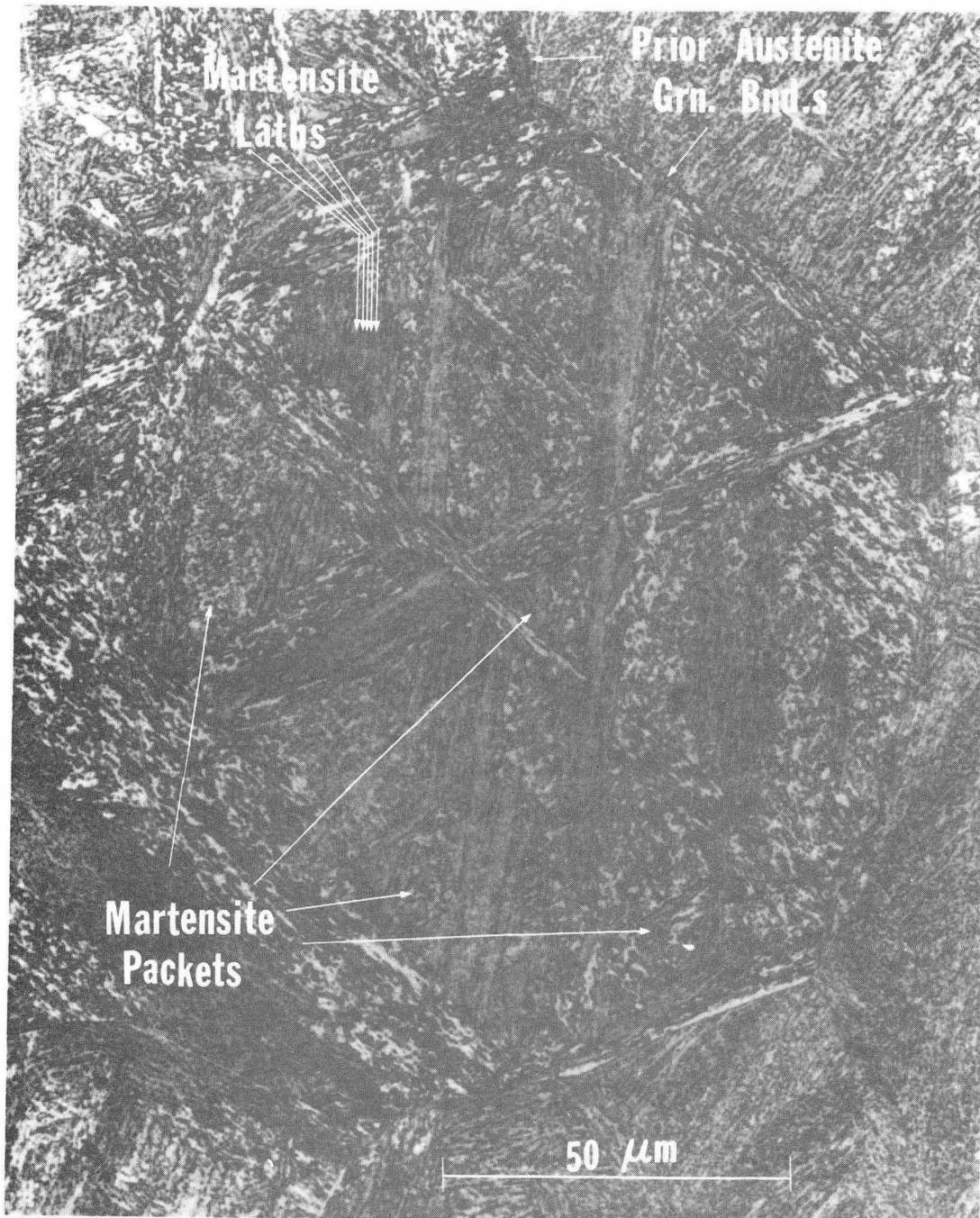


Fig. 1. General microstructure of the alloys at a low magnification. This example by optical microscopy shows the configurations of laths and packets in a single pre-austenite grain.

XBB 821-5



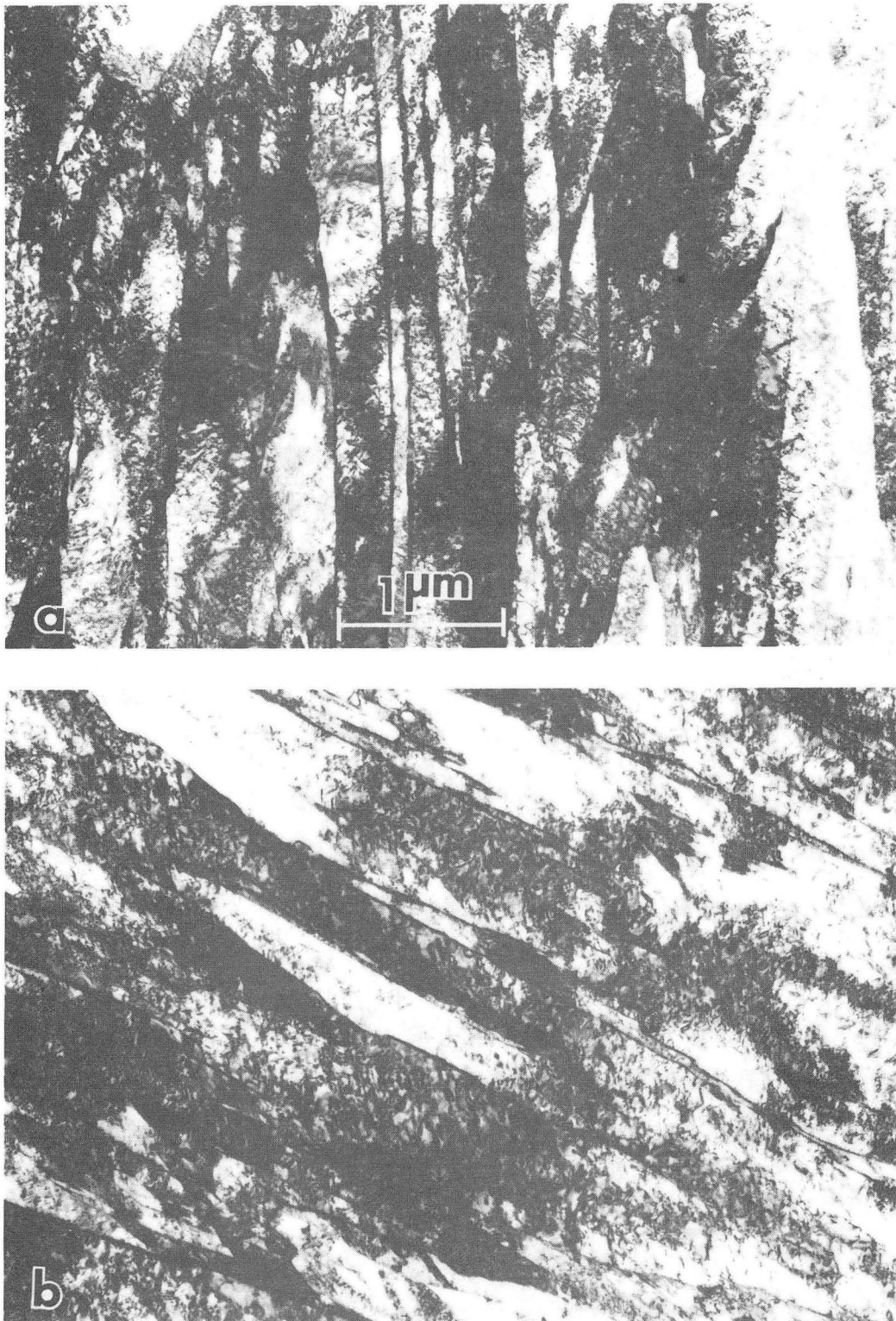


Fig. 2. General microstructure of the alloys in the as-quenched condition. (a) The heavy dislocation density (strain contrast) and the effect of autotempering within the laths are revealed and the lath boundaries are clearly resolved (2 Mn alloy). (b) The same as above in a 2 Ni containing alloy.

It is interesting to compare the two packets of impinging martensite laths, labelled A and B, which appear in Fig. 3. The laths in packet (A) are "twin related"<sup>(89)</sup> (i.e., bright-dark contrast--this is discussed in Section 3.3.2). The presence of regularly-spaced twins in the small laths with retained austenite at their boundaries in packet (B) suggests that packet (A) formed first (since it contains twin-related laths, probably due to autocatalytic nucleation just below  $M_s$ ). The laths in packet (B) probably evolved later and encountered the laths in packet (A). Near the impingement of the two packets, twins formed to accommodate the stresses created in this region.

It is generally noted that twins, usually in every other lath, are similar in both dimensions and separation. Microdiffraction characterization of such areas revealed that the twins are lying on  $\{112\}$  planes of martensite, similar to transformation twins. (15,17,34-35)

The micrograph in Fig. 3 also indicates that some "secondary" laths formed, after impingement, along the growth direction of the original crystals. This configuration suggests that these small crystals of martensite formed after the impingement of the primary laths. Note also that the ends of the laths in packet (B) are curved in this region.

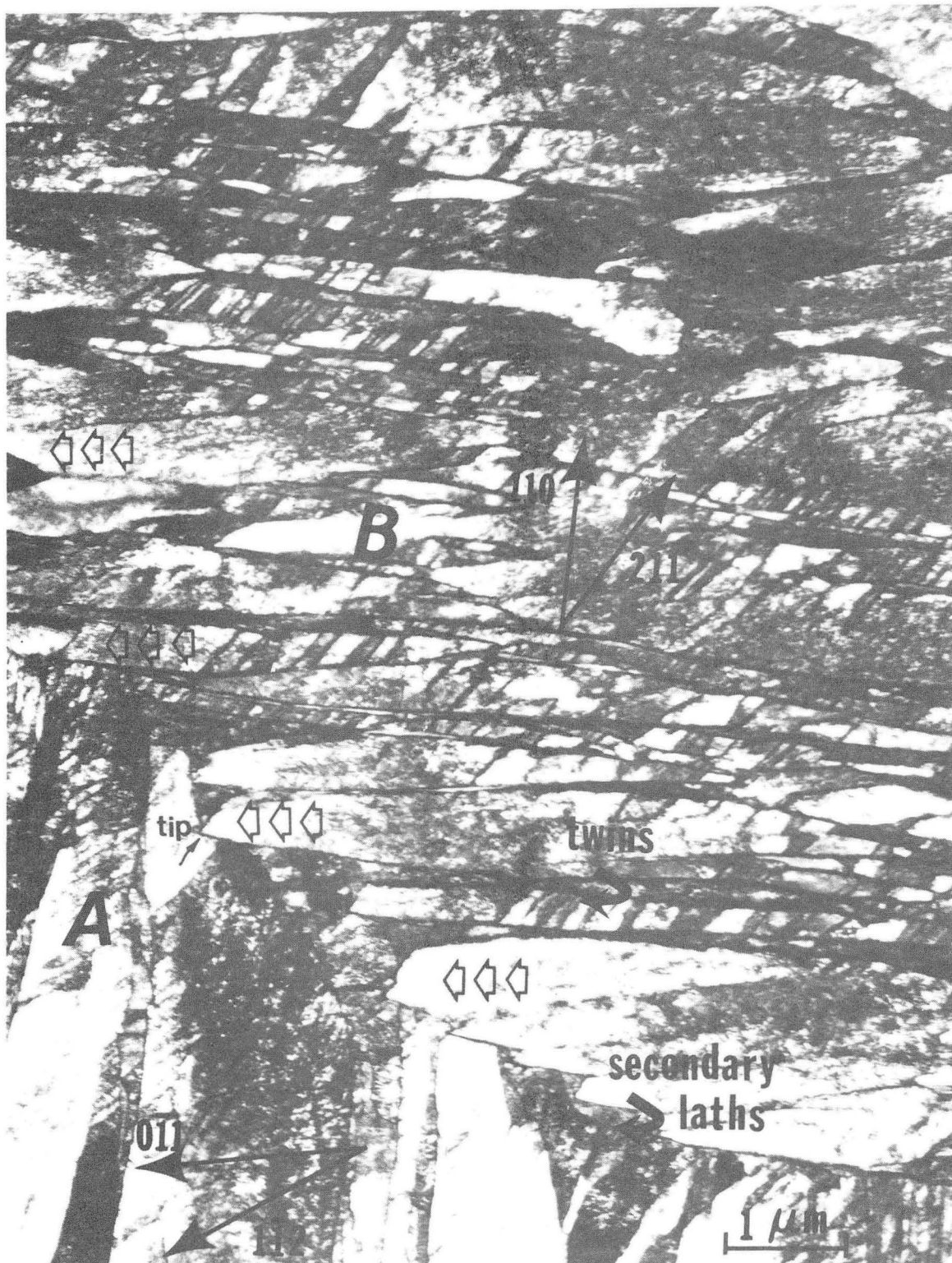


Fig. 3. Details of a packet boundary where the packets A and B intervene (Alloy 4).

XBB 825-4160

This is observed very commonly and must be related to the growth mechanism of the laths (see the discussion section on Page 69).

Since the  $M_s$  temperatures of the alloys are quite high ( $>300^\circ\text{C}$ ), there is time for some C redistribution, i.e., "autotempering"<sup>(15,45)</sup> of the martensite matrix to form C-clusters along dislocations or sometimes they even grow into carbides. These effects can be much more pronounced here than in high C steels with very low  $M_s$  temperatures. The foils studied at high resolution by weak beam dark field (WBDF) technique<sup>(90)</sup> in the air quenched condition show the evidence of such clustering within the martensite. For example in Fig. 4, the dislocations are shown in a heavily strained matrix (a). C-clusters seen in the DF image (b) reveal highly advanced stage of autotempering (may be interpreted as an early stage of  $\epsilon$  or  $\text{Fe}_3\text{C}$  carbide precipitation).

3.2.3. Retained Austenite. An integral part of the microstructure is the generally continuous thin films of untransformed retained austenite, of about 50-450 Å in thickness, at the lath boundaries (Fig. 5). They are trapped between the laths and are highly deformed. Retained austenite is also present at the packet and prior austenite grain boundaries as thin films. However, there is no retained austenite present when the adjacent laths are twin-related (packet B in Fig. 2). Careful microscopy is required to identify these films in this kind of complex structure. The

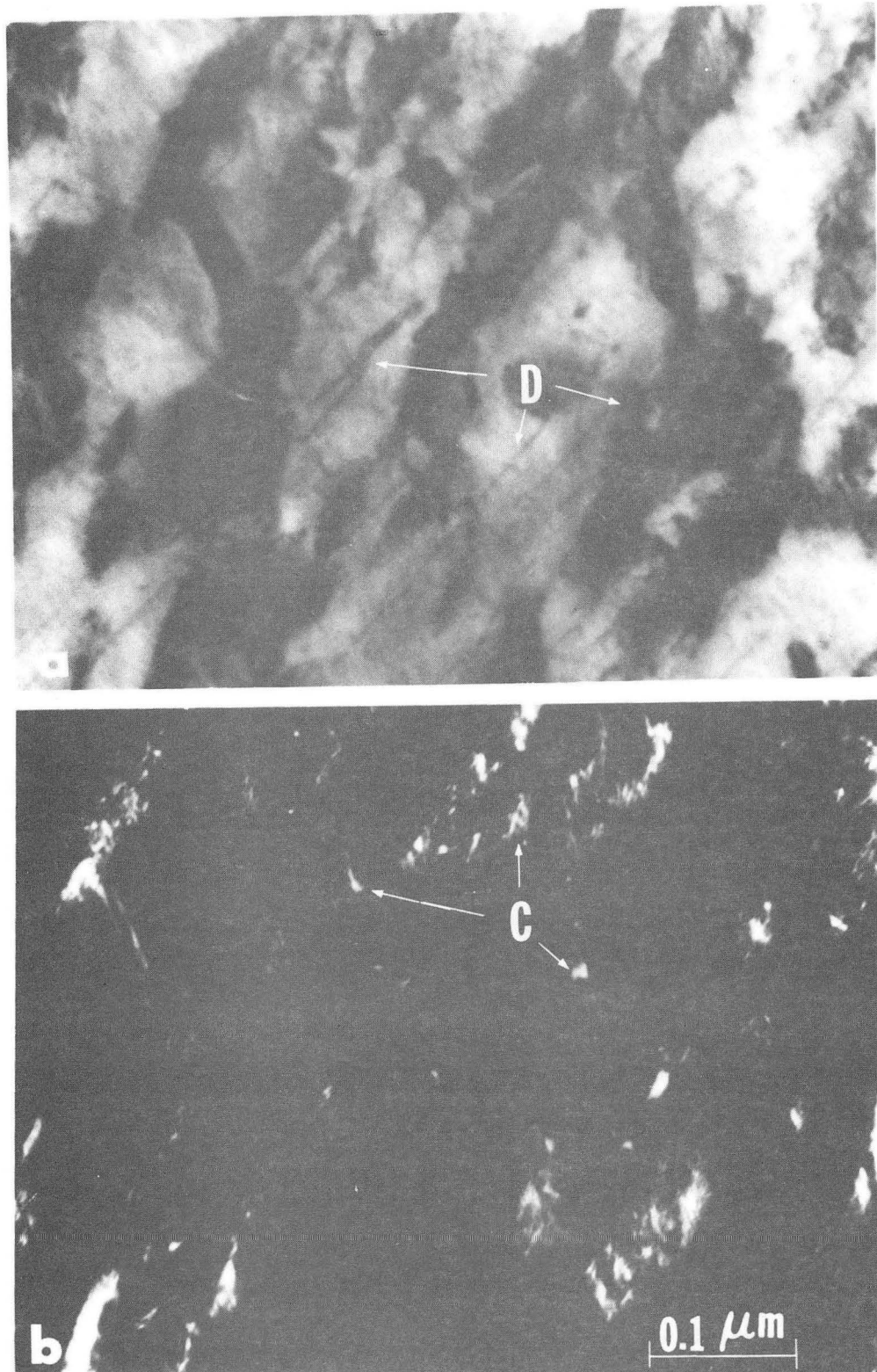


Fig. 4. (a) BF and (b) WBDF images showing C clustering (at an early stage of tempering) at the dislocations within a lath in an as-quenched sample (2-Mn alloy).

XBB 825-4159

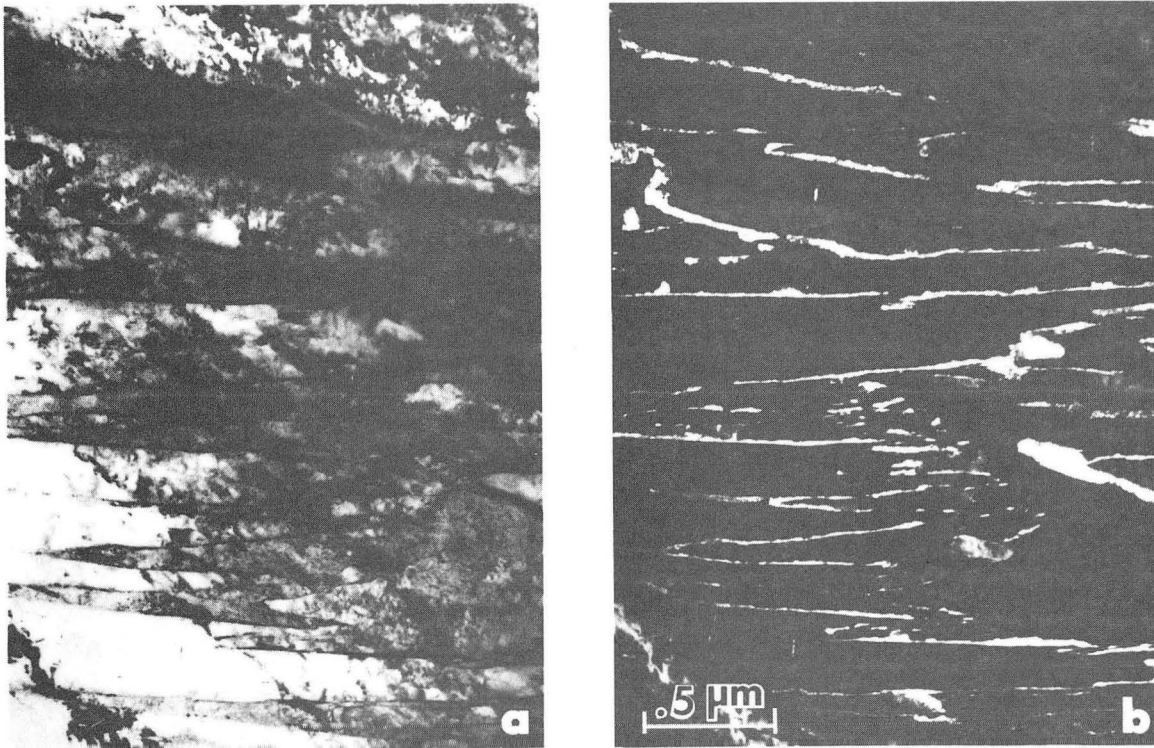


Fig. 5. BF (a) and DF (b) micrographs reveal the retained austenite as thin, continuous films at the lath boundaries (2 Ni alloy in the 200°C tempered condition).

XBB 794-4550

presence of these remnants of the parent phase within the microstructure dictates the morphology and properties of this class of steels. Therefore, a separate detailed section (Part-II) is devoted to the identification and stabilization mechanism of retained austenite.

### 3.3. CRYSTALLOGRAPHY

3.3.1. Relative Orientation of Packets. As noted earlier groups of up to 50 parallel single crystals of martensite, having common growth habits, appear as packets in the TEM. An example is shown in Fig. 6 where the laths in three impinging packets (A, B, and C) all appear close to edge-on. Diffraction patterns taken from the individual packets and from the packet boundaries are shown in the corresponding selected area diffraction, SAD, patterns (A, B, C, D, and E). Although diffraction patterns from the regions A, B, and C indicate a single zone axis (i.e.,  $\langle 111 \rangle_b$ ), the patterns taken from the packet boundary regions D and E give two (111) patterns slightly rotated about  $[111]_b$  direction with respect to each other. Fig. 7(b) shows another cubic (111) SAD pattern containing reflections which again suggest some slight misorientation. In previous studies this was attributed<sup>(33,83,84)</sup> to small angle boundaries between the adjacent laths in a packet. However, a detailed analysis shows that the reflections in this diffraction pattern come from packets with laths "end-on" (laths 1) and "edge-on" (laths 2) in the micrograph. Hence region 2 is not a "single"

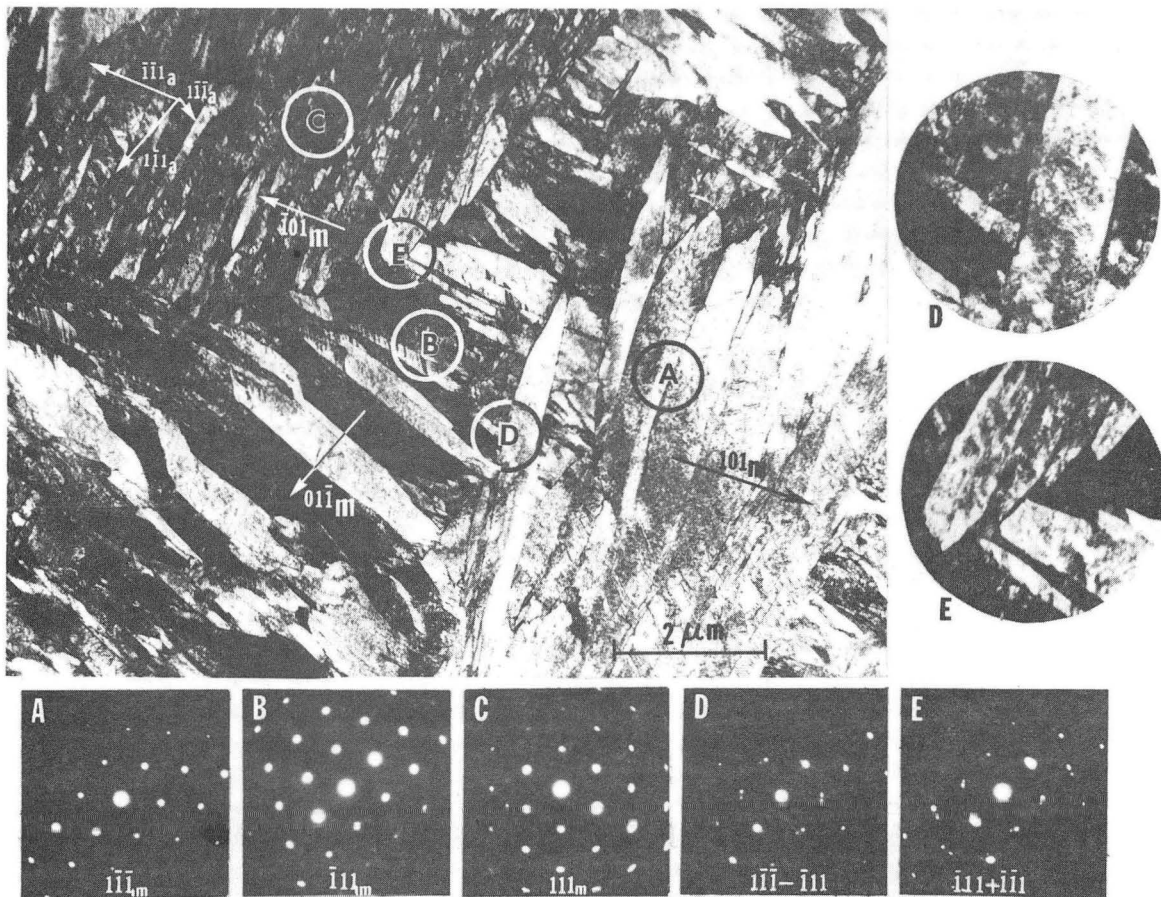


Fig. 6. BF image shows three impinging packets A, B, and C in an 0.3C alloy. The microdiffraction patterns A to E, taken from the corresponding regions in the image, reveal single (A to C) or two superimposed  $\langle 111 \rangle_{\alpha}$  patterns (D and E) (Alloy 4).

XBB 810-11423



lath. It has been ascertained that the laths (1) have a  $\{111\}_A$  habit and laths (2) a  $\{1\bar{1}\bar{1}\}_A$  habit. Similarly in Fig. 6, laths A have a  $\{1\bar{1}\bar{1}\}_A$  habit; laths B have a  $\{\bar{1}11\}_A$  habit and laths C have a  $\{\bar{1}\bar{1}1\}_A$  habit. This is a rotation around a vector normal to the plane of the foil, i.e.,  $\langle 110 \rangle_A$ , or  $\langle 111 \rangle_M$ . In superimposed SAD patterns (Figs. 6D and E, and Fig. 7b), the  $\langle 110 \rangle$  rel-vectors corresponding to different packets are then expected to be separated by a  $10.54^\circ$  rotation (refer to the analysis in Fig. 7c). The measured separation ( $10^\circ$ ) in the diffraction patterns agrees quite well with this prediction (see the SADP's in Figs. 6 and 7). There are four different  $\{111\}$  planes in the austenite lattice. Hence, four or more variants of packets can operate in a single austenite grain (some variants may also be repeated in different parts of the grain). Correspondingly, four or more packets may fill up the austenite grains, e.g., in Fig. 6 three separate  $\{111\}$  variants of austenite (namely  $(\bar{1}\bar{1}1)$ ,  $(\bar{1}11)$ , and  $(1\bar{1}\bar{1})$ ) are present (corresponding to  $(101)$ ,  $(01\bar{1})$ , and  $(\bar{1}01)$  of martensite, respectively).

The large strains (dilatational and principal shear strain) created during the austenite to martensite transformation<sup>(1,2,4,6)</sup> in steels are accommodated by some means such as shearing (slip or twinning) in martensite, various degrees of rotations of adjacent laths, and deformation of retained austenite in the lath boundaries (to be discussed

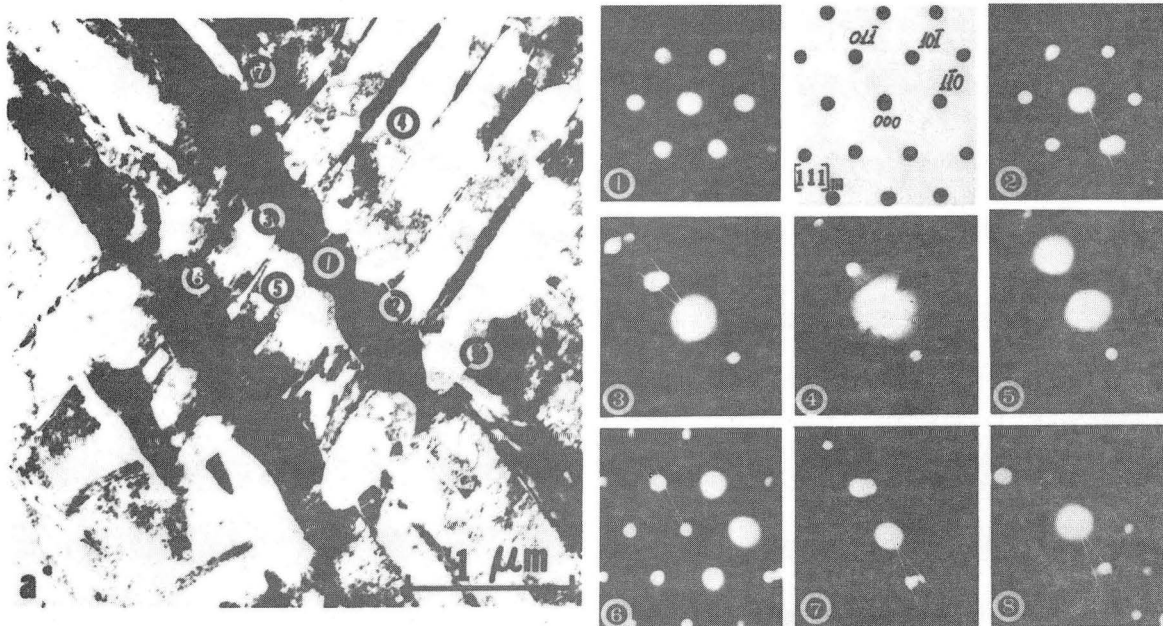
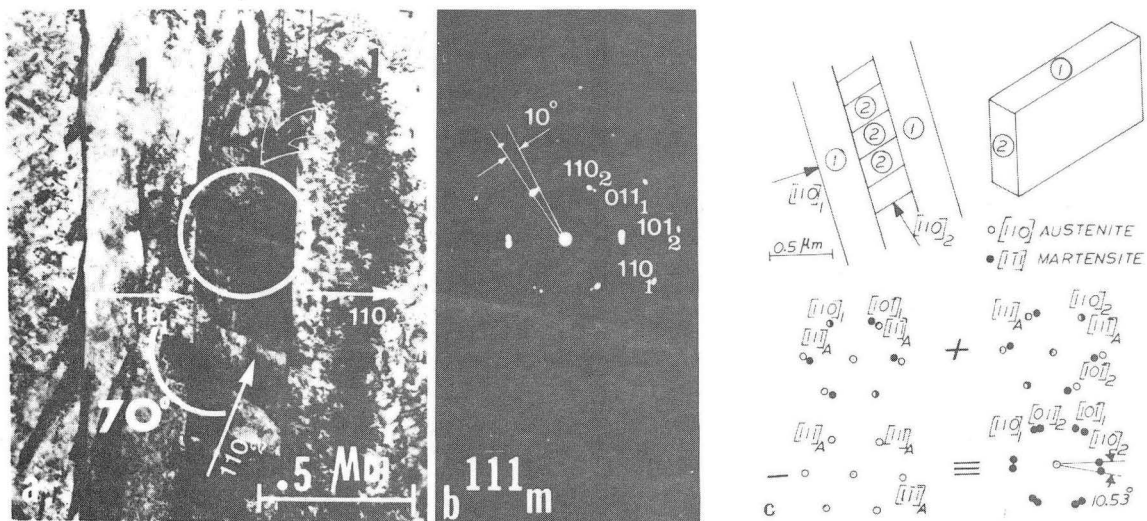


Fig. 7. (a) BF image and (b) the SAD pattern taken from the encircled region in (a). Note that the laths in packet (2) are in end-on configuration (i.e., two shorter dimensions, "a" and "b", are projected). (c) shows a model of the image (a) and gives the analysis of the diffraction pattern (b) (Alloy 4, above).

Fig. 8. BF image (a) and the portions of the microdiffraction patterns corresponding to the regions indicated by (1) to (8). Notice the zig-zag interfaces (Alloy 2, below).

XBB 810-1149

later) in addition to stress relieving process inherent in the different transformation variants. Fig. 8a is a unique example where at least six packets are so oriented with respect to each other in such a small region. As shown in this figure, even a single lath can correspond to a packet (e.g., lath (1)). This is confirmed by microdiffraction\* patterns which show either a single  $\langle 111 \rangle_M$  pattern (1,4,5), or superimposed  $\langle 111 \rangle_M$  patterns (2,3,6,7 and 8) rotated  $\sim 70^\circ$  (or  $110^\circ$ ) according to the site on which the electron probe was placed.

### 3.3.2. Relative Orientations of Adjacent Laths in a Packet

(i) Twin related laths: This less frequently observed relative orientation between adjacent laths is one in which the laths on either side of the boundary have approximately opposite orientations, i.e., are rotated + and  $-90^\circ$  with respect to their common  $\langle 110 \rangle$  axis and hence are "twin related." The situation is also observed in higher carbon alloys and an example is shown in Fig. 9. Here in the central packet B the laths are twin related (dark-bright contrast). All microdiffraction patterns from the individual laths have nearly the same type of symmetries, i.e., all  $\langle 111 \rangle$  patterns

---

\* A microdiffraction pattern (91) is formed by placing an electron beam of certain size (usually 500 Å or smaller in diameter) on a region of interest, while an SAD pattern is formed by placing a selected area aperture on a region and limiting the diffraction coming from that certain area (usually 0.5  $\mu\text{m}$  or larger).

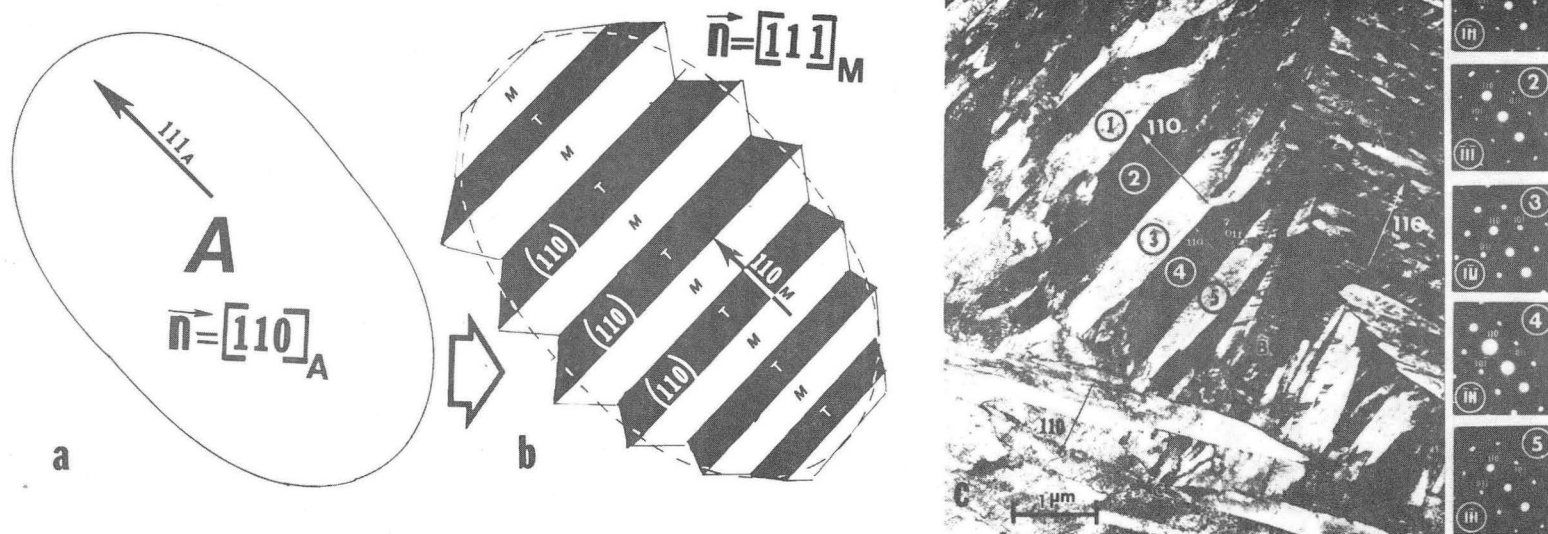


Fig. 9. (a) A section from an austenite grain before the transformation has occurred ( $\vec{n}$  is electron beam direction). (b) The same grain in (a) after the martensitic transformation, showing the arrangements of twins (T) and martensite (M) produced from  $\{111\}_A$  variant of austenite. (c) A TEM micrograph showing a packet B which contains twin related laths. Insets are the SAD patterns in  $\langle 111 \rangle_M$  taken from the individual laths (1) through (5).

XBB 824-3499

(1 through 5) but with reflections having different intensities. The laths have their (110) faces parallel to each other. Therefore, the twin plane is  $(110)_\alpha$  and the direction is  $[\bar{1}\bar{1}1]_\alpha$ , which means laths are in  $[1\bar{1}1]$  and  $[\bar{1}\bar{1}\bar{1}]$  zone axis orientations, successively. With the beam exactly on a zone axis, the laths should appear to give the same contrast, but for a very small misorientation ( $0.5^\circ$  as in this example) successive laths appear bright and dark due to the phase contrast.

(ii) Parallel laths: This commonly observed situation stimulated the interesting hypothesis<sup>(15,33,39,40,61,81-84)</sup> that in a group of parallel laths every successive lath is further rotated around this common  $\langle 110 \rangle_M$  axis, after "n" laths in a " $\pi$ -rotation" results<sup>(40)</sup> (e.g., in the case of twin related laths n is, of course, two, i.e., the rotation is completed by two adjacent laths). This rotation is not a physical one but results as a consequence of the principal shear vector assuming different variants of austenite. This hypothesis was advanced as it minimizes the strain created during the nucleation of individual martensite units over a relatively small number of laths in a packet. For example, when 4 or 5 laths gave all  $\langle 111 \rangle_M$  diffraction patterns, it was interpreted to mean that each individual lath was in a different  $\langle 111 \rangle_M$  zone axis (z.a.) orientation, e.g.,  $\langle \bar{1}\bar{1}\bar{1} \rangle$ ,  $\langle \bar{1}\bar{1}1 \rangle$ ,  $\langle 1\bar{1}\bar{1} \rangle$ , etc., around the common  $\langle 110 \rangle_M$  axis (e.g., see Fig. 10).

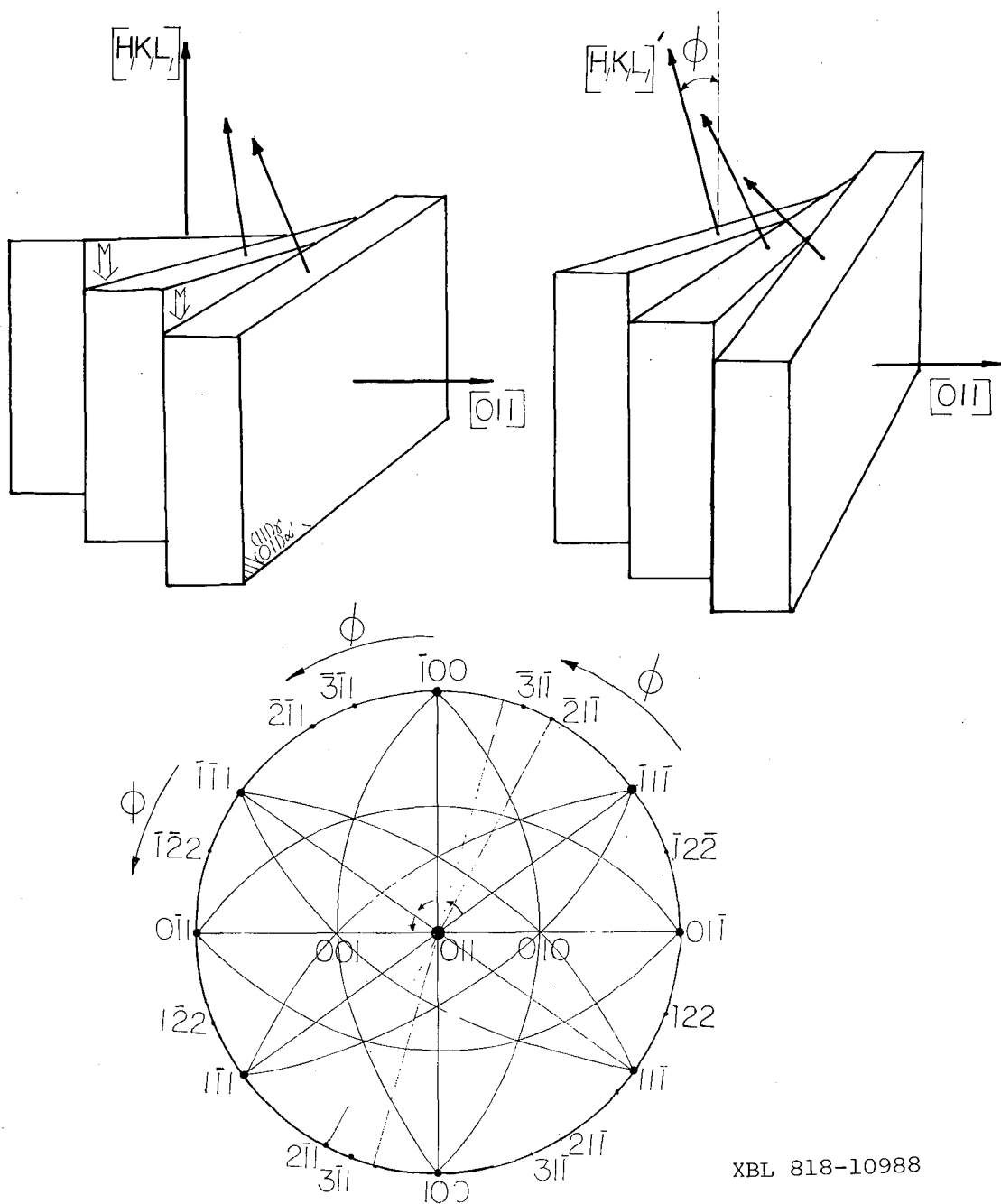


Fig. 10. The experiment to confirm the hypothesis that the successive laths are related geometrically by a rotation around the common  $[110]_M$  axis. Configuration of the laths (a) before tilting and (b) after tilting. (c) Stereographic projection showing the expected changes in the type of the diffraction patterns (along the poles 90 degrees to common  $[110]_M$ ) after tilting.

In the present alloys the above situation is frequently observed and new experiments were designed to check the hypothesis reviewed above. The experiment required orienting a packet of interest in such a manner all the laths line up "edge-on". Tilting is then done in one direction perpendicular to common  $\langle 110 \rangle_M$ . Assuming the first lath is in  $[\bar{1}1\bar{1}]$  z.a. orientation, and the second is in  $[\bar{1}\bar{1}1]$  z.a. orientation, and so on, tilting the foil, say counterclockwise, around  $[110]_M$  by  $\phi$  degrees brings lath (1), e.g., near  $[\bar{3}1\bar{1}]$ , and lath (2) near  $[0\bar{1}1]$ , and other laths assume new z.a. orientation accordingly (Fig. 10a-b). The experiments are tedious because during tilting through high angles and maintaining a small area in the microdiffraction condition is difficult. With magnetic alloys the problem is even worse because bending of the foil by the magnetic flux may reverse during tilting. Nonetheless, numerous experiments were carried out to obtain the required conditions, e.g., small foil dimensions (prepared by window technique) to decrease the amount of magnetic flux lines through the foil, lower carbon alloys where the lath boundaries tend to become straighter, the laths longer and the dislocation density lower.

The concept of such an experiment is shown in Fig. 11, where in (a) and (b), the microdiffraction patterns taken (with electron probe size of  $400 \text{ \AA}$ ) from individual regions marked (1) through (12) are given. One may note that patterns taken (1) through (4) show  $\langle 111 \rangle_M$  symmetry, and (5),

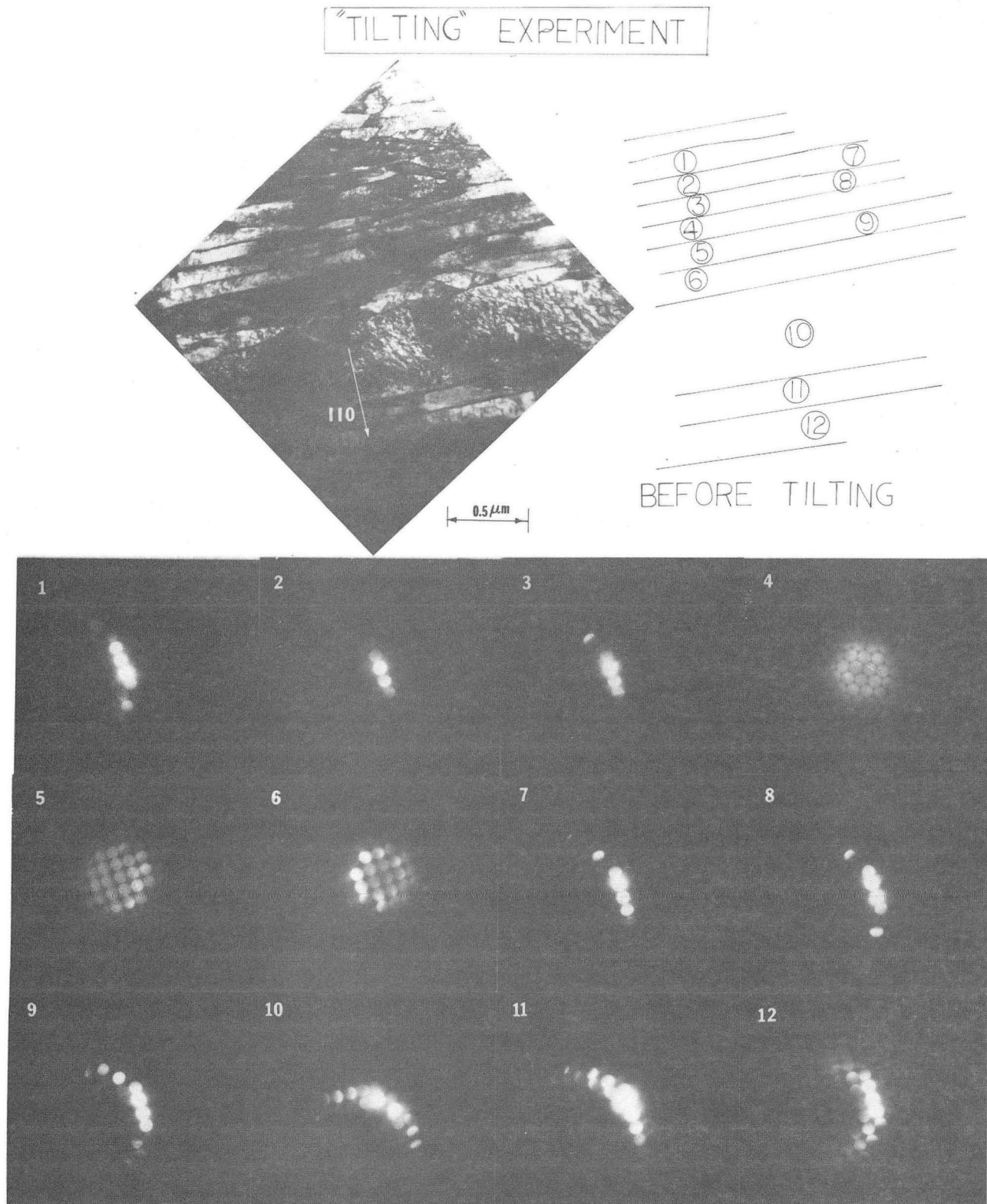


Fig. 11. (a) The analysis of the tilting experiment (0.1 carbon alloy). Microdiffraction patterns (1) to (12) were taken from the corresponding laths before tilting.

XBB 817-7033



(6), and (10), (11), (12) show  $\langle 100 \rangle_M$  symmetry with slight misalignments. After tilting the foil about  $30^\circ$  around the  $[110]_M$  common axis, microdiffraction patterns from the same individual laths as before again gave similar patterns for laths (1) through (4), i.e.,  $\langle 113 \rangle_M$  and for (5), (6), and (10) through (12), i.e., around  $\langle 112 \rangle_M$ , Fig. 11-b. The result is that the first stack of laths ((1) through (4)) cluster about the same  $\langle 111 \rangle_M$  pole, say  $[111]_M$  and not different  $\langle 111 \rangle_M$  poles, as has been proposed earlier. (40,92) Analysis of the second stack produced a similar result although unlike the  $\bar{1}11$  vs.  $1\bar{1}1$  case  $[100]$  cannot be distinguished from the  $[010]$  pole.

Thus it is clear that the laths in a stack tend to cluster around a particular pole with only slight misalignment in a direction perpendicular to a common  $[110]_M$ . The misorientations of the laths near  $[111]_M$  and  $[100]_M$  poles (and also near  $[113]_M$  and  $[112]_M$  after tilting) were measured to an accuracy of  $0.5^\circ$ . The results, plotted on a Kikuchi map along the  $(110)$  pair, indicate that the misorientation is about a direction in  $(110)_M$  plane and varies  $0$  to  $10^\circ$  in either sense around that direction (Fig. 11-c). The final situation is also shown on a  $[001]$  stereographic projection (Fig. 11-d) which shows the poles corresponding to the diffraction patterns observed before and after tilting around the  $(110)_M$  trace.

AFTER TILTING

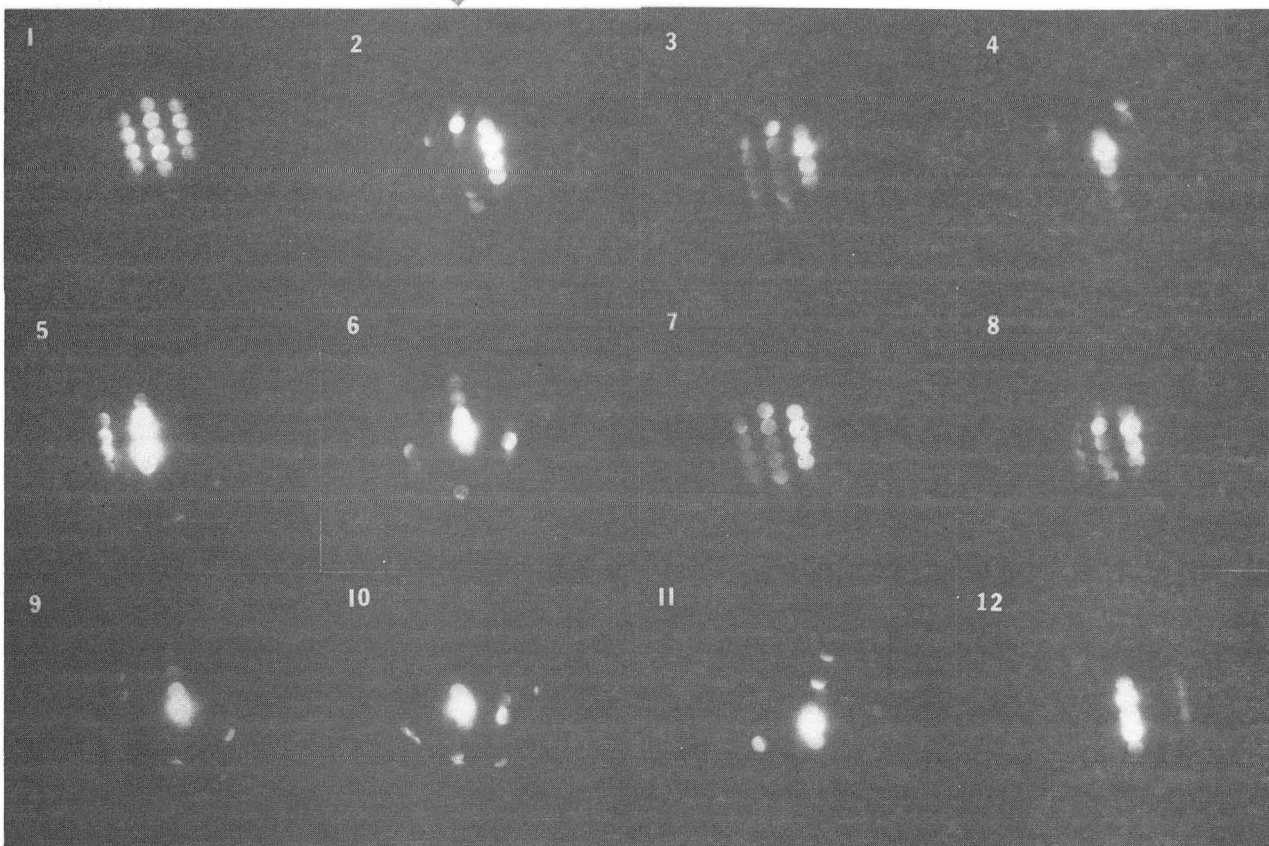
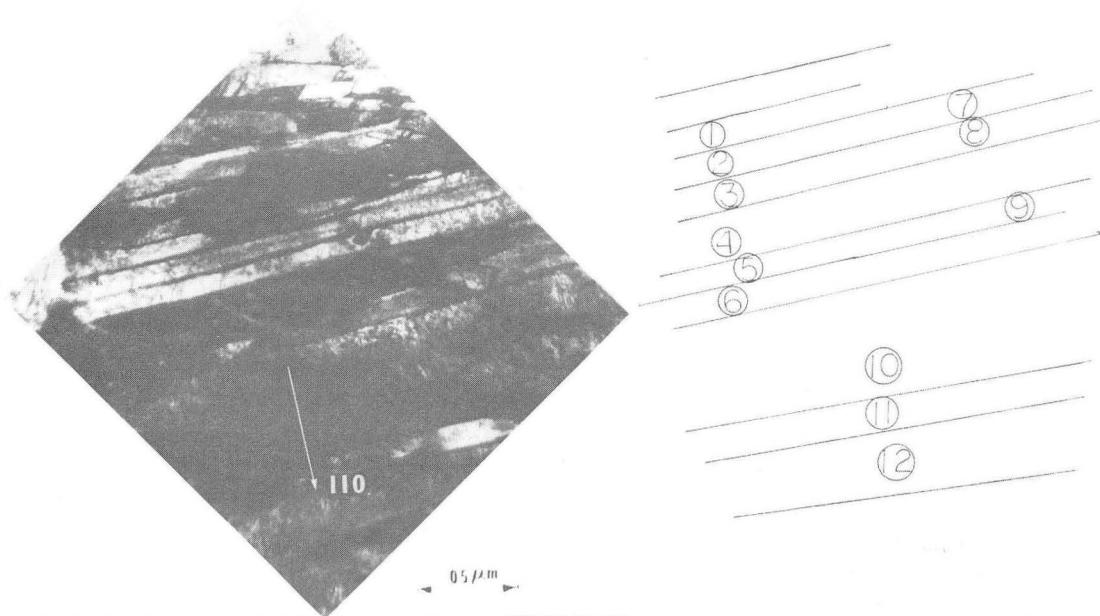
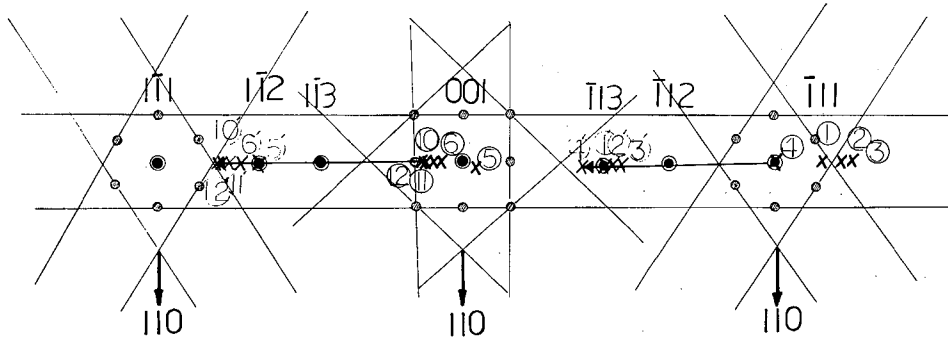


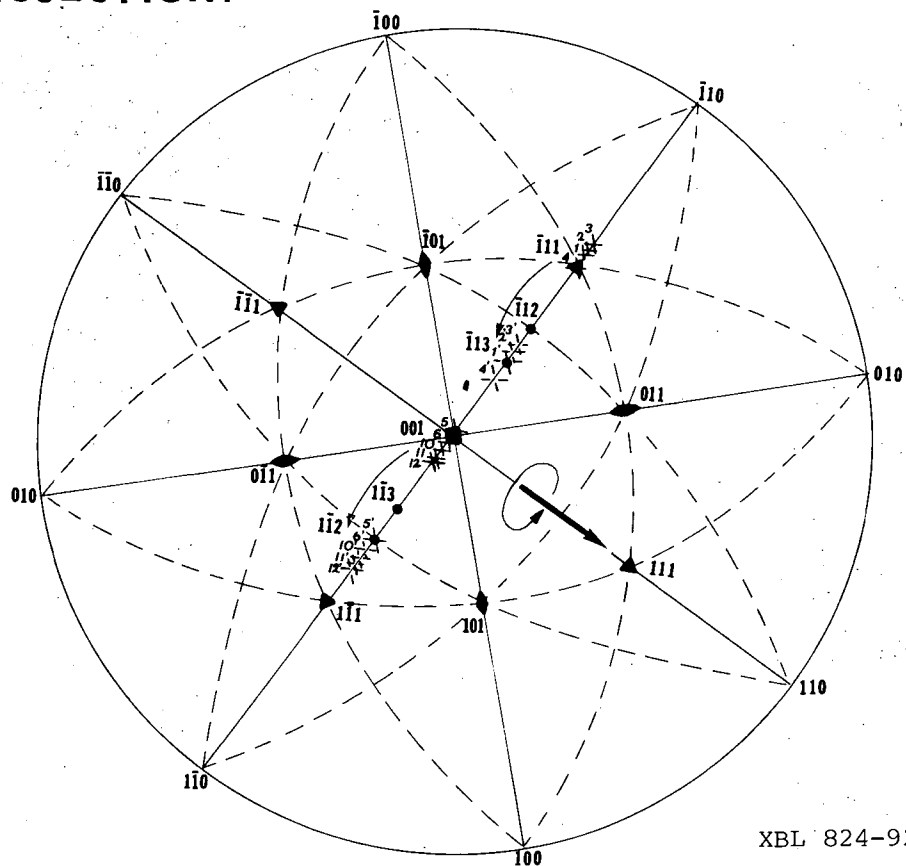
Fig. 11. (b) The microdiffraction patterns after tilting. Patterns (7), (8) and (9) were taken along the same laths [(2), (3), and (5)] to assure the slight misorientation along a particular lath which is not more than  $0.5^\circ$ .

XBB 817-7028

**ANALYSIS of the TILTING EXPERIMENT  
KIKUCHI MAP:**



**STEREOGRAPHIC  
PROJECTION:**



XBL 824-9224

Fig. 11. (c) The analysis of the orientations of the adjacent laths on a Kikuchi map. (d) The analysis on a  $[001]_M$  stereographic projection.

(iii) Abrupt changes in lath orientation, e.g., from  $\langle 111 \rangle_M$  to  $\langle 100 \rangle_M$  in a packet: It was noted earlier that the stacks of laths within a packet tend to cluster around  $\langle 111 \rangle_M$  or  $\langle 100 \rangle_M$ . The question still remains whether laths in a particular stack are in one  $\langle 111 \rangle_M$  orientation with other stacks in different  $\langle 111 \rangle_M$  orientations. Further tilting experiments on several groups of laths in a particular packet (in both 0.1 and 0.3 wt% carbon alloys) were carried out to reveal the exact change in the orientation between adjacent stacks.

A typical example of a packet with parallel lath boundaries which contain retained austenite is shown in Fig. 12-a. Microdiffraction patterns from individual laths (1) through (19) show that there is a cyclic pattern of abrupt changes in orientation from  $\langle 111 \rangle_M$  to  $\langle 100 \rangle_M$  and then back to  $\langle 111 \rangle_M$ . The microdiffraction patterns indicate that laths (1), (9), (11), (14), (15), and (18) are near a  $\langle 001 \rangle_M$  zone axis (z.a.) orientation, while the others singly and in groups are close to a  $\langle 111 \rangle_M$  z.a. (Fig. 12-a).

Assuming that the  $[110]_M$  direction over the whole number of laths is fixed, the question is whether the laths from different batches of  $\langle 111 \rangle_M$  have the same or different indices, i.e., whether different stacks belong to the same particular  $\langle 111 \rangle_M$  pole or not. To check this point, another tilting experiment was conducted on the same region of the foil. Keeping a particular  $[110]_M$  direction fixed in space

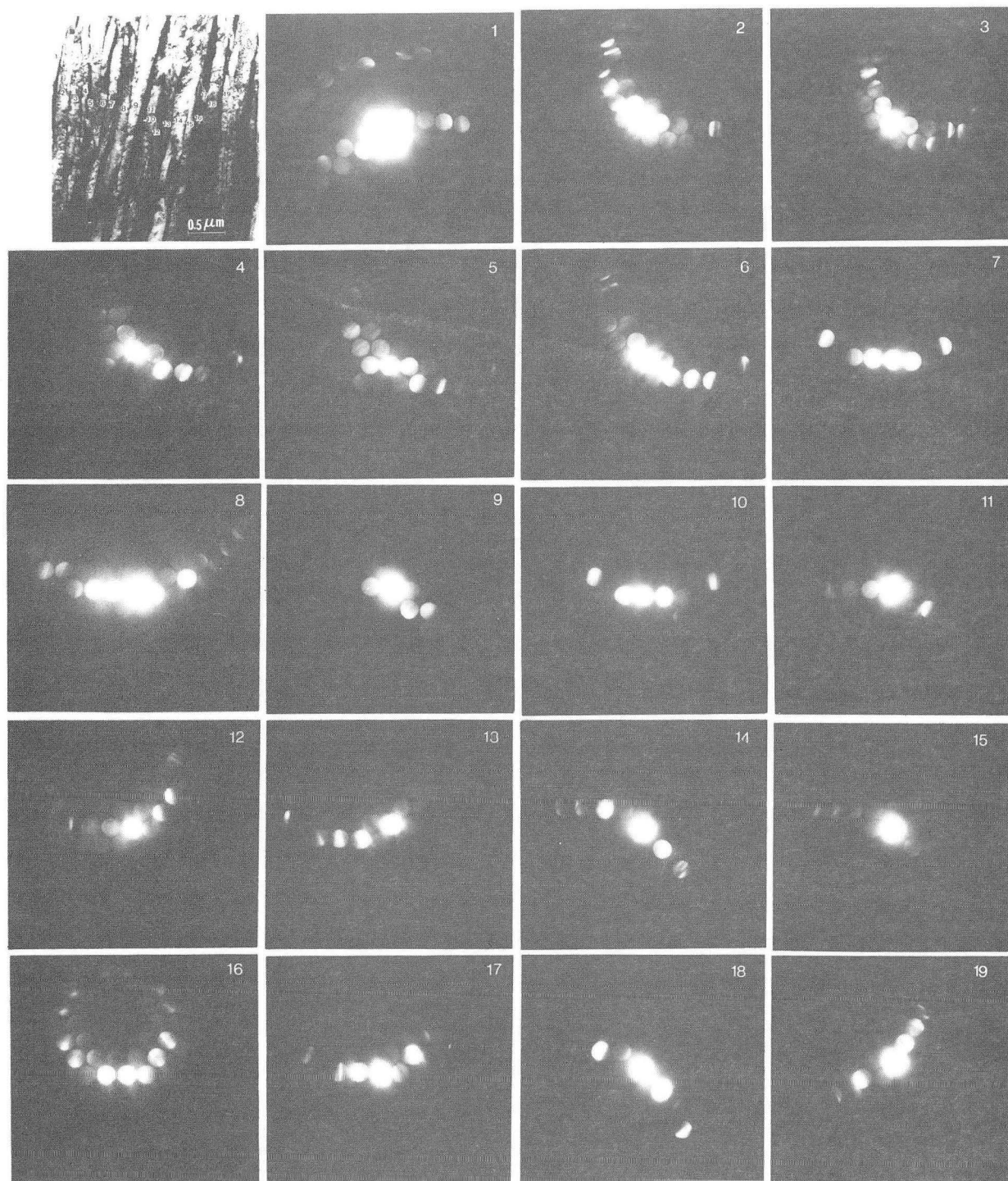
**BEFORE TILTING**

Fig. 12. The tilting experiment. (a) Microdiffraction patterns (1) through (19) were taken from the regions shown in the BF image before tilting (Alloy 3). XBB 824-3498

## AFTER TILTING

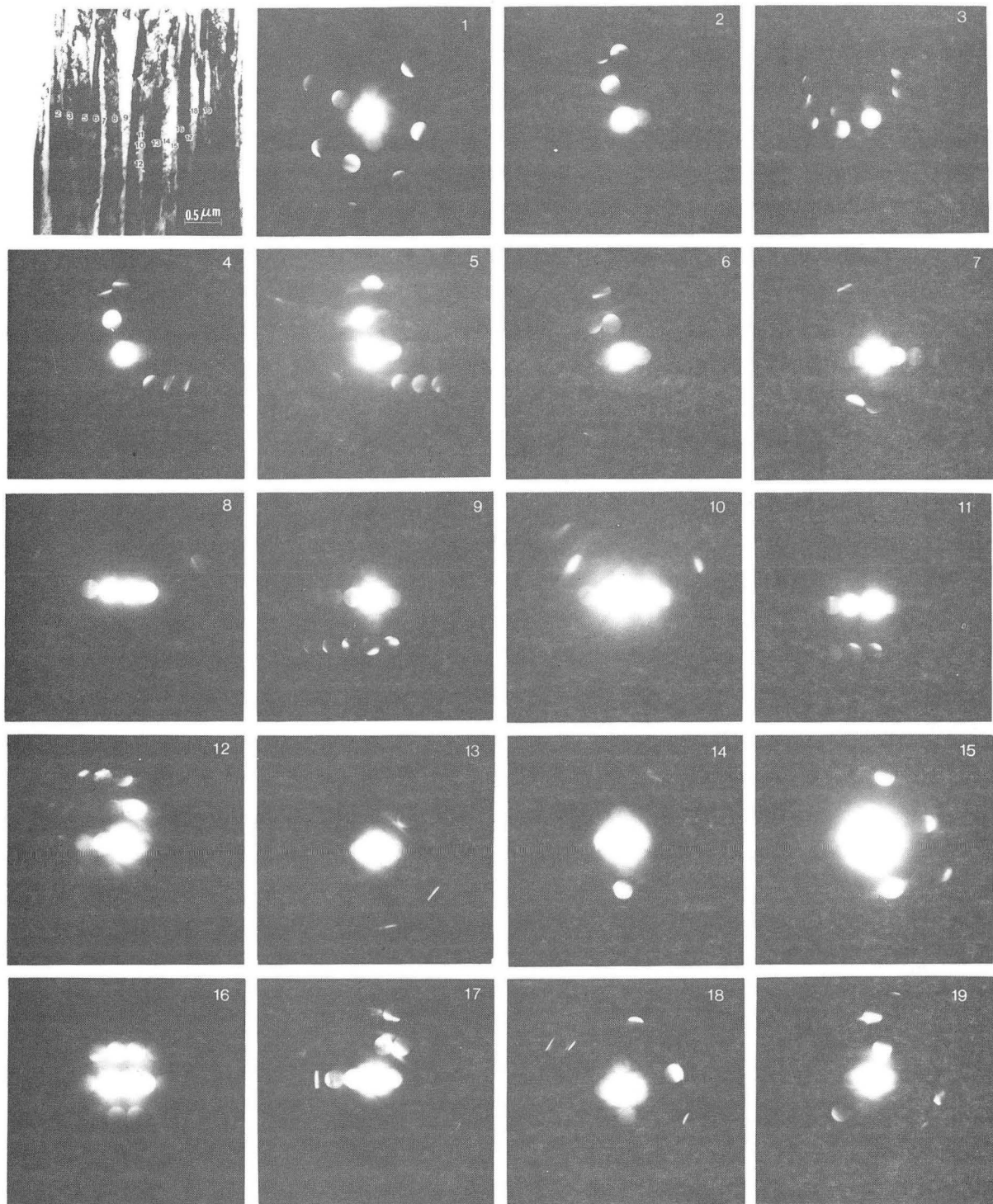


Fig. 12. (b) Microdiffraction patterns taken from the corresponding laths after tilting.

XBB 824-3497

the foil is tilted counterclockwise about  $35^\circ$ . The micro-diffraction patterns then taken from the corresponding areas from the laths (1) through (19) are shown in Fig. 12-b. It can be seen that the laths previously having  $\langle 111 \rangle_M$  orientation now are near  $\langle 113 \rangle$  zone axis orientation, and correspondingly laths in  $\langle 001 \rangle_M$  orientation before the tilting are now near a  $\langle 112 \rangle_M$  z.a.

The results of the analysis of the preceding orientation changes between laths are summarized in Fig. 12-c through f, where each figure represents a portion of the [001] cubic stereographic projection, superimposed to a "Wulf Net," near  $\bar{1}11$ , 001,  $\bar{1}13$ , and  $\bar{1}12$  poles, respectively. The Wulf Net is oriented with respect to the projection and the diffraction patterns (in Fig. 12-a and b) to permit analysis of misorientation with high accuracy (i.e., about half a degree of arc). The poles, therefore, in Fig. 12-c through f, respectively, aligned with respect to the patterns in (a) and (b) (also refer to (9) which shows the relative positions of the above poles with respect to [110] pole, that is the poles  $[\bar{1}11]$ , [001],  $[\bar{1}13]$ , and  $[\bar{1}12]$  lie on the trace of the (110) plane). The patterns obtained (Fig. 12-b) after tilting the foil reveal that all  $\langle 111 \rangle$  stacks correspond to the same pole, say  $[\bar{1}11]_M$  and there are only slight misorientation between adjacent laths within the stack while the stacks themselves are separated by the lath(s) with the  $[001]_M$  zone axis. Note (in Fig. 12-c and d) that the angle

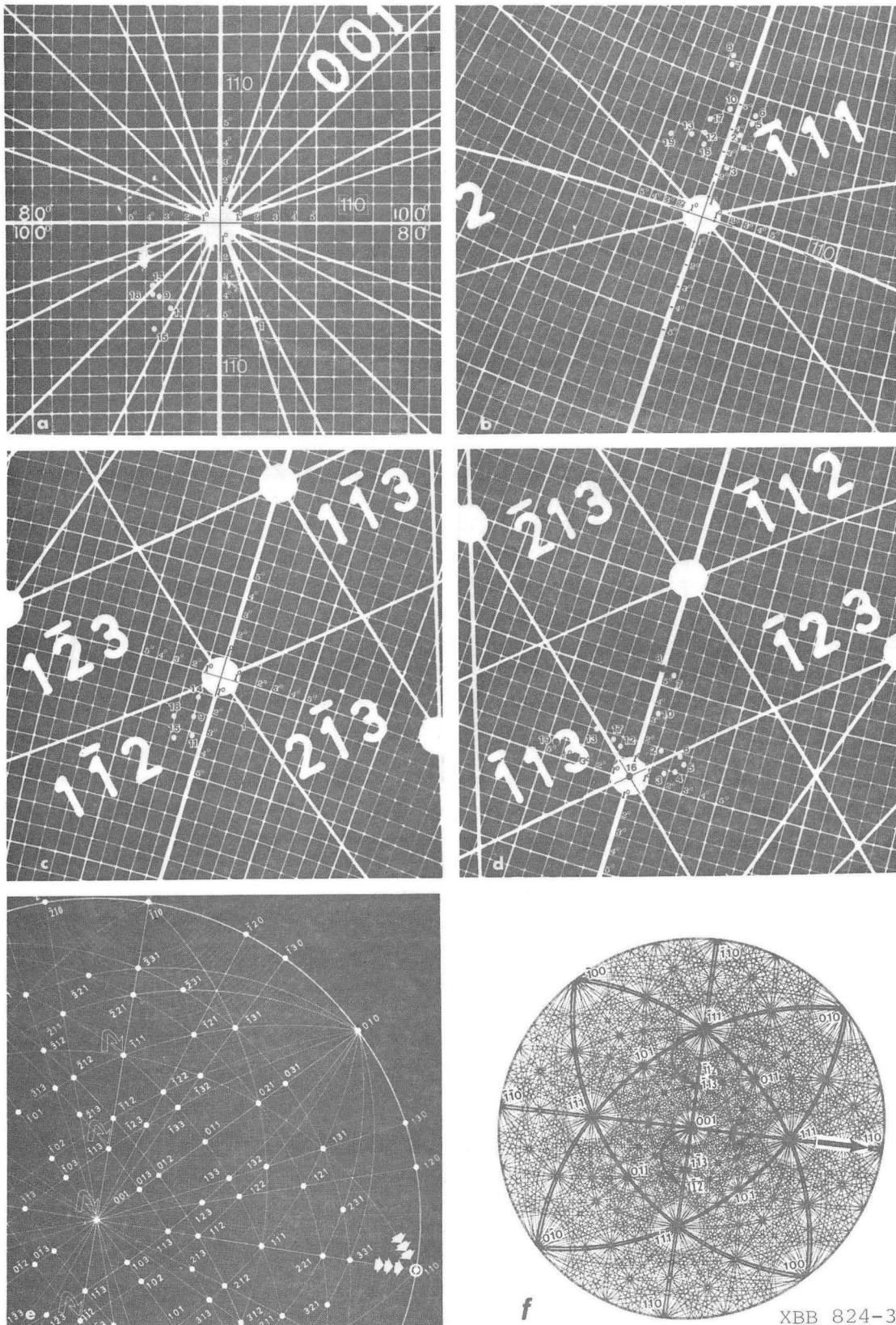


Fig. 12. (c) through (f) are portions of [001] stereographic projection corresponding to the poles  $[\bar{1}11]$ ,  $[011]$ ,  $[\bar{1}13]$  and  $[\bar{1}12]$ , respectively. (g) Relative positions of poles with respect to common  $[110]$  pole. (h) The summary of the analysis on a [001] stereographic Kikuchi map of Fe.

XBB 824-3496

M.S. Berkeley



between the laths belonging to a certain z.a. (either  $[\bar{1}11]$  or  $[001]$ ) change from fraction of a degree to 5 or more degrees (and these are, of course, repeated between the corresponding laths in Fig. 12-e and f). Also interesting to note is that the misorientations are clustered near the trace of  $(110)$  plane and that the misorientations fall on either side of the poles on that trace. The overall analysis is summarized in a  $[001]$  Stereographic Kikuchi map in Fig. 12-h which reveals the sense of tilting through the  $[110]$  Kikuchi band.

The abrupt change between the poles (i.e., from  $[\bar{1}11]_M$  to  $[001]_M$  on  $[113]_M$  to  $[\bar{1}12]_M$ ) may be explained on the basis of the orientation relationships between the retained austenite film and the adjacent martensite laths as discussed in Section 3.3.4. (note that in that section in Fig. 19-h the SAD pattern, taken from the area shown in Fig. 12-b, is a composite of two martensite patterns,  $[\bar{1}13]$  and  $[\bar{1}12]$ , and a superimposed austenite  $[112]$  pattern). The small change in alignment around the  $[110]_M$  direction will help to minimize the strain created during the  $\gamma$  to  $\alpha'$  transformation.

(iv) Observation of the laths belonging to different z.a. within the same packet: It is commonly observed that parallel laths in 0.3 wt% carbon alloys have more than one pole system and that laths belonging to several different poles are arranged side by side with the common  $\langle 110 \rangle_{\alpha'}$  axis perpendicular to their broad faces. Such a situation is

shown in the SAD pattern in Fig. 13 which is taken from a region within a single packet which contains parallel laths (see the inset). Here several patterns corresponding to martensite and one corresponding to austenite are superimposed. From the indexed schematic diffraction pattern in 13(b), it was found that the martensite patterns belong to  $[\bar{1}2\bar{1}]$ ,  $[\bar{3}\bar{1}1]$ ,  $[0\bar{1}1]$ , and  $[1\bar{1}1]$  z.a. and the austenite pattern belongs to  $[\bar{1}2\bar{1}]$  z.a. Note that within the accuracy of SAD, the patterns are not in a z.a. orientation and are tilted roughly in the direction perpendicular to  $[110]$  direction, i.e., within  $(110)_\alpha$  plane; tilted in both senses from the electron beam direction. The important fact here is that so many variants of laths are present within the same packet all having their  $[110]_\alpha$  direction in common. This point was also checked by DF imaging. When the reflections belonging to different individual z.a. were used for DF analysis, the laths belonging to those corresponding variants change contrast. However, when the common  $g_{110}$  reflection was used, all the variants changed contrast simultaneously including the retained austenite whose  $(111)_\gamma$  reflection is superimposed with  $(110)_\alpha$ . The retained austenite was also revealed by DF imaging using an isolated reflection such as  $g_{200}_\gamma$ . Within the accuracy of SAD patterns, the orientation relations between austenite and martensite planes and poles may be stated as follows;

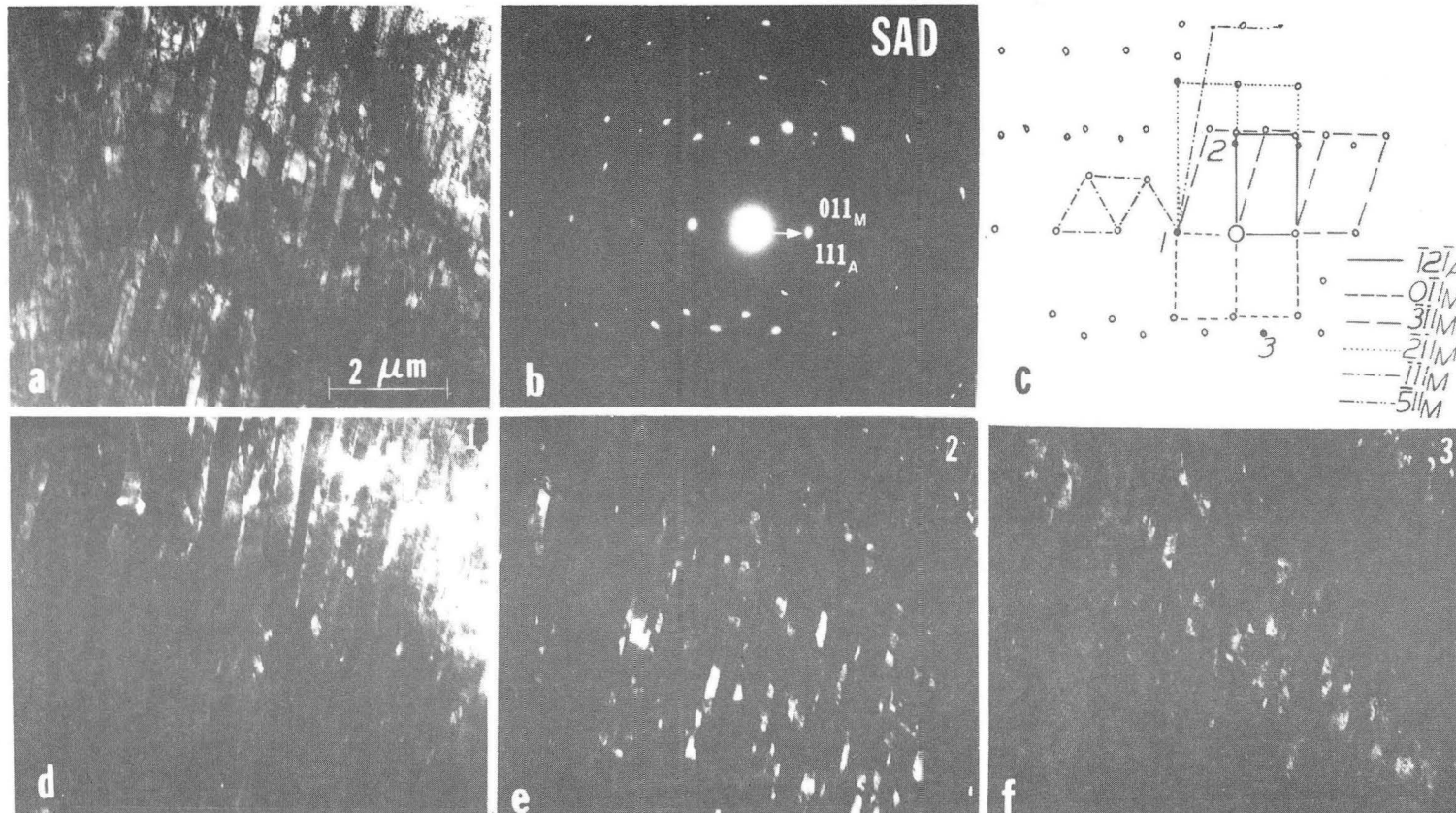


Fig. 13. Bright field (a) and selected area diffraction pattern (b) taken covering many laths in (a). The orientations are sketched in c. Dark field images are shown in d, e, and f from reflections 1, 2, and 3, respectively.

XBB 824-4819

$$\begin{aligned} & (110)_{\alpha}, // (111)_{\gamma} \\ \text{and} \quad & [0\bar{1}1]_{\alpha}, // [121]_{\gamma} \quad (1) \\ & [\bar{3}\bar{1}1]_{\alpha}, // [121]_{\gamma} \quad (2) \\ & [\bar{1}2\bar{1}]_{\alpha}, // [121]_{\gamma} \quad (3) \\ & [1\bar{1}1]_{\alpha}, // [121]_{\gamma} \quad (4) \end{aligned}$$

Further discussion on this subject appears in the section on the orientation relationship analysis (Section 3.3.3) and in the Discussion (Section 3.4).

(v) Occurrence of a "packet" between parallel laths:

It is frequently observed that in higher carbon alloys some packets of parallel laths contain an occasional lath that is slightly misoriented with respect to those on both sides, i.e., the situation of "lath" (2) in Figure 14. The microdiffraction patterns taken (using a small selected area aperture) near the boundaries of laths (1) and (3) are isolated single diffraction patterns (here  $\langle 111 \rangle$ ). However, the diffraction pattern taken from the "lath" (2) shows two superimposed  $\langle 111 \rangle_b$  patterns slightly rotated with respect to each other about the electron beam direction, i.e., near  $\langle 111 \rangle_b$ . The analysis shows that this is not because the laths (1) and (2) or (2) and (3) have low angle boundaries between them, but it is due to the fact that the "lath" (2) is indeed composed of much smaller martensite crystals (or laths) which are viewed "end-on" in the image (Fig. 1-b as opposed to "edge-on" configurations of the laths 1, 3, 4,

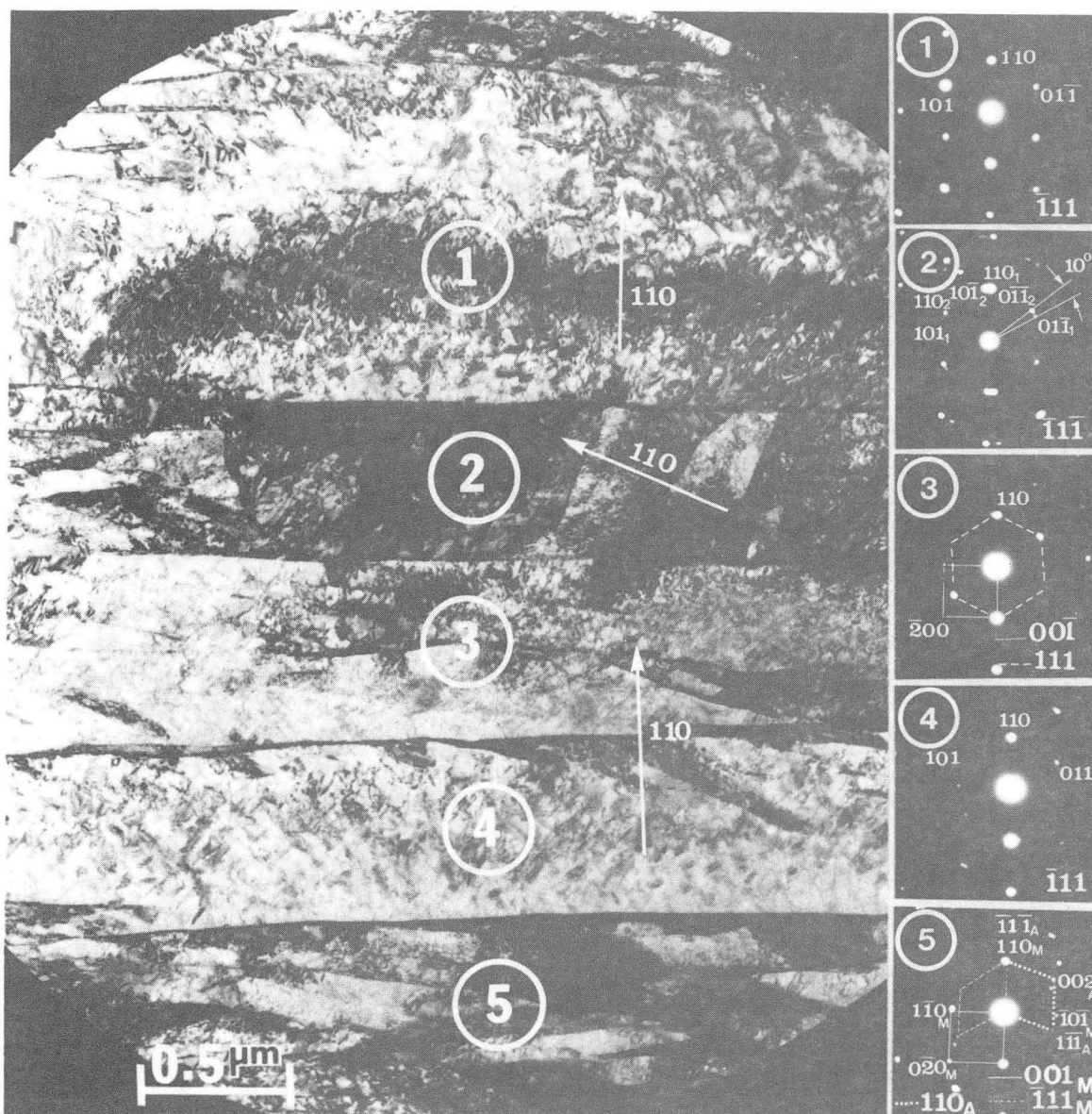


Fig. 14. A TEM micrograph from a region showing several laths with parallel boundaries. Note that the SAD pattern taken from lath (2) consists of two superimposed patterns belonging to, say,  $[111]_M$  and  $[\bar{1}\bar{1}\bar{1}]_M$  variants. (Note also in pattern (5) retained austenite reflections are also revealed) (Alloy 5). XBB 796-8216

etc.). This situation is similar to the one mentioned in Section 3.3.1. (Also see Figs. 7 and 8). Here the crystals in region (2) assume different austenite variant (i.e., one of  $\{111\}_A$  planes which is parallel to  $\{110\}_M$ ) than the laths (1) and (3) (which both have another austenite  $\{111\}_A$  variant). Therefore, region (2) should be a new packet formed between the laths (1) and (3). In  $\langle 111 \rangle$  electron beam direction two superimposed  $(111)_b$  patterns are observed diffracted from the crystals in region (2) and from the lath (1) (or (3)), which are rotated  $70^\circ$  with respect to each other around  $\langle 111 \rangle_M$  (or  $\langle 110 \rangle_A$ ), i.e., a rotation by an angle between the  $\{111\}$  planes of austenite (here  $(\bar{1}\bar{1}\bar{1})_A$  and  $(\bar{1}\bar{1}1)_A$  as in SAD pattern 5). This may also be interpreted as a  $10^\circ$  separation between the  $(110)_M$  reflections belonging to different  $\langle 111 \rangle$  zones of martensite (here  $[\bar{1}11]_M$  and  $[\bar{1}\bar{1}\bar{1}]_M$ ; see Fig. 7 for a schematic illustration). There is always retained austenite between the laths which was revealed by DF imaging. However, one may note that retained austenite reflections are very weak and difficult to see except in SAD patterns (5).

### 3.3.3. Determination of Orientation Relationships between Martensite and Austenite:

One important aspect of the crystallography of martensitic transformations is the lattice orientation relationships (OR) between the parent and the product phases which identify the correspondence between the planes and the directions in

the two phases. (64-67) In most studies the investigators found a single O.R. specific to a particular alloy type. For example, in Fe-Ni alloy the Bain O.R. (49,51) was identified. Similarly in Fe-Ni-C martensites Greninger and Troiano (G-T) O.R. was found. (67) In many other low alloy and medium carbon steels either Kurdjumov-Sachs (K-S) (15,39,40,64,83,84,93) or Nishiyama-Wassermann (N-W) (15,40,65,66,83,84) O.R.s have been reported. These authors reached their conclusions through analysis of indirect measurements, such as relating known traces in martensite to the crystallographic features of austenite. (15,33,36,39,83-87) However, a recent observation (93) made in a class of medium carbon steels, similar to the ones used in this study, crystallographic analyses were performed in which it was shown that both K-S and N-W O.R.s are present within the same region of the specimen. (40,92,93)

Actually a small amount of austenite does remain untransformed as thin films between the martensite laths which was long overlooked in low carbon martensitic Fe-C alloys. (15,33,39,53,56,80-87) The total amount of retained austenite is relatively low (2-5 vol%) (45,121) and detailed X-ray analysis (4,9) is not possible. However, determination of the orientation relationships between austenite and martensite is possible by means of precise electron diffraction analysis in the TEM.

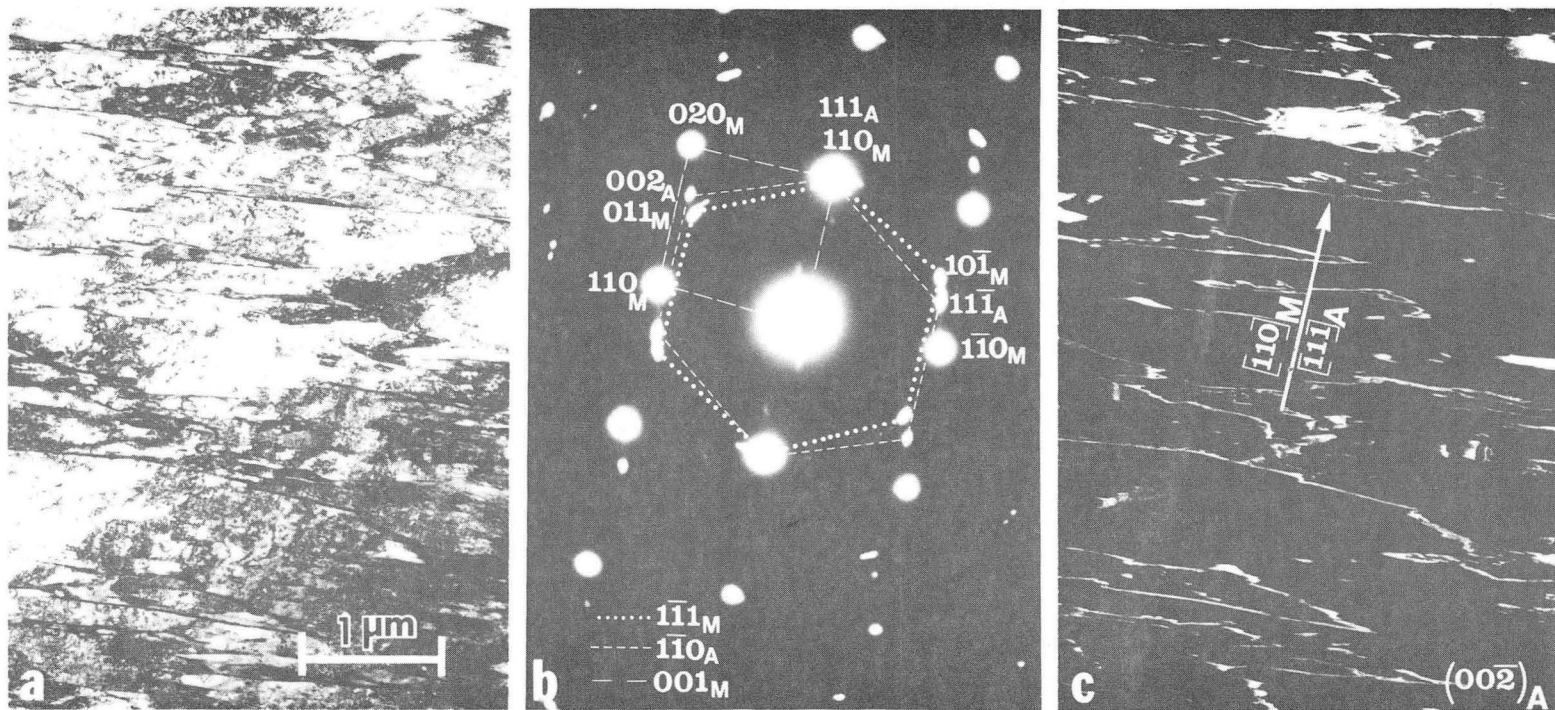


Fig. 15. (a) BF, (b) typical SAD pattern and (c) DF using  $g_{002\bar{A}}$  reflection revealing the general appearance of the films (2 Ni Alloy).

XBB 796-7880



A typical microstructure specific to the present alloy systems is shown in Fig. 15 where in the D.F. (b), taken by using an austenite reflection (here  $\bar{g}_{200A}$ )<sup>(88,89)</sup> retained austenite changes contrast at the martensite lath boundaries as continuous films. A selected area diffraction pattern taken from an area covering several laths and the retained austenite films, is shown in (c). In this pattern there are basically three superimposed patterns present, namely  $\langle 111 \rangle_{\alpha_1}$ ,  $\langle 100 \rangle_{\alpha_2}$  and  $\langle 110 \rangle_{\gamma}$ . From the symmetry of the patterns the correspondence of the directions and the planes may be stated as follows (see Fig. 16):

$$\begin{aligned} [110]_{\gamma} // [100]_{\alpha_2} \\ (111)_{\gamma} // (011)_{\alpha_2} \end{aligned} \quad (1)$$

and

$$\begin{aligned} [\bar{1}10]_{\gamma} // [\bar{1}1\bar{1}]_{\alpha_1} \\ (111)_{\gamma} // (011)_{\alpha_1} \end{aligned} \quad (2)$$

It follows that, the first of these identities corresponds to N-W O.R., and the second to K-S O.R., as interpreted earlier.<sup>(40,45,89,92,93)</sup>

In order to see the interrelationships between the O.R.s, it is informative to quote the most commonly observed O.R.s between  $\alpha'$  and  $\gamma$  in steels. These are as follows:<sup>(64-66)</sup>

$$\begin{aligned} (110)_{\alpha'} // (111)_{\gamma} \\ [\bar{1}\bar{1}1]_{\alpha'} // [1\bar{1}0]_{\gamma} \\ \text{and } [\bar{1}12]_{\alpha'} // [\bar{1}\bar{1}2]_{\gamma} \end{aligned} \quad \text{K-S}$$

# INTERPRETATION OF $\langle 111 \rangle_{\alpha_1} // \langle 100 \rangle_{\alpha_2} // \langle 110 \rangle_{\gamma}$ TRIPLET

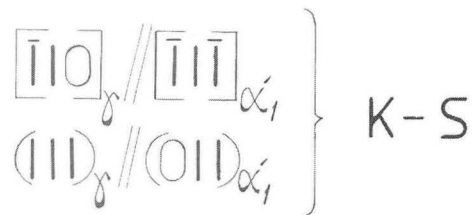
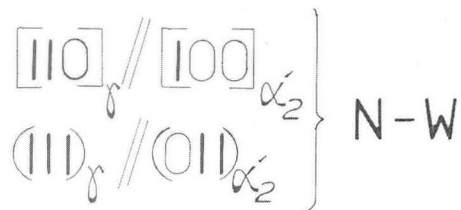
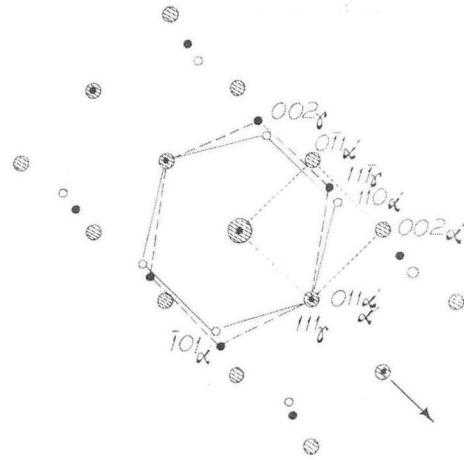
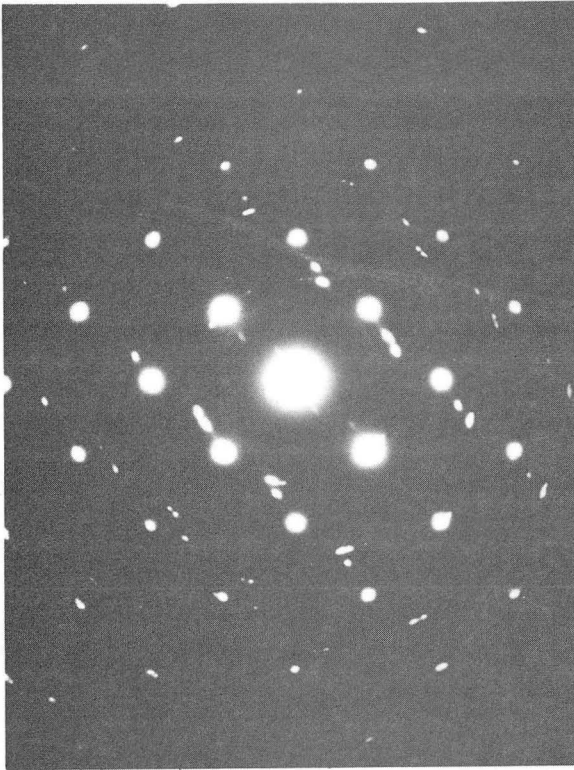


Fig. 16. Indexing and the interpretation of the frequently occurring  $\langle 111 \rangle_{M_1} / \langle 100 \rangle_{M_2} / \langle 110 \rangle_A$  triple SAD pattern. The patterns belonging to those z.a. appear to be fairly symmetrical.

XBB 818-7241

$$\begin{array}{l}
 (110)_{\alpha} // (111)_{\gamma} \\
 [001]_{\alpha} // [0\bar{1}1]_{\gamma} \quad \text{N-W} \\
 \text{and} \quad [\bar{1}12]_{\alpha}, 5.26^{\circ} \text{ from } [\bar{1}\bar{1}2]_{\gamma}
 \end{array}$$

The correspondence between the planes and the axes in both phases are also shown in detail on  $[001]_A$  stereographic projects in Fig. 17(a) and (b). One may see from this figure that the interrelationships between K-S and N-W is that when the crystal, having K-S O.R., is rotated about a common  $[011]_{\alpha}$ , about  $5.26^{\circ}$ , one achieves the N-W O.R. Fig. 18 also reveals this interrelationship between the two O.R.s schematically where the plane of the paper in the case of austenite is  $\{111\}$  and in martensite  $\{110\}$ . The  $[01\bar{1}]_{\alpha}$  axis derived from  $[\bar{2}11]_{\gamma}$  in N-W relation while there is a  $5.26^{\circ}$  angle between these directions in the K-S relation.

There is also a third kind commonly observed O.R., namely G-T, <sup>(67)</sup> in which the relations between the planes and the axes are almost those of between the N-W and K-S variants. <sup>(67,102)</sup> By making use of Fig. 17 these relations may be summarized as follows:

$$\begin{array}{l}
 (110)_{\alpha}, \text{ within about } 1^{\circ} \text{ from } (111)_{\gamma} \\
 [1\bar{1}1]_{\alpha}, 2.5^{\circ} \text{ from } [1\bar{1}0]_{\gamma} \\
 \text{and} \quad [\bar{1}12]_{\alpha}, 2.5^{\circ} \text{ from } [0\bar{1}1]_{\gamma}
 \end{array}$$

The interpretation of the triple  $\langle 111 \rangle_{M_1} / \langle 110 \rangle_A / \langle 100 \rangle_{M_2}$  diffraction patterns such as the ones shown in Figs. 15 and 16, was based on the accuracy of the SAD patterns, the

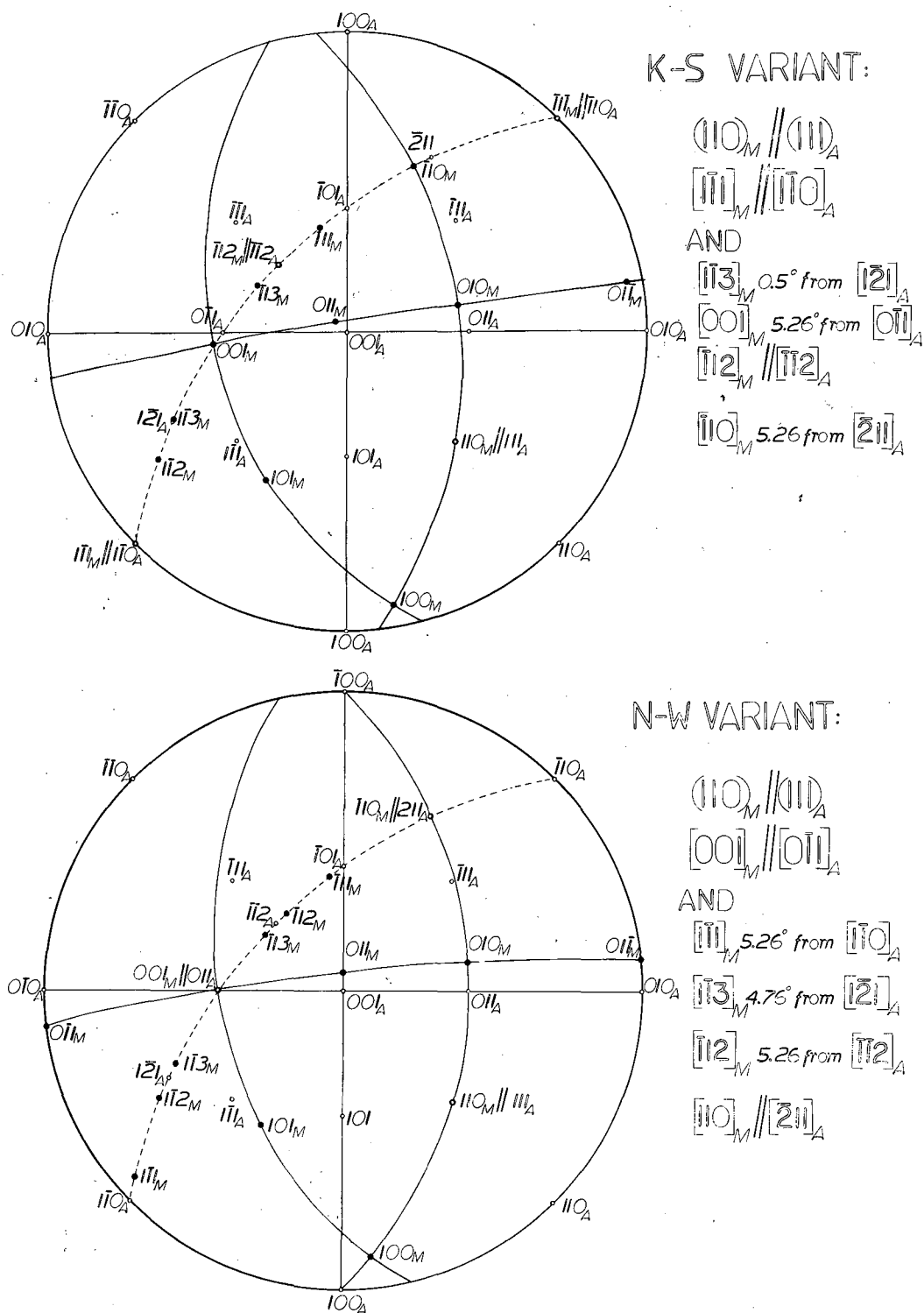


Fig. 17. Stereographic projection analysis of the most commonly occurring orientation relationships, namely K-S (a) and N-W (b). (Indices of the parallel planes and the relations between the directions are indicated on the right.)

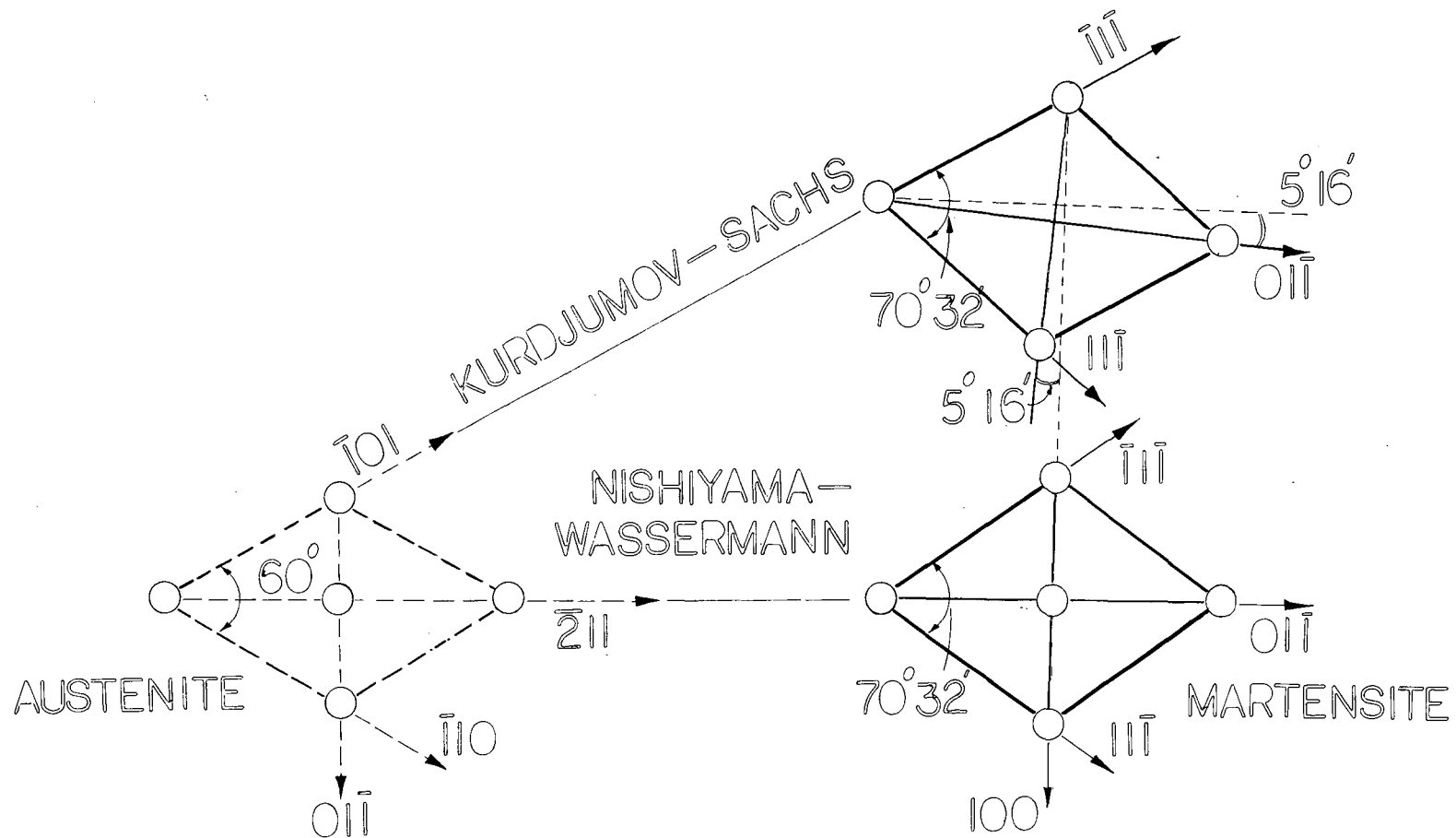


Fig. 18. The relationship between the K-S and N-W O.R.'s. Plane of the paper for austenite is  $(111)$ , and for martensite is  $(110)$ . Notice the  $5.26^\circ$  rotation between the two O.R.'s.

XBL 818-11156

symmetry of the patterns belonging to different z.a., and the deviation of these z.a. with respect to each other. (40,89)

Because of the spherical aberration, the inaccuracy in a SAD pattern can be  $5^\circ$  (94,95) and even with the Ryder and Pitsch procedure (95) the accuracy is still not better than  $2^\circ$

(extremely difficult in the present case because the analyses requires two sets of reflections belonging to two nearly parallel zones and the intensity of the reflections; with composite patterns, as in our case, some reflections are superimposed which increases the intensity of those spots).

In addition, the high dislocation density both in  $\gamma$  and  $\alpha'$  so diffuses the Kikuchi patterns that they cannot be used to determine orientations to within  $1^\circ$ . (96) This accuracy is needed because only a  $2.5^\circ$  angle distinguishes the K-S, N-W, or G-T O.R. variants.

Therefore, in order to unambiguously determine the exact O.R., one has to obtain single isolated patterns from retained austenite and the martensite crystals in either or both sides of the boundary. (99,100) This is obviously not a straightforward experiment to perform, given the fact that, in addition to the high defect density, the austenite film is very thin, the microdiffraction method (92) which utilizes a small ( $\sim 400 \text{ \AA}$  dia.) and highly convergent electron beam to obtain diffraction patterns from an area roughly equal to the probe size.

A number of experiments have been conducted by micro-diffraction method. An example is shown in Fig. 19 which involves a region giving the frequently observed triple  $\langle 111 \rangle_{\alpha_1} / \langle 110 \rangle_{\gamma} / \langle 100 \rangle_{\alpha_2}$  diffraction pattern. By using a small probe (convergence angles 5 mrad. in the TEM mode) the microdiffraction patterns were taken, from the regions in (a), as shown in (b), (c) and (d), which are identified as  $[\bar{1}11]_{\alpha_1}$ ,  $[110]_{\gamma}$  and  $[100]_{\alpha_2}$ , respectively. The foil was then tilted about the common  $\langle 110 \rangle_{\alpha} // \langle 111 \rangle_{\gamma}$  axes by approximately  $30^\circ$  and the microdiffraction patterns were again taken from the corresponding regions. Tilting was done to ensure the reproducibility of the analyses. The result of the experiment is shown plotted in a  $[001]_{\gamma}$  stereographic projection in Fig. 20(a). From this analysis, one obtains the following relations:

$$\begin{aligned}
 & (110)_{\alpha} // (111)_{\gamma} , \\
 & [\bar{1}\bar{1}1]_{\alpha} , 2.50^\circ \text{ off } [0\bar{1}1]_{\gamma} , \\
 \text{and} & [001]_{\alpha} , 2.85^\circ \text{ off } [0\bar{1}1]_{\gamma} , \text{ (in opposite sense)} \\
 \\ 
 \text{or} & (110)_{\alpha} // (111)_{\gamma} , \\
 & [\bar{1}\bar{1}3]_{\alpha} , 2.00^\circ \text{ off } [\bar{1}\bar{1}2]_{\gamma} , \\
 \text{and} & [\bar{1}12]_{\alpha} , 3.50^\circ \text{ off } [\bar{1}\bar{1}2]_{\gamma} , \text{ (in opposite sense)}
 \end{aligned}$$

It can be seen from the foregoing discussion that these relations are close to either K-S or N-W O.R.s. However, within the reproducibility of the tilting experiments, the

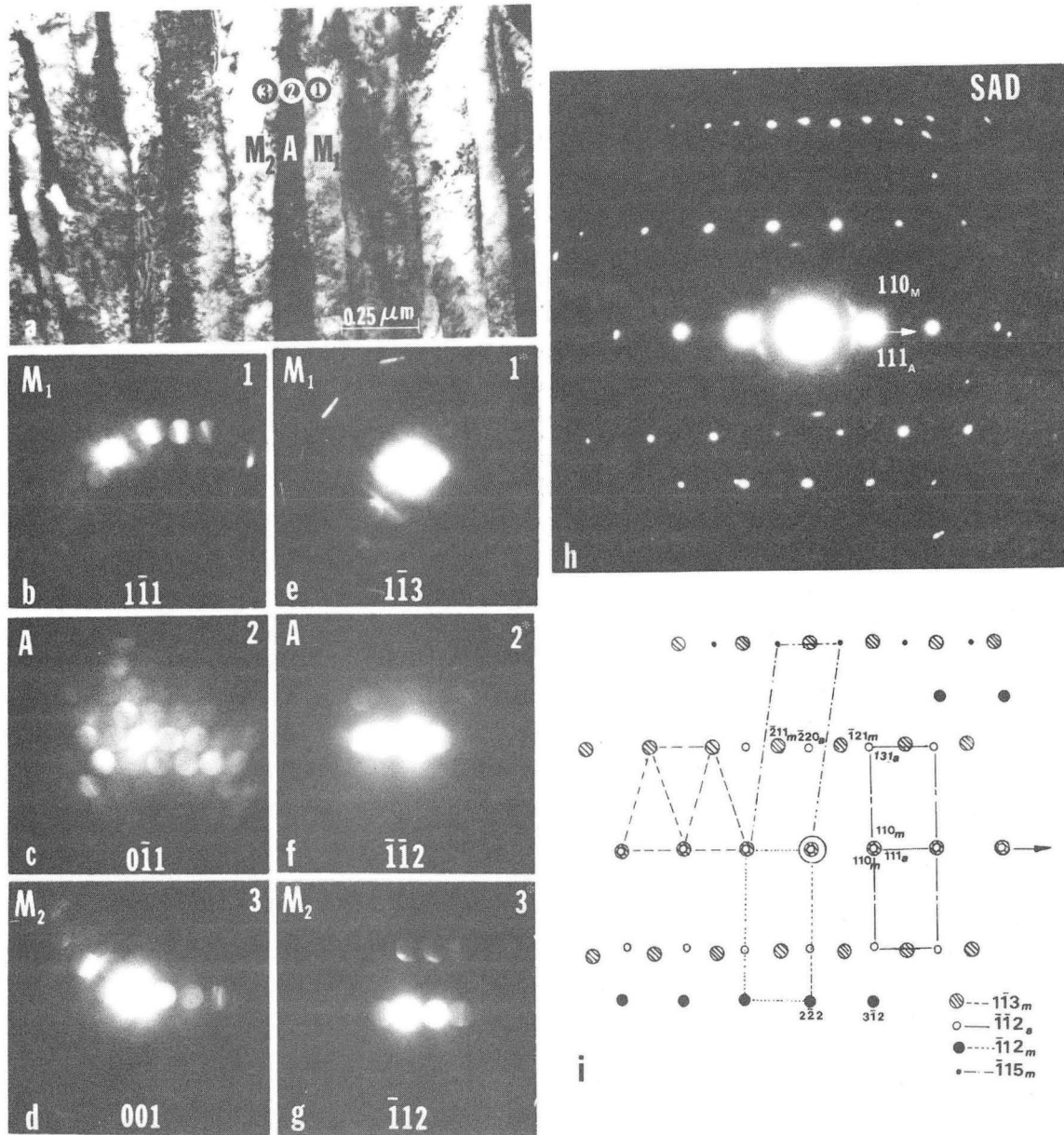


Fig. 19. Microdiffraction experiment to determine the correct O.R. between the martensite laths (1 and 3) and austenite (2) in a 0.1 carbon alloy. Micrograph (a) shows the arrangement of austenite and martensite on both sides. Microdiffraction patterns (b), (c) and (d) were taken before and (e), (f) and (g) were taken after the controlled tilting. (h) is the SAD pattern taken from the region and (i) is the indexed schematic pattern corresponding to (h). XBB 824-3500



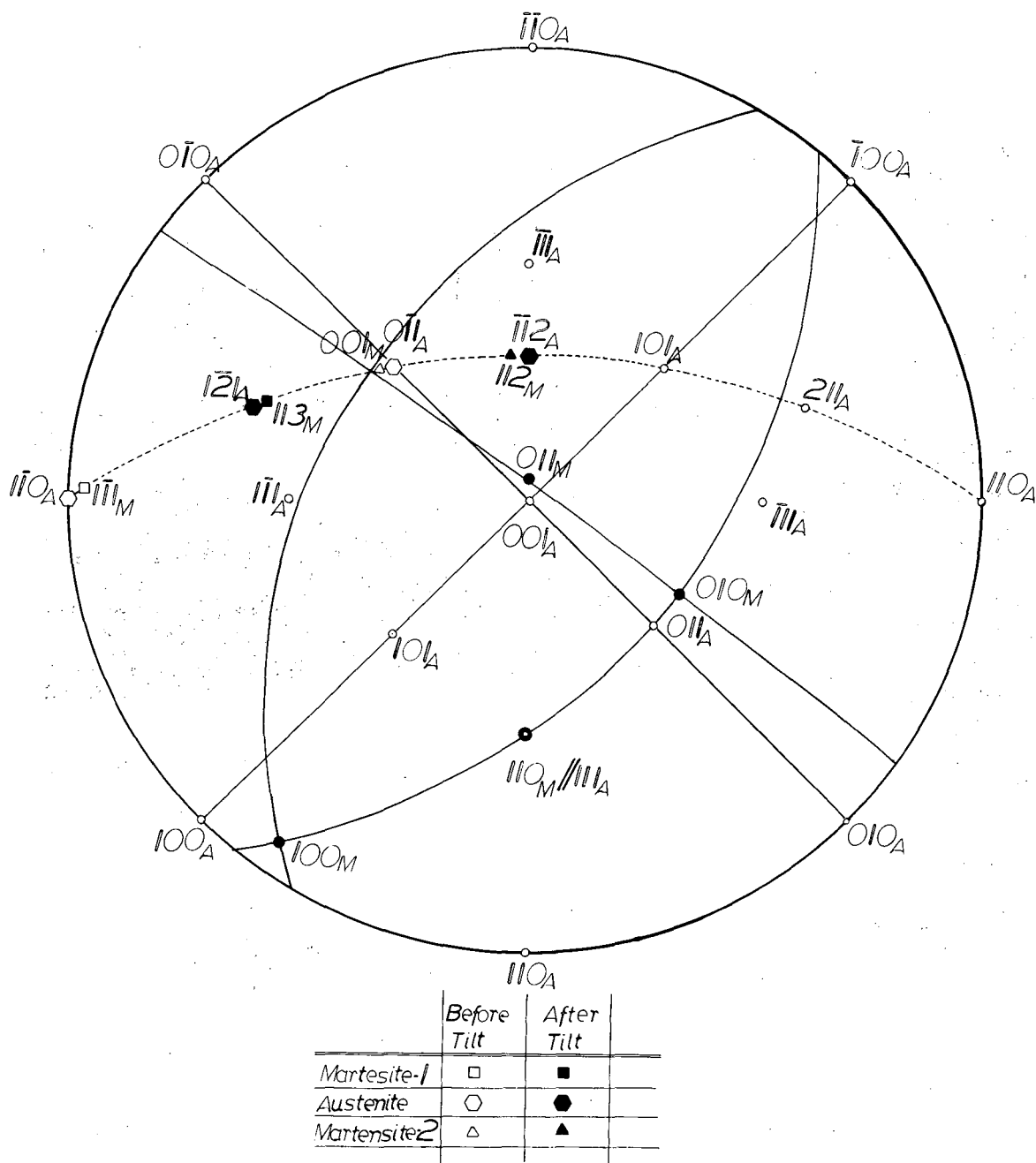


Fig. 20. Stereographic analysis of the orientation relationships in Fig. 19. Note the scatter of the poles of the microdiffraction patterns with respect to the electron beam direction on a great circle corresponding to common  $[110]_M // [111]_A$  zone. (Relative misorientations of  $M_1$  and  $M_2$  are corrected according to that of A.)

XBL 825-9886

relations are much closer to the G-T O.R. Hence it may be concluded that both martensite laths are in the G-T O.R. with the retained austenite.

The results of many experiments involving retained austenite and laths on either or both sides of the film (sometimes including tilting to another z.a. orientation) showed that there is indeed a scatter of poles between K-S and N-W. Therefore, orientation relationships can be anywhere between K-S and N-W, but mostly occur around G-T O.R.

3.3.4. Habit Plane Analysis. Habit plane analysis of packets of laths with fairly straight boundaries was carried out on several different alloys. The trace analyses were done on stereographic projections both before and after tilting about  $[110]_{\alpha}$ , direction common to all laths in a packet. The analysis given in Fig. 21-a shows the trace normals for the boundaries when the laths are in different z.a. orientation. Each pair of the lines indicates the two extreme deviations from the normal trace. The boundary normal traces fall into a specific zone which defines the indices of the pole of the normal to the habit plane. The presence of retained austenite in the sample enables direct determination of the habit plane knowing the fact that the  $(110)_{\alpha}$  is parallel to  $(111)_{\gamma}$  as ensured by microdiffraction information taken from austenite during the tilting



experiments. In a sense, therefore, the habit plane analysis is done directly on austenite. As shown in Fig. 21-a, which is a composite stereographic projection belonging to  $\alpha'$  and retained austenite (in K-S O.R.), the habit plane is very close (within  $5^\circ$ ) to  $(111)_\gamma$ .

From the observations of many lath configurations in the TEM an approximate shape of the individual martensite units has been determined. These units are usually seen in the "edge-on" configuration (Figs. 6 and 15), occasionally "end-on" (Figs. 7 and 14) and almost never "face on" but sometimes appears oblique to the broad faces. Thus the units are "laths" (elongated parallelepipeds) with curved ends (see, e.g., Fig. 3) and retained austenite films of varying thickness covering the surfaces. As shown in Fig. 21-b, the broad faces of the laths are parallel to  $(110)_\alpha$ , (which are parallel to  $(111)_\gamma$ ), the long direction of the laths are in  $\langle \bar{1}11 \rangle_\alpha$  direction ( $//$  to  $\langle 110 \rangle_\gamma$ , and the other orthogonal direction (in the plane of the broad face and perpendicular to the long direction) is  $\langle \bar{1}12 \rangle_\alpha$ , (which is parallel to  $\langle 11\bar{2} \rangle_A$ ).

### 3.4. SUMMARY AND DISCUSSION

#### 3.4.1. Morphology of Lath Martensite:

As illustrated in preceding sections, the microstructure of quenched low alloy-low carbon steels is termed "lath martensite" in recognition of the fact that the individual crystals of martensite are lath-like as distinct from the characteristic lenticular "plates" which form in high carbon steels. The laths are about 0.1-0.5  $\mu\text{m}$  in width, 1.0-5.0  $\mu\text{m}$  in height and 10-30  $\mu\text{m}$  in length and are generally larger the lower the carbon content. A typical prior austenite grain will transform to about  $10^4$  to  $10^5$  laths which are arranged in a complex pattern to minimize the strain energy resulting from the local shape changes and the overall volume change of the transformation. The laths arrange themselves in groups or packets which take up each of the 4 crystallographic variants.

The lath shaped martensite single crystals have curved ends and parallel boundaries with interlath continuous films of retained austenite. The martensite contains a high density of dislocations to provide high level accommodation of the stresses created by the transformation. The dislocation density appears to increase as the carbon content of the alloys increases because of the greater magnitude of the principal stresses which must be accommodated. The dislocation density achieved a value estimated to be around  $10^{12}$   $\text{cm}/\text{cm}^3$  in 0.3 wt% carbon alloy.

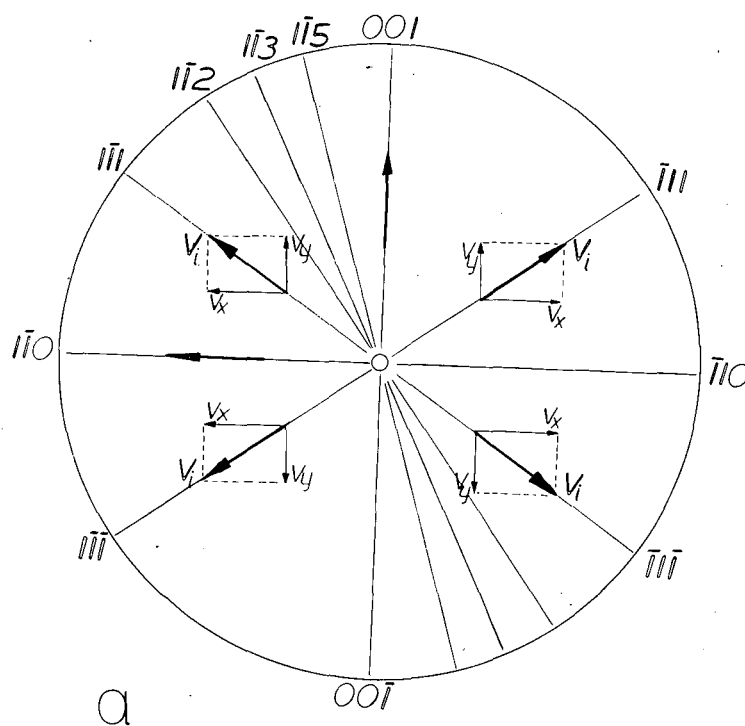
The retained austenite films, present at the boundaries, are mostly continuous and have widths varying between 50-200 Å (sometimes extending up to 500 Å). There could not be any direct correlation made between austenite thickness and the lath width. Nonetheless it is observed that the films are wider in lower carbon alloys. Retained austenite is also highly deformed and has a defect density increasing up to  $10^{14}$  cm/cm<sup>3</sup> in 0.3 wt% C alloys.

Extensive autotempering occurs in the alloys. The  $M_s$  and  $M_f$  temperatures are high so that carbon redistribution can occur during and even after the completion of the transformation to form carbon clusters both within the martensite laths and at the dislocations at the boundaries.

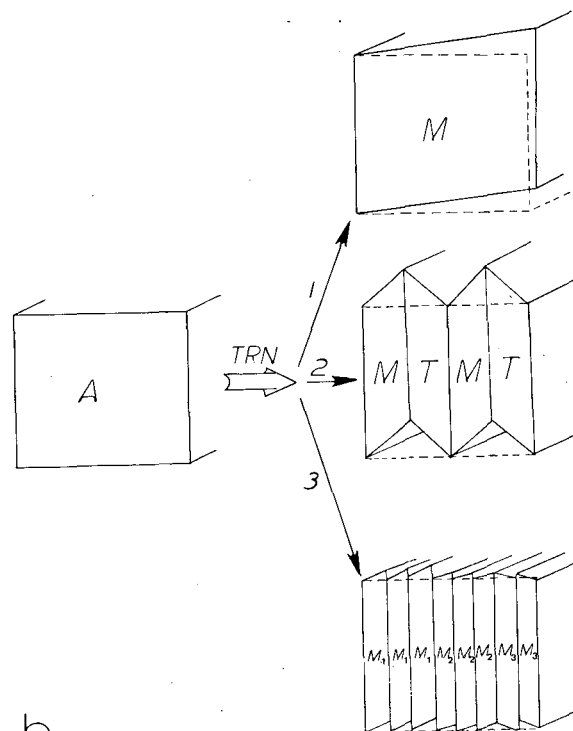
#### 3.4.2. Crystallography:

Since transformation from austenite to martensite involves principal shear as well as dilatational stresses<sup>(1-4)</sup> (volume increase) a net strain is created during the transformation. This can be accommodated by many means, such as by slip<sup>(15,33)</sup> or twinning<sup>(17,34,51,56)</sup> in martensite, deformation in retained austenite, formation of packets of different austenite variants,<sup>(99)</sup> and finally by various lath arrangements within a packet.<sup>(39,40,93,97-99)</sup>

The minimization of the total shear by individual martensite units may be analyzed schematically as shown in Fig. 22. If a large block of original austenite transforms into martensite, there will be a large strain created after



a



b

XBL 825-9885

Fig. 22. (a) Analysis of the principal shear vector  $V_i$  on a  $(110)_M$  stereographic projection.  $180^\circ$  rotation if  $V_i$  would create no shear strain over the number of laths, e.g., between  $[\bar{1}11]$  and  $[1\bar{1}\bar{1}]$  orientations. (b) Shear process of a block of original austenite, A, into either a block of martensite, M (case-1), twin related laths (case-2) (no retained austenite at the boundary), or to the martensite laths in different orientation as stacks (case-3) with retained austenite between them.

the transformation as a result of the shape change. This strain can be reduced if the original block of austenite is broken up into several smaller units upon transformation which then assume different crystallographic arrangements in the resultant structure. This may happen by a change in the direction of the principal shear vector  $V_1$  confined to each unit as shown on a stereographic projection in Fig. 22-a.

The simplest situation is when the adjacent two units are twin related, i.e.,  $V_1$  is in  $[111]_M$  and  $V_2$  is in  $[\bar{1}\bar{1}\bar{1}]_M$  orientation. Then the net shear over the two laths will be zero as schematically shown in Fig. 22-b, case-2). Although not very often this situation was observed in the present alloy system. The twin related laths were wider and had relatively low dislocation density and lacked the other morphological features usually seen otherwise due to auto-tempering. This may mean that they may have formed at the beginning of the transformation when there was a large driving force available and relatively less obstacles (such as boundaries, dislocations) were present. Once one lath has nucleated and grown, the stresses ahead of the boundary is so large it initiates the nucleation of the next lath in such a way that the principal shear will be in opposite direction (Fig. 22 - 2nd case). This way the net shear will be zero over the two laths. Then there is no retained austenite left between the laths (e.g., Fig. 9).



There will be more nucleation sites available for the martensite crystals as the temperature is decreased. When these laths grow, retained austenite is left between them (due to some stabilization mechanisms involved as discussed in Part-II). Then there is no direct effect of one lath to initiate the next in twin orientation. The stresses created by the formation and the growth of the first lath are partly accommodated by this austenite retained behind the boundary. There are probably small residual stresses left which may help to initiate the formation of the next lath. The overall stresses created, however, by those laths within the same region of a packet becomes so large and is not totally accommodated by the retained austenite. Therefore, an abrupt change occurs in the orientation of the laths (around  $\langle 110 \rangle_M$  which is common to all laths). The new orientation is such that the stresses created by those several laths are decreased to some extent (Fig. 22-a and 3rd case in b). The laths in the new orientation and the austenite may assume either a new orientation relationship or a variant of the same orientation relationship (e.g., K-S or N-W).

The situation when the principal shear vector in the first lath is in  $\langle \bar{1}\bar{1}\bar{1} \rangle_M$  direction and in the next one in  $\langle 1\bar{1}\bar{1} \rangle_M$  direction is desirable as described in Fig. 22-a.

This in fact corresponds to a twin variant of Kurdjumov-Sachs orientation relationship. The earlier interpretation (40) about the nature of the relative orientation of adjacent laths was that in a stack of laths in  $\langle 111 \rangle_M$  orientation shear vector in each lath assumes different  $\langle 111 \rangle_M$  direction so that over n number of laths the total rotation of the shear vector around  $\langle 110 \rangle_M$  common direction is completed. Therefore, the overall strain would be zero. This idealized situation rarely or never happens in reality. As the tilting experiments revealed that the laths cluster around certain poles in a packet (as stacks) and they have slight misorientation between them. (The reason for this misorientation will be explained in a later paragraph.)

A similar configuration, however, occurs between the packets. Since the system overall tends to go to a lower energy configuration, the packets themselves arrange in such a way to contribute to this process. It has been ascertained by microdiffraction that the packets are actually different  $\{111\}_A$  variants. Again from Fig. 22 assuming successive packets have  $\{111\}$ ,  $\{11\bar{1}\}$ , etc., variants, then the total strain over the whole austenite grain will be minimized.

There can be different orientation relationships between the individual martensite laths and the retained austenite with an  $\{011\}_M // \{111\}_A$  common boundaries in a packet. There are overall 12 variants of orientation relationships possible

(6 for K-S, 3 for N-W, and 3 for G-T) within a single packet with a particular  $\{111\}_A$  habit. Therefore, there may be a number of situations possible for the relative orientations of the adjacent laths with respect to each other. Six variants of K-S orientation relationship with  $(110)_M // (111)_A$  are shown in Fig. 23. The possible N-W, K-S and G-T orientation relationships given in Section 3.3.3., lead to the following situations:

(i) If there is a  $70^\circ$  or  $180^\circ$  angle between two adjacent laths then they are twin related (e.g., the situation between 1-4, 2-5 and 3-6 in Fig. 23).

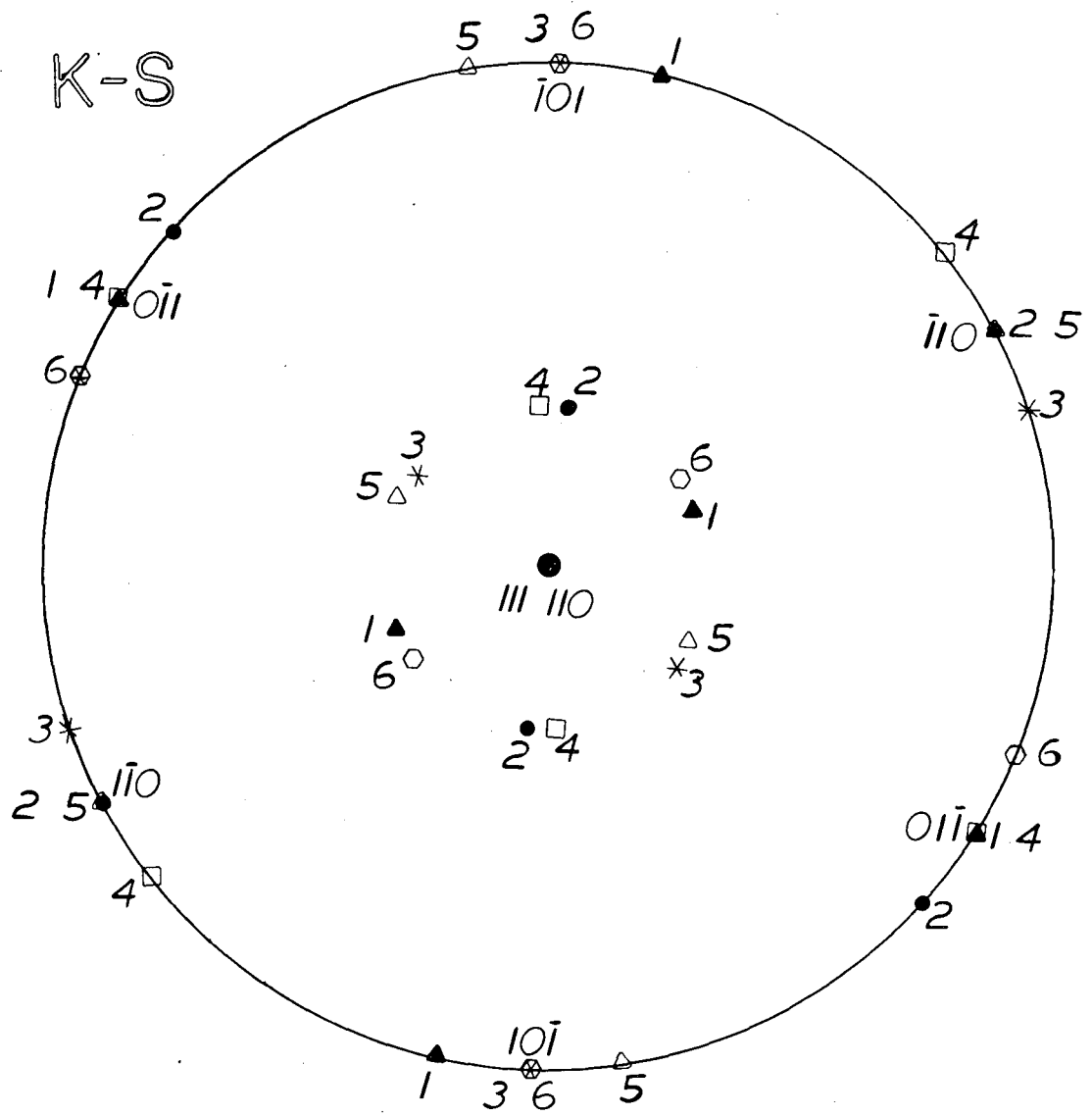
(ii) If there is only  $10^\circ$  angle, then the adjacent laths are variants of K-S (or N-W) (e.g., 1-5, 3-4 and 2-6). The same is true if the angle is  $60^\circ$  (1-2, 1-3, 4-5, 4-6, 2-3, 5-6) or  $50^\circ$  (1-6, 3-4, 2-5, as shown in Fig. 23).

(iii) If the angle is  $5^\circ$  in each direction, then each lath is in either K-S or N-W orientation relation (one variant of each) with the austenite. This is also true if the angle is  $55^\circ$  or  $65^\circ$ .

(iv) If there is  $2.5^\circ$  angle then each lath obeys G-T orientation relationship (true also for angles  $57.5$ ,  $52.5$ ,  $7.5$ ,  $62.5$ ,  $72.5$ ).

(v) Different combinations of the above cases may also occur.

Many of the above cases have been observed in the present alloy system. Diffraction analyses revealed that



VARIANTS

- |   |   |
|---|---|
| ▲ $\bar{1}\bar{1}\bar{1}_M // 0\bar{1}\bar{1}_A$ ---- 1 | □ $\bar{1}\bar{1}\bar{1}_M // 0\bar{1}\bar{1}_A$ ---- 4 |
| ● $\bar{1}\bar{1}\bar{1}_M // \bar{1}\bar{1}0_A$ ---- 2 | △ $\bar{1}\bar{1}\bar{1}_M // \bar{1}\bar{1}0_A$ ---- 5 |
| * $\bar{1}\bar{1}\bar{1}_M // 10\bar{1}_A$ ---- 3       | ○ $\bar{1}\bar{1}\bar{1}_M // 10\bar{1}_A$ ---- 6       |

XBL 825-9883

Fig. 23. Analysis of six-variants of Kurdjumov-Sachs O.R. when  $(111)_A // (110)_M$ . The stereographic projections belonging to six variants are superimposed onto each other to reveal the angular interrelationship between them.

parallel laths of one, two or more orientations in each packet can be present. For instance in Fig. 13, such a situation is shown where in the SAD pattern there are four martensite zones and one austenite zone with a common  $\langle 110 \rangle_M // \langle 111 \rangle_A$  direction. Therefore, there are four different orientations of martensite within that region of a packet. Dark field analyses made using the reflections belonging to different zone axes revealed contrast changes in those laths belonging to the same zone (an experiment necessary in such complex configurations to distinguish between different variants). It should be also reminded that, in practice, it is difficult to distinguish K-S variants which have generated one N-W (or G-T) variant. It is necessary to have a configuration of the foil where the instant electron beam is perpendicular to  $\langle 110 \rangle_M // \langle 111 \rangle_A$  common direction. In such a case, the cross-section of the packet in the foil plane will be parallel to the habit plane of the laths and there will generally be only one lath lying in that cross-section. In addition, as shown in an example in Fig. 19 tilting the foil in the direction perpendicular to common  $\langle 110 \rangle_M$  and taking microdiffraction information from both austenite and martensite for the correct identification of the orientation relationships is also necessary. There is, however, always discrepancies due to the lattice relaxations which may change the local orientation. The microdiffraction patterns taken from different sites within a

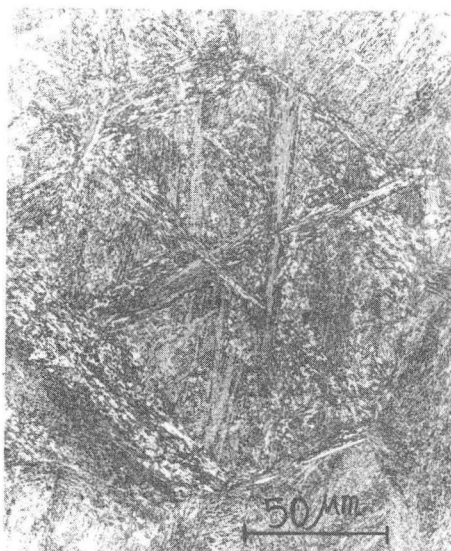
particular lath showed that the misorientations scatter only within a degree.

### 3.4.3. Formation of Laths:

The reason why so many orientation relationships may exist within a given packet may be attributed to the increased variants available for the laths during the nucleation. As discussed in the previous section, the system always tries to minimize the stresses and different variants of the orientation relationships partially fulfill this requirement by decreasing the magnitude of the overall principal shear vector. It has been ascertained that the long directions of the laths are in  $\langle 111 \rangle_M$  direction. Having  $(110)_M // (111)_A$  habit, then, the austenite has its  $\langle 110 \rangle_A$  direction parallel to the film plane. Both of these directions are close-packed directions in martensite and austenite, respectively. Therefore,  $\langle 111 \rangle_M$  is likely to be the easy growth direction in martensite.

During cooling, nucleation probably starts at the strain centers (embryos) in austenite (or at the boundaries) just below the  $M_s$  temperature. The critical nuclei then, having a certain orientation with austenite, start growing slowly in  $\langle 110 \rangle_M$  and fast in  $\langle 111 \rangle_M$ . When the growth is stopped, the austenite is stabilized ahead of the interface because of the large strain buildup. Adjacent laths nucleate by the aid of this strain already available near

①



POSSIBLE SEQUENCE OF FORMATION OF PACKETS

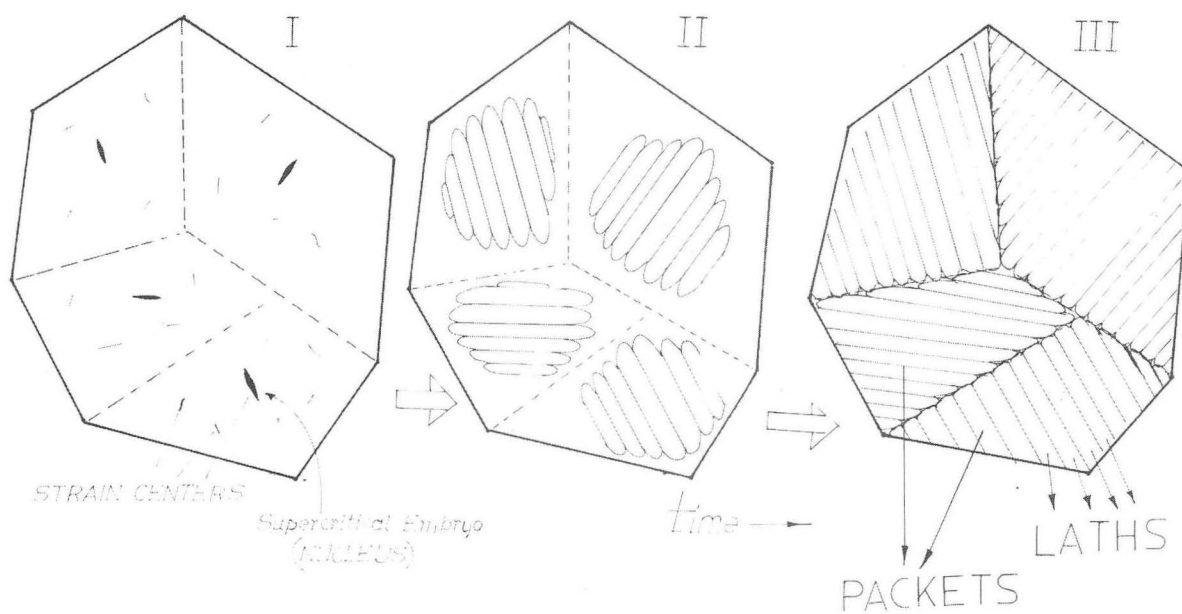


Fig. 24. Possible sequence of growth of laths and subsequent formation of packets in an austenite grain.

XBB 817-7035

the boundary and grow assuming a new orientation (or a variant of the old). The austenite is then trapped between them. This progresses until all the packet is filled with parallel laths. Similar process also occurs in other packets of parallel laths which are themselves different  $\{111\}_A$  variants to finally fill the austenite grain (see Fig. 24 for illustration).

### 3.5. CONCLUSIONS

(i) The microstructures of experimental low and medium carbon low alloy steels consist of dislocated, autotempered "lath" martensite with thin film retained austenite at the boundaries, except where twin related laths occur.

(ii) Individual martensite crystals occur as laths, 0.1-0.5  $\mu\text{m}$  width,  $\sim 5$   $\mu\text{m}$  height and 10-30  $\mu\text{m}$  in length, with straight parallel boundaries. Stacks of laths with different  $\{111\}_\gamma$  transformation variants form packets.

(iii) Adjacent laths in a particular packet have one  $\langle 110 \rangle_M$  direction in common and may be rotated about this axis with small angles ( $0^\circ \leq \theta < 10^\circ$ ) or large angles ( $\theta > 20^\circ$ ) (i.e., adjacent laths in  $\langle 111 \rangle$ ,  $\langle 100 \rangle$ ,  $\langle 112 \rangle$ ,  $\langle 113 \rangle$ , etc., orientations with common  $(110)_\alpha$ ). The angle of rotation may even be  $\pi$  in which case the laths are twin related. This configuration is attributed to the necessity of strain minimization during the successive formation (nucleation) and growth of individual martensite crystals.



(iv) Orientation Relationships between austenite and martensite all lie between K-S and N-W, G-T being the most frequently observed; this is perhaps due to the greater availability of variants during nucleation of the laths.

(v) The macroscopic habit plane has been identified to be near  $(111)_{\gamma}$  (within  $5^{\circ}$ ) which is parallel to  $(110)_{\alpha'}$ .

(vi) The long directions of the laths have been identified to be parallel to  $\langle 111 \rangle_{\alpha'}$ , which is parallel to  $\langle 110 \rangle_{\gamma}$  and broad faces parallel to  $(110)_{\alpha'}$ .

(vii) It is hypothesized that upon quenching several laths nucleate as discrete units in different parts of the austenite. Those which nucleate first establish the austenite variant, i.e., a particular  $\{111\}_A$ , followed by the other laths as they nucleate and grow one after another to form packets. Retained austenite is trapped at the boundaries. The relative orientations between adjacent laths, the orientation relations between austenite and martensite, the packet orientations, the structural dislocations both in martensite and austenite and the rare microstructural twins in martensite are all arranged to minimize the overall strain (shear and dilatational) created during the transformation.

## 4. PART-II

## THIN FILM RETAINED AUSTENITE

## 4.1. INTRODUCTION

Plate martensitic structures as encountered in high carbon (or high nitrogen)-high alloy steels, which usually have  $M_s$  temperatures below ambient have been studied extensively. (14-18,50-60,106-111) These ferrous martensites contain retained austenite as "blocky" islands filling up the space between the lenticular twinned martensitic plates. (6,15-17,33,34) Its microstructure (14-16,30-36) and crystallographic relationships (64-67) with martensite are well documented. The existence of this phase, which amounts to more than 10% by volume is affected by heat treatment, (9, 10,62,63,106-111) composition, (9,10,30-33,81) and stress state. (107,115-118)

However, previous investigators working on the morphologic and crystallographical aspects of low alloy steels with or without carbon did not identify retained austenite in the lath martensitic structure. (15,16,33,39, 80-87) (One may note that in published papers of the studies involving lath martensitic steels containing carbon one can recognize thin films of retained austenite in the micrographs.) It was not until recently that retained austenite has been identified as "thin films" at the lath boundaries in the medium carbon-low alloy experimental steels (45,112) (similar composition as the present study) having  $M_s$  above

room temperature. Following this finding, limited studies concentrated on the effect of this phase on the mechanical properties of those steels, (41-45,61,112-114) but little systematic work has been undertaken to explain its occurrence. (40,45)

One of the objectives of the present research was to explain the existence and behavior of austenite in the present series of low carbon steels in light of concepts developed to apply to high carbon steels. The stabilization of retained austenite could be accounted for by partitioning of alloying elements, especially carbon, during the  $\gamma$  to  $\alpha'$  transformation as the  $M_s$  temperatures of the present alloys are well above room temperature (usually above 200°C). Since chemical partitioning in the  $M_s$ - $M_f$  range would partly explain the presence of retained austenite this possibility was tested using sophisticated techniques to check for partitioning of alloying elements between martensite and austenite and obtain a composition profile across the microstructure.

#### 4.2. TEM IDENTIFICATION AND THE OCCURRENCE OF RETAINED AUSTENITE

Retained austenite in these steels is in the form of thin layers or films on the boundaries of the roughly parallelepiped martensite crystals (laths) arranged in packets. They are usually continuous and found at packet boundaries and preaustenite grain boundaries as well. The thickness of the films varies from very thin ( $\sim 50 \text{ \AA}$ ) to very thick ( $400 \text{ \AA}$ ) (but usually in the  $150\text{-}200 \text{ \AA}$  range) depending on factors such as the size of the laths (larger the laths thicker the films), relative orientation of the adjacent laths and the alloy content of the steel (increasing with austenite stabilizers such as Mn or Ni).<sup>(45,120)</sup>

Significant variations occur in the amount of retained austenite within a given specimen either as-quenched or after low temperature (e.g.,  $200^\circ\text{C}$ ) aging.<sup>(89)</sup> In some regions there is no retained austenite present at the lath boundaries perhaps because of the influence of the adjacent lath orientations.<sup>(99)</sup> For example, in Fig. 9 retained austenite was found in the packet B containing laths projected edge-on having alternately bright-dark contrast. These laths are "twin related" and they are self accommodating. In the same figure in packets A and C, surrounding the central packet B, the laths are not twin related and indeed detailed analysis of these packets confirm the presence of retained austenite. In low carbon alloys, the laths are more regular in shape

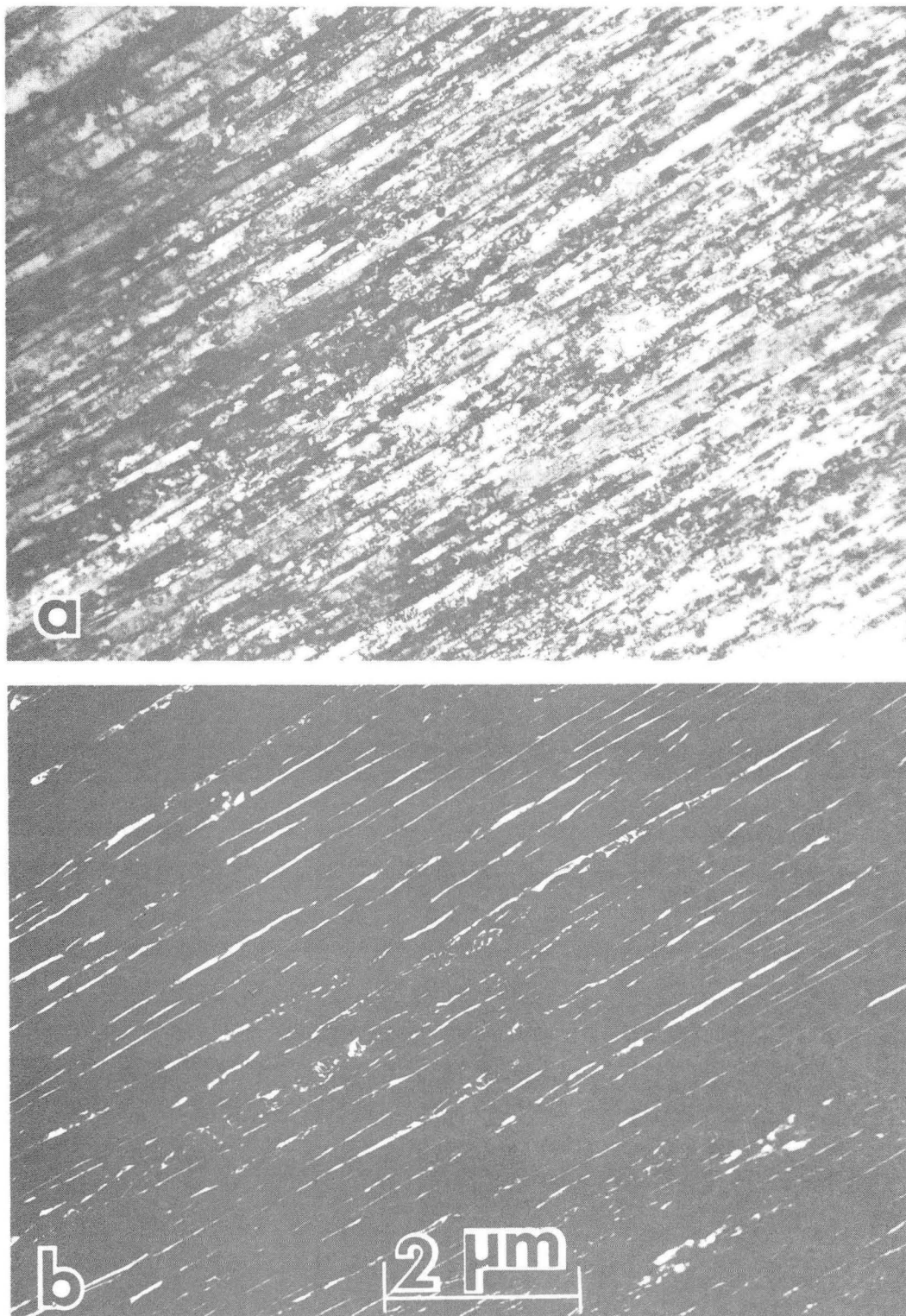


Fig. 25. General view of the microstructure on 0.1 C containing alloy (Alloy 2) showing the parallel lath morphology with retained austenite (a) BF, and (b) DF images. In low carbon alloys the laths have more regular shape and thicker retained austenite films than 0.3 C alloys.

XBB 800-14347

and the parallelism of the boundaries is more pronounced. The retained austenite films are much more uniform throughout a particular packet (for example, see Fig. 25).

Retained austenite films are often very heavily deformed as may be discerned from the high magnification micrographs shown in Fig. 26 which were taken from a region containing exceptionally thick retained austenite films ( $\sim 450 \text{ \AA}$ ). Retained austenite has a dark contrast in BF image when oriented properly to a zone axis. There is also strain contrast arising from the high density of imperfection due to heavy deformation of austenite which has taken place, to accommodate the stresses created during the  $\gamma$  to  $\alpha'$  transformation. This is especially noticeable in DF images (e.g., see Fig. 26-b). Defects observed in retained austenite films give contrast similar to dislocations, stacking fault ribbons and ledges. No defect analysis could be done because of the limited size of the films. However, the dislocation density was estimated to be around  $10^{12}$ - $10^{14} \text{ cm/cm}^3$ .

The total amount of retained austenite in low carbon steels is very low, i.e., 2-5 vol% as determined by X-ray diffraction technique. (120,121) Therefore, considerable attention is required to detect retained austenite in the TEM. It is often difficult to identify retained austenite in BF images from other various features in the microstructure because of the lack of regular contrast. Therefore, careful electron diffraction and DF analyses have to be

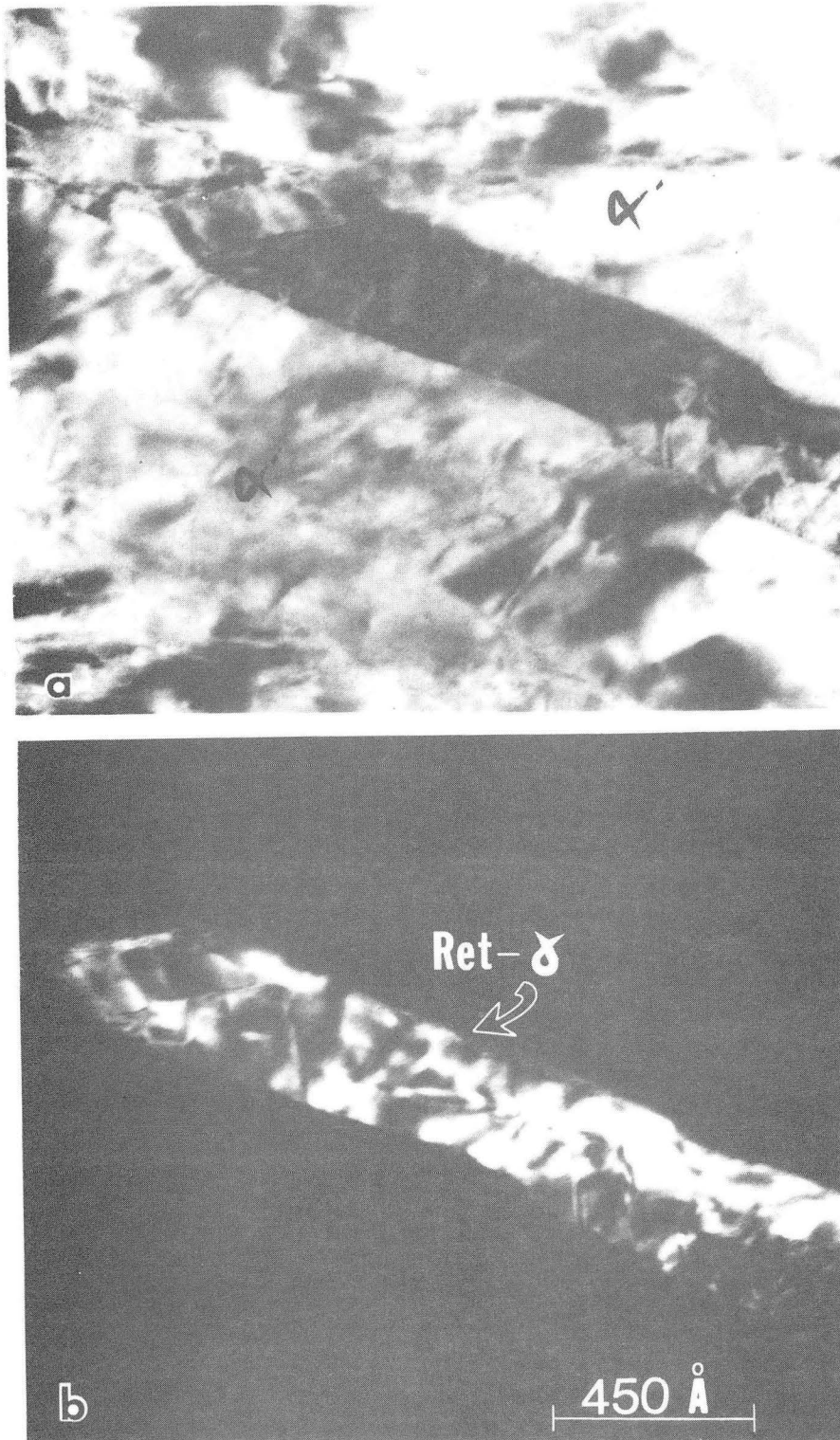


Fig. 26. High magnification micrographs of a region containing thick retained austenite film, show the contrast change due to defects arising from heavy deformation. (a) BF and (b) DF.

XBB 823-2326

performed including tilting the foil to different orientations to provide the best contrast.

Interpretation of diffraction patterns is also often difficult and sometimes puzzling since they usually contain reflections from several features in the microstructure such as martensite laths having slightly different orientations, from autotempered carbides, internal or multiple twins in martensite, the retained austenite itself, and also from double diffraction (formed by the elastically diffracted electrons from the above features interacting to form extra reflections). In Fig. 27, several of the most commonly observed diffraction patterns are plotted schematically. Here, for clarity, two patterns, one from  $\alpha'$  and the other from  $\gamma$ , are indicated. In reality, if one uses a selected area aperture, one may obtain reflections from many laths in different orientations within the same packet. Of course, all austenite will be in the same orientation and contrast as long as the observation is contained within the same preaustenite grain.

The most commonly observed case is a composite triple diffraction pattern caused by two sets of martensite laths, i.e.,  $\langle 111 \rangle_{\alpha'}$  and  $\langle 100 \rangle_{\alpha'}$ , and a third pattern due to the austenite, i.e.,  $\langle 110 \rangle_{\gamma}$  (Fig. 28-a). In this configuration the reflection to be used for the DF analysis of retained austenite is  $(00\bar{2})_{\gamma}$  which has the largest angular separation ( $\sim 12$  mRad) from the other reflections in the pattern. Once



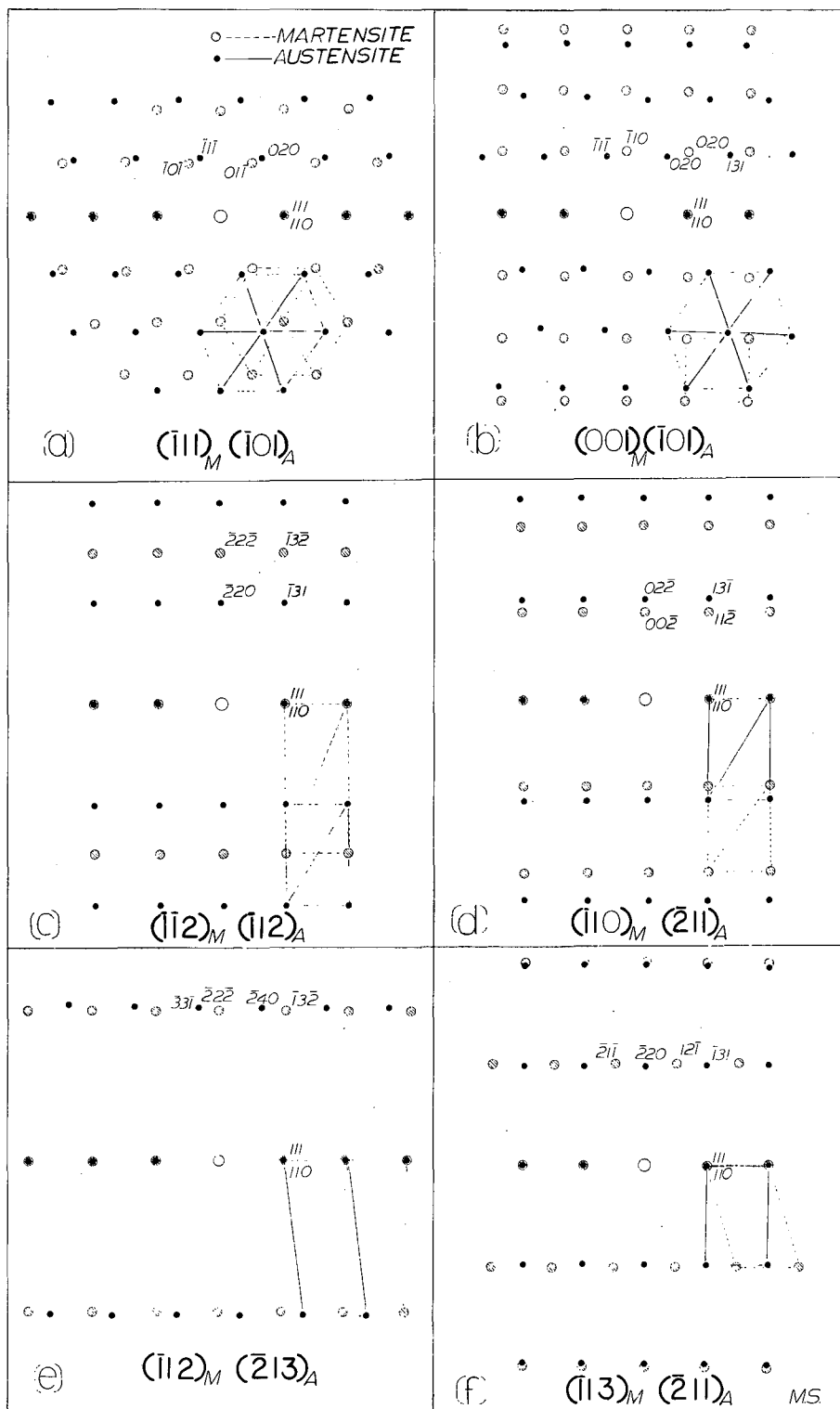


Fig. 27. Schematic illustration of the most commonly observed superimposed diffraction patterns from  $\alpha'$  and  $\gamma$ .  
XBL 823-8592

the various patterns are identified, this reflection can be distinguished and should be used for the DF imaging.

It should also be noted that considerable arching occurs in the pattern as a result of the internal strains and minor orientation differences of the laths.<sup>(120)</sup> Due to the shape factor,<sup>(122)</sup> retained austenite reflections are usually elongated in the  $\langle 111 \rangle_{\gamma}$  direction. For certain orientations of a particular region (not exactly on the  $[110]_{\gamma}$  zone axis but slightly tilted, i.e., 1-2°, towards  $\bar{g}_{200_{\gamma}}$ ) streaking could be observed from the austenite reflections in a direction perpendicular to the long directions of the films (Fig. 28-b and c).

The morphology of retained austenite in various alloys (containing different carbon and other alloying elements) is shown in the BF and DF images in Fig. 29 to reveal the general appearance of this phase in the lath martensitic structures of these alloys.

#### 4.3. CHEMICAL ANALYSIS OF RETAINED AUSTENITE

4.3.1. Experimental Techniques. Since austenite could be stabilized by carbon partitioning during the transformation (chemical stabilization)<sup>(45)</sup> technique capable of resolving C in retained austenite under the exceptionally severe conditions of the present problem, must be employed to measure the extent of carbon enrichment. The difficulties involved are:

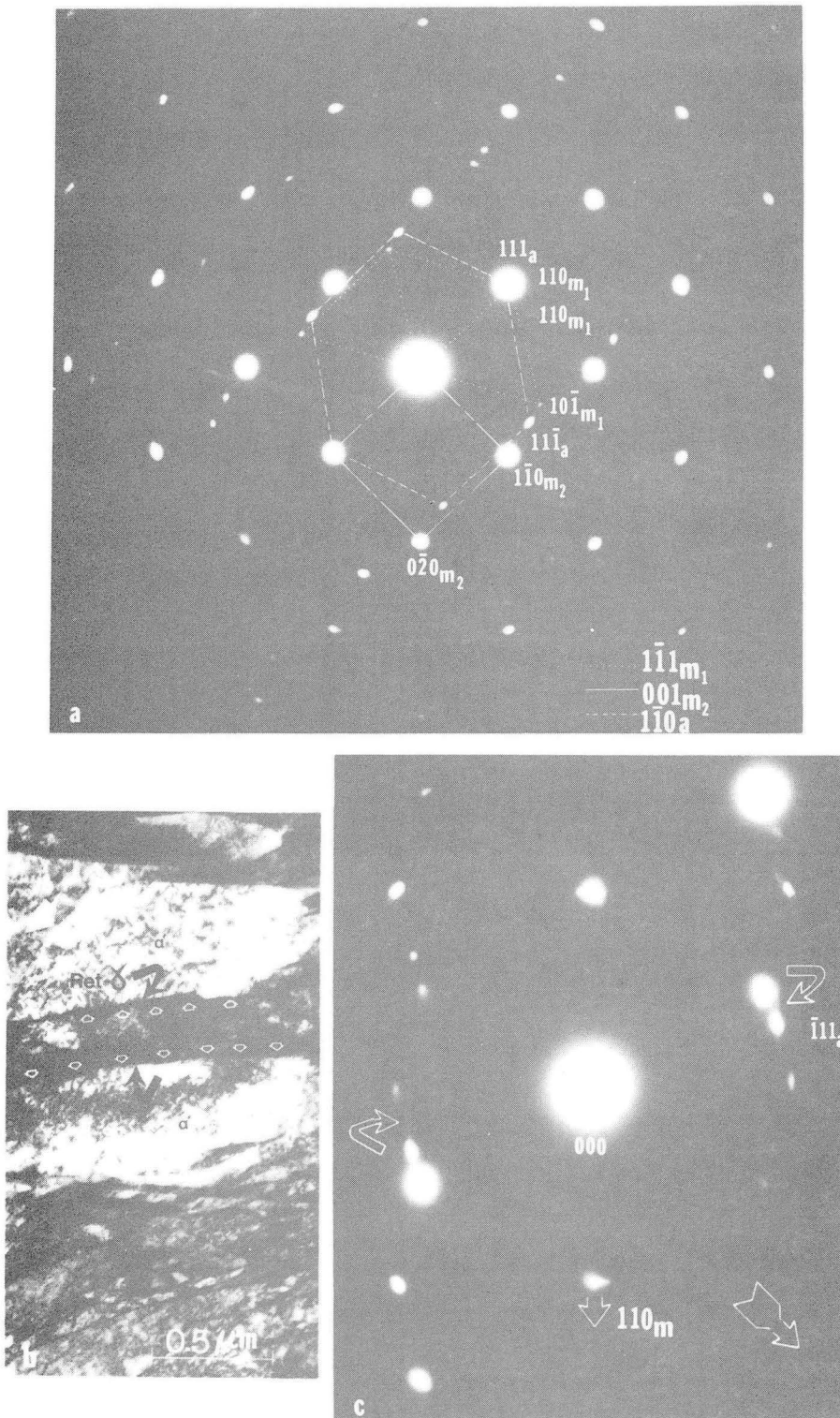


Fig. 28. (a) Frequently encountered diffraction pattern;  $\langle 111 \rangle_M / \langle 100 \rangle_M / \langle 110 \rangle_A$ . (b) Due to the long and thin shape of the austenite films "streaking" occurs in the SAD pattern in  $\langle 111 \rangle_A$ . The effect is seen when the foil is slightly tilted in the direction shown by the arrow in (c) (here about  $1^\circ$ ).

XBB 824-3501

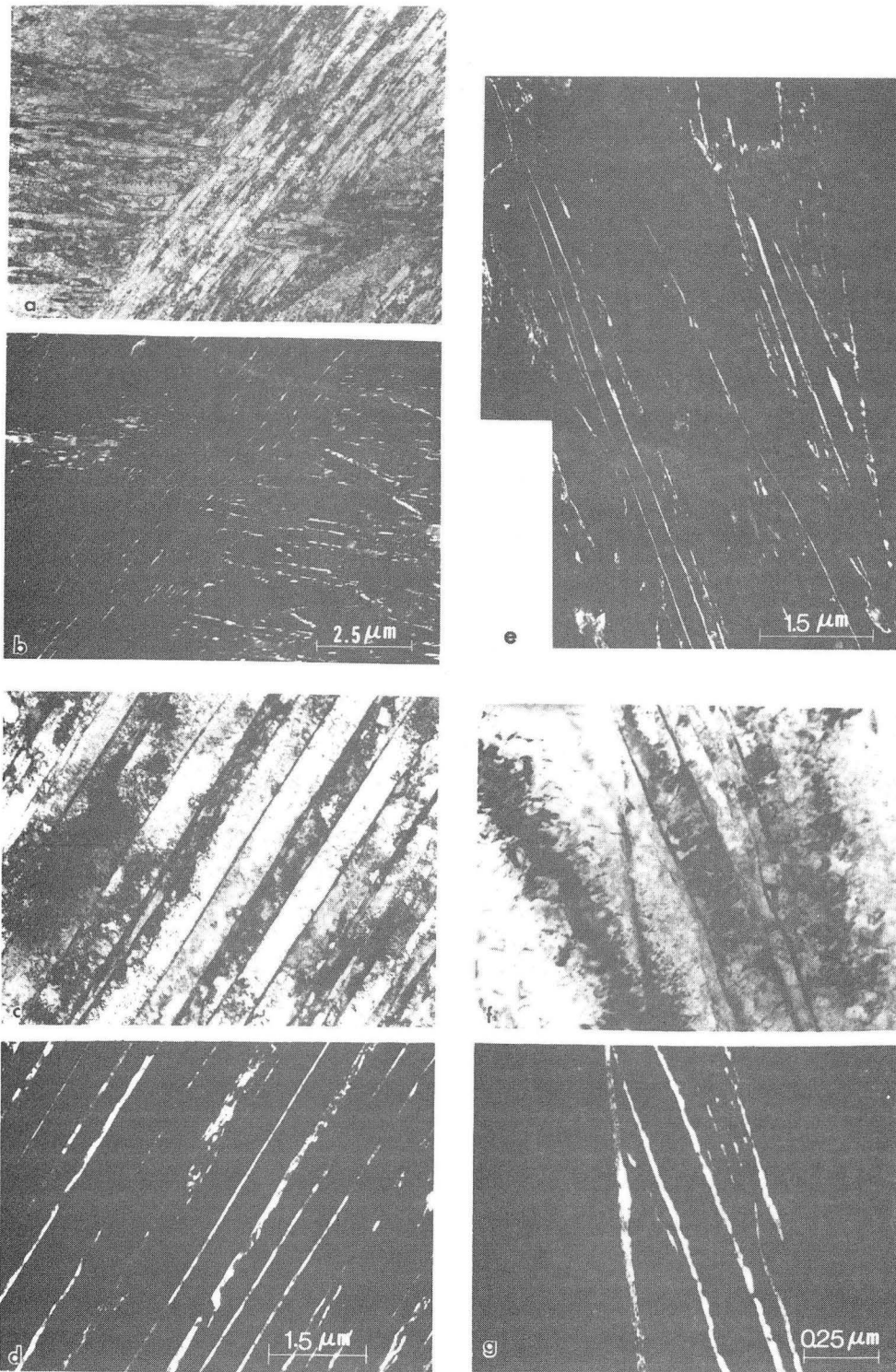


Fig. 29. General appearance of retained austenite in different alloys. (a) BF and (b) DF (Alloy 3), (c) BF and (d) DF (Alloy 2), (e) DF (Alloy 4), (f) BF and (g) DF (Alloy 5).

XBB 823-2327

- (i) The amount of retained austenite is low (1-5 vol%).
- (ii) The retained austenite is in the form of narrow films ( $\sim 200$  Å thick) between the martensite laths. Hence the technique must involve high spatial resolutions.
- (iii) The C content could be no more than a few at% in retained austenite and only 0.47-1.40 at% in the matrix.

For these reasons, lattice parameter measurement by conventional X-ray diffraction<sup>(123)</sup> could not be used as the intensities of the diffraction peaks (111) and (112) would be extremely weak and broad and lost in the background.<sup>(121)</sup> Also, since C is a light element, direct techniques such as X-ray micro-analysis could not be used, since the weak  $C$ ,  $K_{\alpha}$  and  $K_{\beta}$  peaks are masked by the intense Brehmsstrahlung at the lower end of the spectrum.

Nonetheless, several sophisticated techniques are available to obtain an estimate of the C content in local regions. High Resolution Lattice Fringe Imaging (HRLF<sub>I</sub>)<sup>(125)</sup> and Convergent Beam Electron Diffraction (CBED)<sup>(126)</sup> can be used to measure the local lattice parameter and relate it to the carbon content contained within that region. Other more direct techniques are Electron Energy Loss Spectroscopy (EELS)<sup>(127)</sup> and Field Ion Microscopy - Atom Probe Analysis (FIM-APA)<sup>(46,47)</sup> where chemical composition of a particular region is determined by direct analysis of the chemical

species present. All four of these techniques were explored, but the CBED and FIM-APA proved to be the most useful. The results obtained by these two techniques will be discussed in detail in the next sections. Following immediately is a brief discussion on the individual techniques mentioned above.

a. Indirect Techniques

(i) High Resolution Lattice Imaging: Measurements of the local lattice parameter<sup>(40,128,129)</sup> by HRLI suggested that the carbon content in austenite could be between 0.41-1.04%<sup>(45)</sup> in a 0.3C bulk steel. This result was deduced from the analysis of the fringe spacings of austenite (using that of martensite as reference) by Laser Optical Diffraction<sup>(125)</sup> made on the negative film which is taken by simultaneous imaging of the lattice fringes from  $(101)_M$  and  $(111)_A$  planes. However, high uncertainties exist in this method due, e.g., to the amount of defocussing, local thickness variations (because of preferential etching of either martensite or austenite), effect of strain in austenite (i.e., this phase is highly deformed), and the errors and the uncertainties involved in fringe measurements.

(ii) Convergent Beam Electron Diffraction: This method, although indirect, gives an accuracy of 2/10000 in lattice parameter measurements<sup>(126)</sup> when the experimental requirements are met. The CBED method has been utilized successfully in current investigation (see section 4.3.2 below).

b. Direct Techniques

(i) Electron Energy Loss Spectroscopy: Direct quantitative analysis of light elements, such as carbon, can be made by this method. The technique basically involves the study of the angular and energy distribution of high energy electrons which have suffered momentum changes (energy losses) during the passage through a "thin" region of a TEM foil. The resulting Electron Energy Loss spectra i.e., transmitted signal intensity as a function of the energy loss for electrons accepted through the entrance slit contains information about the type and quantities of the elements in the foil. However, this technique revealed its limitations under the severe conditions in its application to the existing problem. Although considerable effort was spent on quantitative analysis of the carbon content in both martensite and austenite phases with the Berkeley spectrometer, (129) carbon (hydrocarbon) contamination, thick foil effects (multiple scattering), and low spatial and energy resolutions limited the carbon detectability to about 2 wt%. (130)

(ii) Field Ion Microscopy-Atom Probe Analysis: FIM-APA has proven to be an appropriate method for estimating point to point carbon levels in steels with martensitic structures. (46,132,133) This is a unique method which has high spatial resolution (atomic resolution) and mass independent sensitivity. (132-137) By this method, it was possible to

analyze quantitatively the carbon and substitutional alloying element (such as Cr, Mn, Ni, Mo) distribution both in martensite and retained austenite (see Section 4.3.3).

#### 4.3.2. CONVERGING BEAM ELECTRON DIFFRACTION-AUSTENITE LATTICE PARAMETER MEASUREMENT

##### a. Experimental Background

Converging Beam Electron Diffraction (CBED) patterns are two-dimensional maps of the diffraction intensity as a function of the inclination between the incident electrons and a particular crystal direction. (126,137) They are normally composed of a series of discs, each one corresponding to a different Bragg reflection (Fig. 30). The intensity variation within the discs carries important information about the specimen orientation, thickness, lattice parameter and other properties of the specimen. (126)

The CBED pattern is obtained as follows: in the TEM mode, one starts by forming an image of the specimen under standard condition and then increase the first condenser lens to its maximum excitation while adjusting the second condenser lens to produce a focussed spot on eucentrically adjusted foil. To form a CBED pattern, the objective aperture is removed and the diffraction mode is selected. The diffraction pattern formed on the back focal plane of the objective lens is composed of discs on the 0<sup>th</sup> order Laue zone and a circle composed of discs on the higher order Laue zones (HOLZ) depending on the particular material



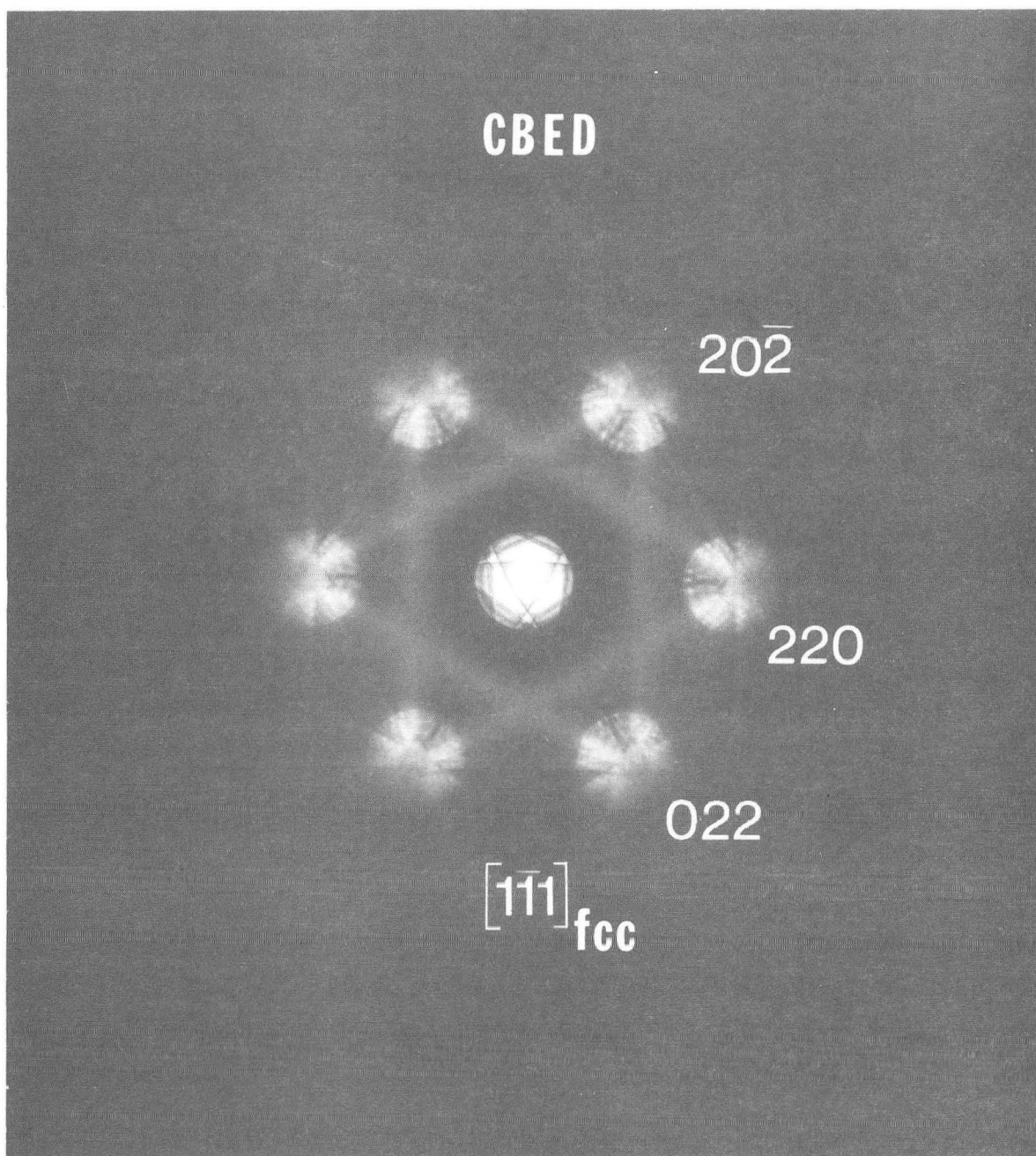


Fig. 30. CBED pattern taken down to (111) zone axis in an fcc crystal (here Ni) showing the three-fold symmetry (at 100 kV). The patterns inside the discs formed by the diffracted beams are due to the HOLZ lines and the pattern in the background is due to Kikuchi lines. XBB 816-5736

used and zone axis chosen (see Fig. 30 for Ni). Disc size is defined by the angle of convergence which is directly proportional to the diameter of the second condenser aperture. Once the CBED pattern is formed, further adjustments are made to obtain a focussed pattern. A 300-400 Å diameter electron probe size can be obtained in the TEM mode and less than 100 Å probe size is possible in the STEM mode in a Phillips 400 microscope.

Requirements for obtaining a useful CBED pattern from a particular material, include uniform thickness and a strain free region. (126) In the present case, martensite has a high dislocation density, and austenite is heavily deformed to accommodate the strains created during martensite growth. Hence it was quite difficult to obtain any CBED pattern with sharp HOLZ (High Order Laue Zone) lines in it, even though considerable effort was taken to optimize the microscope and specimen parameters. However, a foil preparation method called "dipping" (see Section 2.2.2) can be used to preferentially etch the martensite laths and produce austenite films extending like "fingers" from the martensite matrix (Fig. A2-1 in Appendix 2). Retained austenite polished in this way is free from volume constraints and dislocations.

Changes in the lattice parameter of a crystalline material produce shifts in the HOLZ line positions because deviations between the reciprocal lattice points and the Ewald sphere are altered. (126) The small angle approximation

To Bragg's Law, for a cubic material of lattice parameter  $a$  is:

$$\frac{\Delta\theta}{\theta} = \frac{\Delta a}{a}$$

where  $\Delta\theta$  is the change in the line position and  $\Delta a$  is that in the lattice parameter. <sup>(126)</sup> According to the arguments put forward by Steeds, <sup>(126)</sup> accurate measurements (the limit of accuracy being 2/10000) can be made of the changes of the lattice parameter with respect to a known standard with the same crystal structure and close in lattice parameters. The shift in the position of the HOLZ lines with lattice parameter is given by

$$\frac{\Delta\theta}{\theta} = \frac{2}{3}[q_i/p_i - q_{\text{ref}}/p_{\text{ref}}] (8/115)^{\frac{1}{2}} = \frac{\Delta a}{a_{\text{ref}}} \dots (1)$$

where  $q_i$  represents the heights of the triangles at the centers of the discs formed by the HOLZ lines;  $p_i$  the spacing between the equivalent points in the central and any of the 200 discs (Fig. 31);  $(115/8)^{\frac{1}{2}}$  is the radius of the HOLZ ring (i.e.,  $(115/8)^{\frac{1}{2}} = |G_{\bar{5}\bar{3}9}| / |g_{220}|$ ), and a further factor of 2 is introduced because this radius is equivalent to 2.

#### b. Results

The experiments have been performed on a 0.17C/2.05Si steel (alloy 3) which had exceptionally wide austenite strips (see the inset in Fig. A2-1, Appendix 2). High purity (99.99%) Ni ( $a_{\text{Ni}} = 3.5239 \text{ \AA}$ ) has been used as a reference. The result obtained was cross-checked with 99.999% purity Cu ( $a_{\text{Cu}} = 3.6148 \text{ \AA}$ ). <sup>(139)</sup> (Foil from these were made

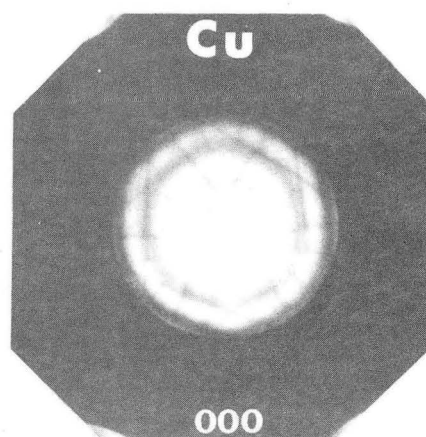
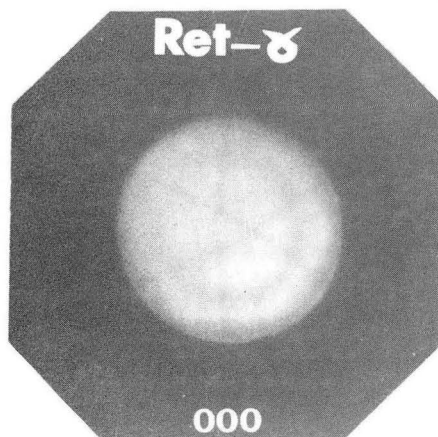
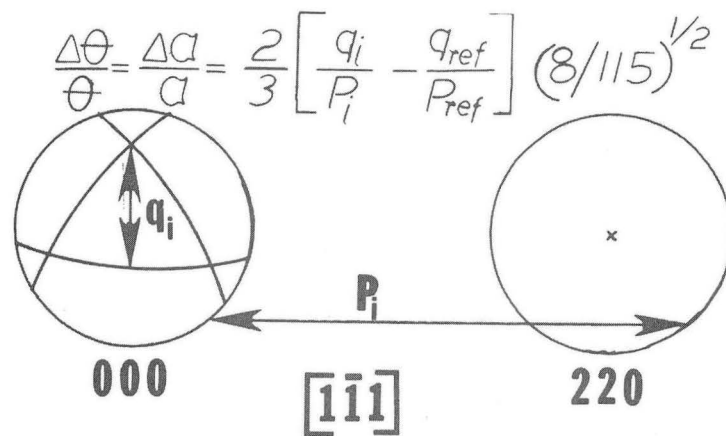
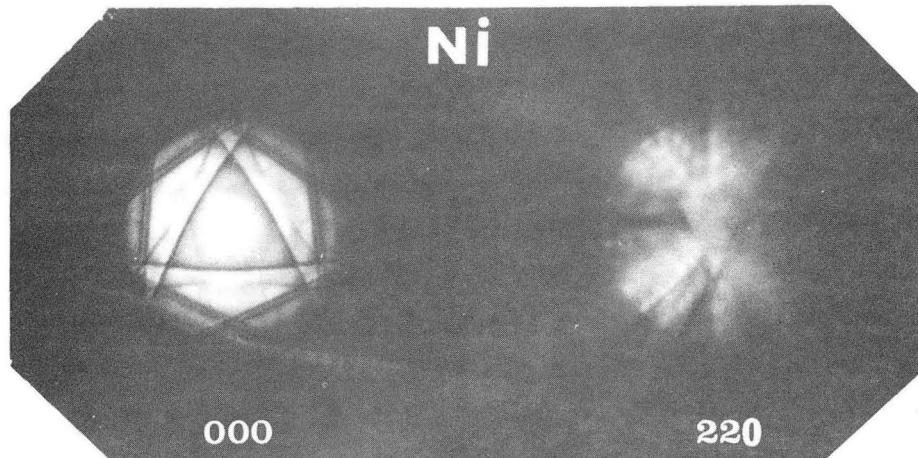


Fig. 31. Patterns show the details inside the discs formed by the forward scattered beam in Ni, retained austenite, and Cu in (111) orientation at 100kV. Note also the description of  $q_i$  and  $p_i$  used in Eqn. (1).

XBB 816-5739

after the annealing treatment.) The lattice parameter of retained austenite which was calculated by this method in a number of experiments performed on different retained austenite films, has been found to be above 3.6000 Å. C content can be found from the following formula which relates the C content to the lattice parameter of retained austenite. (24,140-142)

$$a_{\text{ret-}\gamma} = 3.555 + 0.044 \times \text{wt}\%C \dots\dots\dots(2)$$

Using this formula, a typical value for an average C content in retained austenite (e.g., for  $a_{\text{ret-}\gamma} = 3.6058 \text{ \AA}$ ) can be calculated to be  $1.14 \pm 0.15 \text{ wt}\%$  (or  $\pm \text{at}\%$ ). This value is far above the bulk C concentration (0.17 wt%) of the alloys used for this study. The C content found in this way is an average value corresponding to a local volume of retained austenite which is determined by the diameter of the electron probe size (few hundred Å's). To decrease any uncertainties in the measurements due to high voltage instabilities, the experiments were completed within one week (a voltage instability of 5 volts in 100kV usually occurs in the Berkeley Philips EM400 TEM). Note also in Fig. 32 that the retained austenite CBED pattern shows exactly the same symmetry as the Cu or Ni patterns, i.e., trigonal symmetry in (111) pattern (see also Fig. 30). Therefore, it is concluded that the lattice parameter of retained austenite is isotropic, i.e., no change in lattice

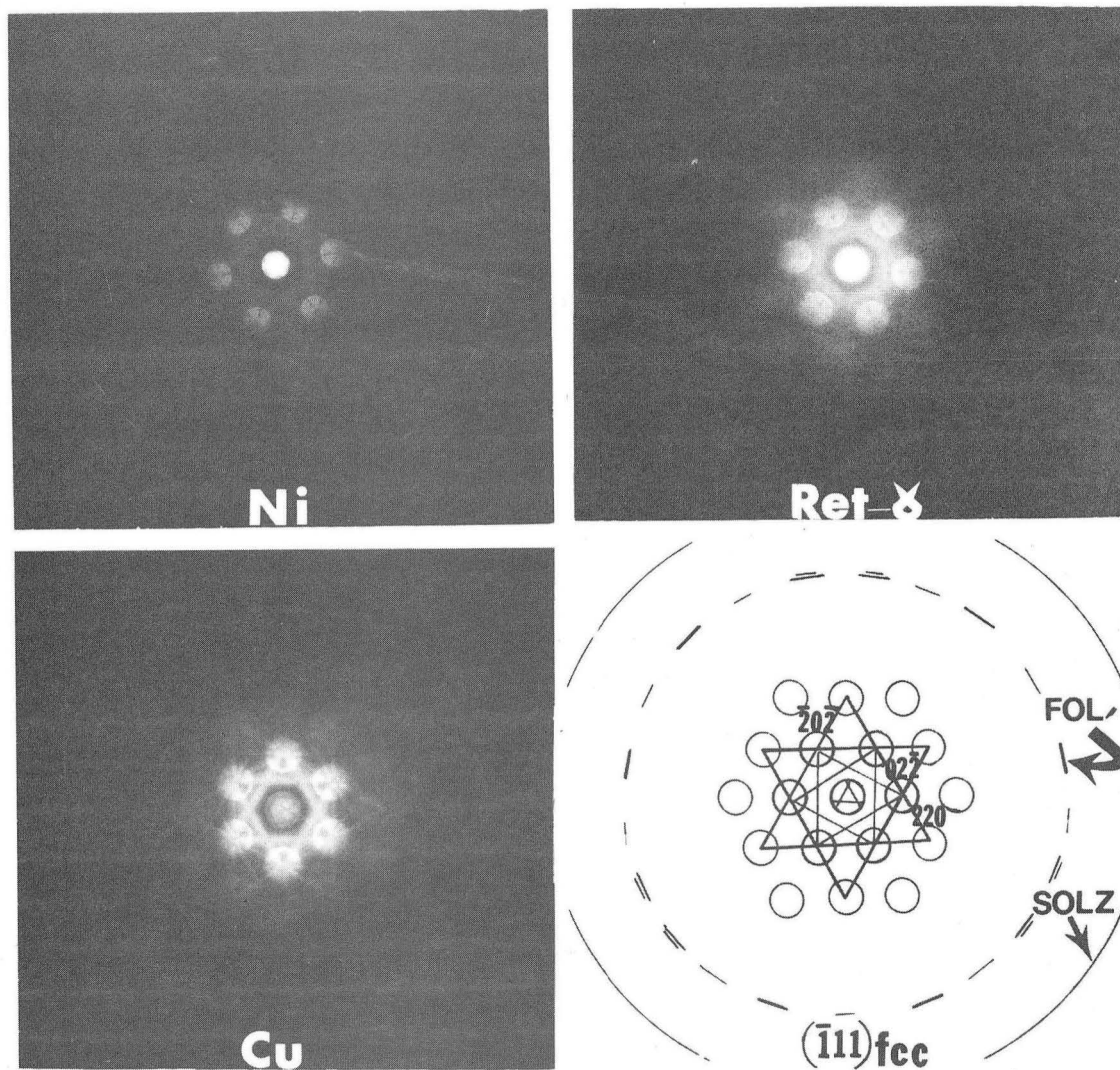



Fig. 32. CBED patterns taken from Ni, retained austenite, and Cu at 100kV showing the higher order Laue zones. All of the patterns are similar to schematic pattern (d), i.e., they have 3-fold symmetry.

MS.  Univ. of Cal., LBL, BERKELEY

XBB 810-11425

parameter with direction due probably to the different octahedral sites occupied by C which could occur in some cases.

Similar attempts were made to measure the lattice parameter of martensite and consequently determine the C content in this phase (see the relation  $a_M$  vs. wt% C in Appendix 2). However, lowering the C content from 0.3 to 0.06 wt% to decrease the dislocation density, changing the heat treatment to produce martensite relatively free of defects, change in accelerating voltage to change the radius of the Ewalds sphere were all unsuccessful. Also, different camera lengths were used, and smaller and brighter electron probes were tried (Philips 400 ST with FEG-ASU with  $d_e < 100 \text{ \AA}$  - at Arizona State University). The results were unsuccessful in obtaining HOLZ lines in the CBP. There is just not enough defect and strain free volume to contribute to the formation of a pattern suitable for lattice parameter measurement (see Appendix 2 for a representative  $(111)_M$  pattern compared to one from retained austenite).

#### 4.3.3. Measurements of Solute Partitioning into Retained Austenite by Field Ion Microscopy-Atom Probe Analysis

##### a. Experimental Background

Line sensitivity of the FIM-AP is independent of mass, so it can be used for analyses of both substitutional alloying elements (Cr, Mn, Ni, etc.) as well as interstitial

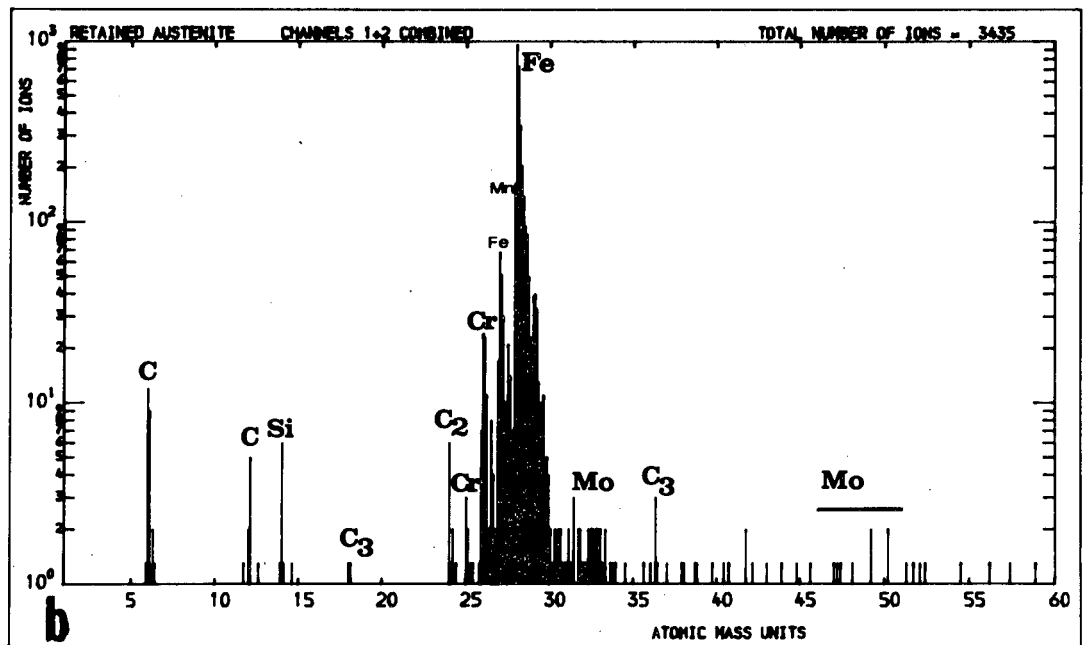
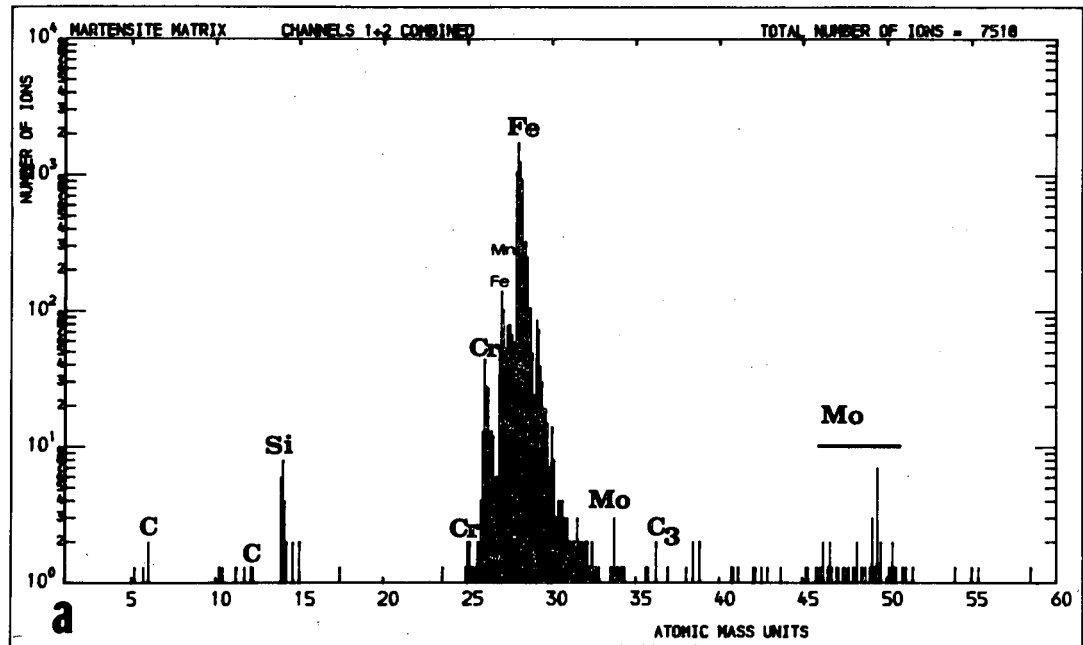


Fig. 33. Typical mass spectra, obtained by Atom Probe Analyzer, from martensite (a) and retained austenite (b) showing the characteristic (m/n) peaks in a 0.3C alloy at 200°C tempered condition (Alloy 4).

XBL 8112-12737



C at high spatial resolution. (40,132,143-145) To illustrate the advantages of the technique, typical mass spectra of the martensite and the austenite phases from an AP Analysis are shown in Figs. 33-a and b from alloy No. 4. The spectra are plotted on a semilogarithmic scale to emphasize the minor peaks due to C, Cr, Mn, and Mo. Note that the C spectrum is particularly complex with peaks at mass-to-charge ratios (m/n) of 6, 12, 18, 24 and 36 due, respectively, to the monomers and polycarbon ions  $C^{++}$ ,  $C^+$ , or  $C_2^{++}$ ,  $C_3^{+++}$ ,  $C_2^+$  and  $C_3$ . It should be noted that the presence of molybdenum somewhat complicates the evaluation of the carbon concentration. The Mo +4 and +5 states have m/n values around 24 and 18 which overlap with  $C_2^+$  and  $C_3^{++}$  peaks, respectively. (46,132,144) It is possible that carbon and molybdenum could be associated in solid solution. If this were the case, then a C-Mo complex ion could possibly be produced, the m/n value of which in the triplet charged state would be around 36, thus overlapping with  $C_3^+$  peak. However, in practice, it is found (46, 144) that the Mo charge states which would give rise to these ambiguities occur extremely rarely (in fact, none was found in an analysis of 7500 ions taken from the martensite phase--see Table 2). If a C-Mo complex ion is formed, it can only be a very small extent, since the nominal level of Mo can be accounted in the +1 and +2 charge states. Although nominal compositions of Cr and Mn are higher, there is no report on C ions associating with these alloying elements in solution or

at the surface of the tip before the field evaporation. Therefore, the C peaks are accepted to be corresponding to pure C species and the analyses have been done accordingly. However, general deconvolution<sup>(46,143)</sup> is always necessary for every C peak as well as for other alloying elements, especially for Mn. Cr is usually evaporated as  $\text{Cr}_{52}^{++}$ ,  $\text{Cr}_{53}^{++}$ , and  $\text{Cr}^+$  (m/n: 2, 26.5 and 52, respectively) and Mn is detected as  $\text{Mn}^{++}$  (m/n = 27.5). It should be noted that the  $\text{Mn}_{55}^{++}$  peak lies between the  $\text{Fe}_{54}^{++}$  peak and the much larger  $\text{Fe}_{56}^{++}$  peak. Hence it is difficult to recognize the  $\text{Mn}^{++}$  peak in a mass spectra (see Fig. 33). Therefore, the distribution of Mn requires special attention in the deconvolution process.

#### b. Results

The results of quantitative analyses of C levels in the martensite matrix and austenite films in a number of 0.3 wt% C-specimens in the as-quenched and low temperature tempered conditions are given in Table 2 (note that the results are given in atomic percent: 0.3 wt% C = 1.4 at% C).

In the 2Mn steel in the as-quenched condition, the average C content in the martensite matrix is very low--less than one-fourth of the bulk concentration (i.e., 0.25 at% = 0.06 wt%), and that of retained austenite is more than twice the original concentration of the alloy (i.e., 2.80 at% = 0.6 wt%). One very significant observation is that the C level at the  $\alpha'/\gamma$ -interface is more than 10 at% (>2 wt%). Tempering the specimens at 200°C for 1 hour reduced the average C

Table 2

The Analysis of C Concentrations in Martensite,  
Retained Austenite and at  $\alpha'/\gamma$ -Interface

Alloy No.	Condition	Phase	At% C	# of Ions Analyzed	
<u>4</u>	As <u>Quenched</u>	$\alpha'$ :	0.23 $\pm$ 0.03	3000	
			0.31 $\pm$ 0.08	3600	
			0.28 $\pm$ 0.13	1800	
			0.14 $\pm$ 0.10	1400	
			0.07 $\pm$ 0.06	1400	
			(near a carbide)		
			0.29 $\pm$ 0.20	700	
			0.14 $\pm$ 0.13	700	
			<u>0.20 <math>\pm</math> 0.19</u>	<u>500</u>	
		Average:	0.23 $\pm$ 0.04	13100	
		Ret- $\gamma$ :	2.83 $\pm$ 0.68	600	
		$\alpha'/\gamma$ -interface :	11, 18, 13		
		$\alpha'$ : (ave.)	0.19 $\pm$ 0.06	6300	
		Ret- $\gamma$ :	0.83 $\pm$ 0.6	600	
		<u>200°C Tempered</u>	$\alpha'$ :	0.17 $\pm$ 0.05	
	Ret- $\gamma$ :		2.24 $\pm$ 0.24		
	$\alpha'/\gamma$ -interface:		6 - 12		
		$\alpha'$ :	0.06 $\pm$ 0.25	1612	
			0.17 $\pm$ 0.05	7495	
			0.07 $\pm$ 0.04	4200	
			0.16 $\pm$ 0.05	7000	
		Ret- $\gamma$ :	2.24 $\pm$ 0.25	3435	
			2.25 $\pm$ 0.37	1600	
			2.25 $\pm$ 0.39	1500	
			2.64 $\pm$ 0.48	1100	
	<u>As Quenched</u>	$\alpha'$ :	0.13 $\pm$ 0.07	2400	
			0.25 $\pm$ 0.09	2800	
			0.20 $\pm$ 0.12	3500	
			0.40 $\pm$ 0.20	1000	
			<u>0.22 <math>\pm</math> 0.16</u>	<u>900</u>	
	Average:	0.23 $\pm$ 0.05	8200		
	Ret- $\gamma$ :	3.40 $\pm$ 0.80			
	$\alpha'/\gamma$ -interface:	5, 9, 9, 20			

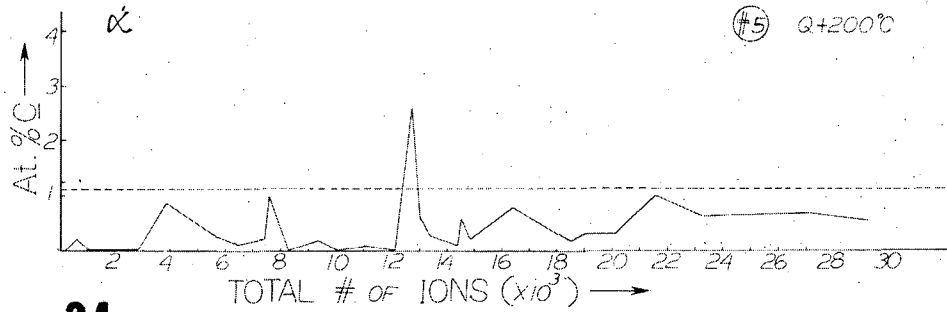
concentration in martensite considerably, while in the retained austenite it stayed nearly the same or decreased insignificantly. There appears to be little or no change in the C content at the  $\alpha'/\gamma$ -interface. The depletion of C in solution in martensite may be due to C segregation to dislocations and the formation of cementite. It should be noted that the C concentration at the  $\alpha'/\gamma$ -interface is higher in some regions, e.g., around ledges or dislocations, giving rise to corresponding high peaks in the C profile across the interface. On the other hand, during tempering, diffusion to the interface region during tempering, occurs and the level of the C content at the interface becomes uniform due to the high mobility of C at these sites. Also given in Table 2 is the analysis of C in 2Ni alloy in the A.Q. condition. As can be discerned in this table, there is again a significant enrichment of C in retained austenite (average 3.40 at%) and depletion of C in the martensite matrix ( $\sim 0.25$  at%). A high degree of C build-up at the  $\alpha'/\gamma$ -interface is again obvious ( $\sim 10$  at%).

The C distribution in the martensite matrix is also not uniform. Atom Probe analysis showed that this is true in samples analyzed both in A.Q. and 200°C tempered conditions. An analysis of the martensite is shown in Fig. 34. Peaks in the C profile were frequently observed during sequential analyses from several Å's thick C-rich regions (sizes of these areas can be found by back calculation from the number

of ions analyzed). These regions are not identifiable in FIM images because they are diffuse and do not stand out from the matrix. However, some peaks with much higher C levels (2.5 at%) were also observed in the specimens again in the A.Q. and especially in the 200° tempered conditions. These regions contain fine carbides which can be discerned in the corresponding FIM images because of their size and dark contrast. Earlier investigation by TEM reported that in the WBDF image of the dislocations in martensite, small irregularly dispersed regions attached to the dislocations. These may be C clusters formed at the dislocations.  $\epsilon$ -carbides in both of the alloys (2Mn and 2Ni) were also observed in the A.Q. condition (Fig. 2). These carbides later transform to much larger cementite upon 200°C tempering; however,  $\epsilon$ -carbides were still observed in foils containing 2 wt% Ni, even at this condition. Therefore, this is a good correlation between the FIM-AP results observed here and the earlier TEM observations of the martensite matrix. (45,121)

More detailed observation on the C distribution through the microstructure was made possible by sequential analysis through both martensite and retained austenite regions. Figs 34 and 35 show C profiles revealing segregation at the  $\alpha'/\gamma$ -interface.

The cumulative total number of ions caught, which is plotted as the abscissa of the graphs, may be taken as a measure of distance evaporated through the specimen. For



34

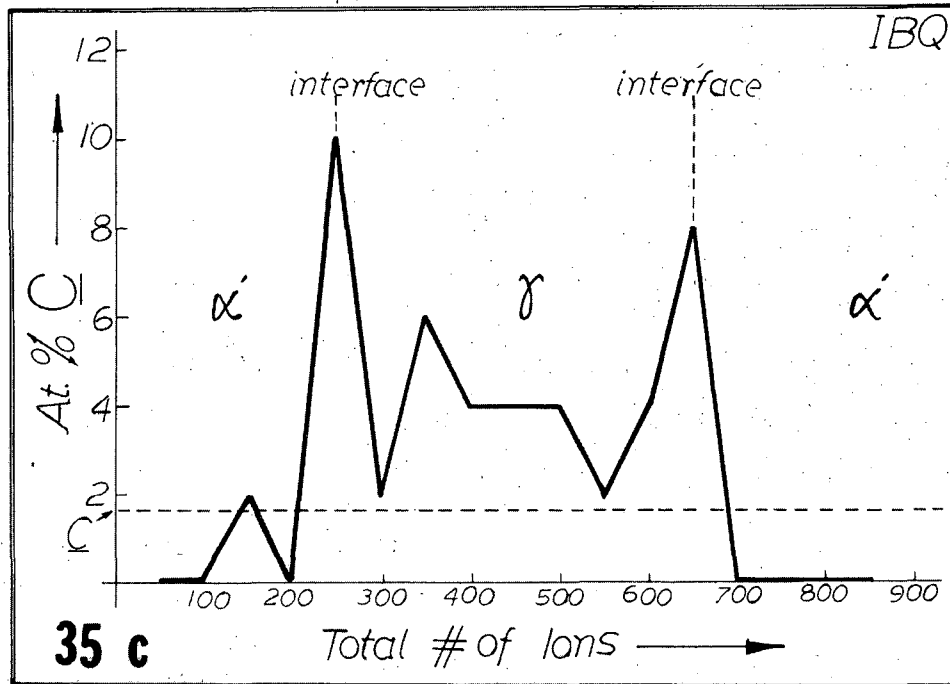
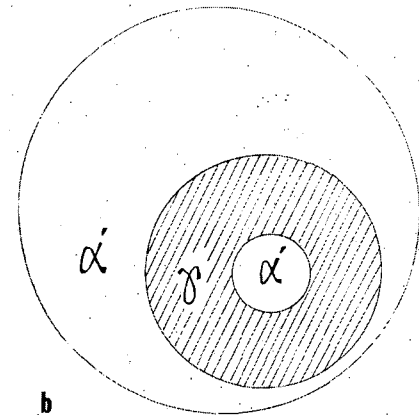
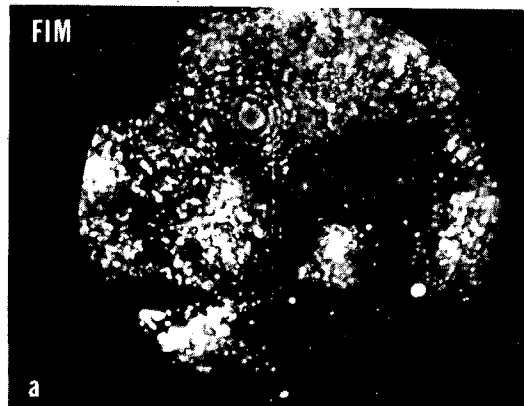


Fig. 34. C profile across the martensite matrix. Note the peaks which may correspond to C clusters at the defects in the matrix (AP sequential analysis--200°C tempered (Alloy 4)).

Fig. 35. (a) FIM image and (b) schematic illustration of the tip. Retained austenite is revealed as a dark circular band. (c) C concentration profile across  $\alpha'$  and  $\gamma$ . XBB 821-1

example, for martensite with tip orientation  $\langle 111 \rangle_b$  and a 20 Å-dia. probe hole, 100 ions caught would correspond roughly to an 8 Å-deep layer of material from the tip of the specimen. Considering the change in the orientation of the tip (and also the crystal structure), and the tip radius of curvature, this figure may be changed to 5 to 8 Å's.

Even with very high cooling rates ( $>10^3$  °C/sec), there still appears to be considerable partitioning of C in retained austenite (Fig. 34). The sample used in the analysis was 0.5mm diameter wire of composition 3 wt% Ni-0.1 wt% Cr-0.35 wt% C (1.63 at%). An FIM image which is taken during the evaporation sequence and its schematic drawing are also shown in Fig. 35-a and b depicting the favorable configuration of the retained austenite film with respect to the specimen axis. It should be noted that the C level in retained austenite is not uniform and showed an average concentration of 4 at%. Whereas the average concentration in martensite appears to be much less than the bulk value, unexpectedly high concentrations of C at the  $\alpha'/\gamma$ -interface (8-10%) were observed even for severe quenching conditions. It should be noted here that the peak at the interface is not sharp, but rather broad as it depends on the configuration of retained austenite film which may distort the true shape of the C profile. (This important point will be iterated later in this section.) A number of profiles obtained by sequential analysis in both 2Mn and 2Ni alloys under these conditions

produced similarly-shaped C profiles. On the average, more than 10 at% C has been observed at the interface (see Table 2).

Tempering the alloys at 200°C for one hour did not change the shape of the C profile appreciably. The C level in  $\gamma$  has retained above 2 at% in this unusually thick (500 Å) film (Fig. 36). However, a decrease in the matrix C content is apparent as was also discussed before. This is probably due to C distribution into clusters at the dislocations and carbides in the martensite. A small increase in the C content at the  $\alpha'/\gamma$ -interface is also expected due to the high mobility of C. In fact, in some cases localized C content at the interface rises above 20 at% which might be the indication that carbides are just starting to nucleate at these sites. Analyses of substitutional alloying elements (Cr, Mn, Ni, Si, Mo) revealed no apparent change in the level of the alloying elements neither in the A.Q. nor in the 200°C tempered condition. Fig. 36 shows Cr and Mn profiles in 2Mn steel in the 200°C tempered condition. Except for insignificant localized variations, there is no deviation in the average value of the Cr and Mn from the bulk concentration. It is relevant to note here that attempts to determine the concentration of alloying elements in martensite and retained austenite by X-ray microanalysis (EDX) in the STEM was not successful.



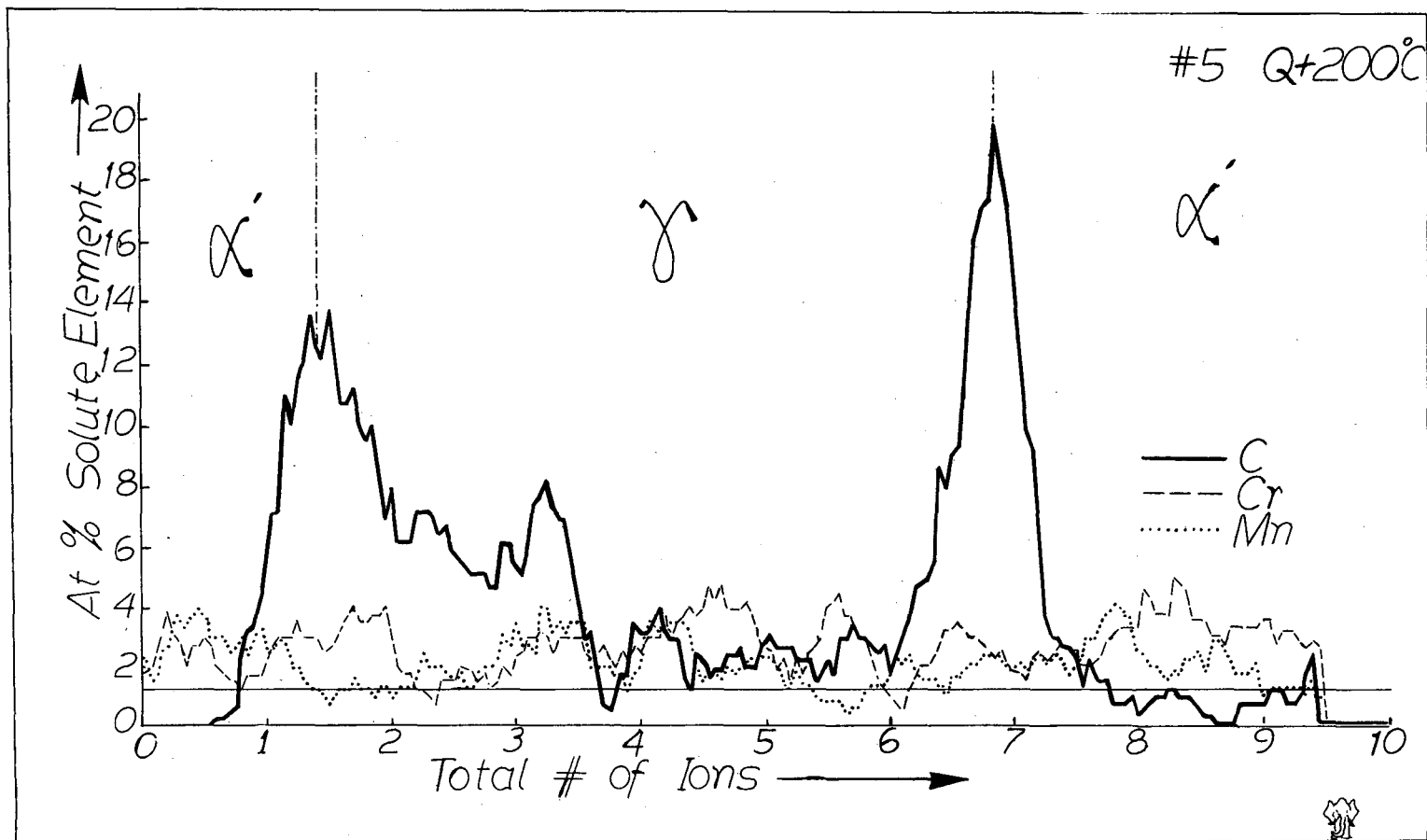


Fig. 36. Substitutional (Cr, Mn) and interstitial (C) alloying element partitioning in martensite and austenite in Alloy 4. Although no change in the composition of Cr and Mn levels occurs in the microstructure, the C-level is high (>2 at%) in this thick retained austenite film ( $\sim 400 \text{ \AA}$ ) and rises to near saturation values at the interface (sequential analysis--200°C tempered condition).

XBL 8112-12975

Some retained austenite films observed in the FIM were very thin ( $<50 \text{ \AA}$ ) and in these cases the C content appeared to be more uniform. In the example shown in Fig. 37, where the AP analysis was done by selected area, there were no peaks at the  $\alpha'/\gamma$ -interfaces, but a single peak corresponding to the film itself. It should be noted here that retained austenite films (or bands) are distinguished from any other feature in the martensite matrix (e.g., especially carbides) by their continuous dark-band appearance in conjunction with the chemical data. There is no way of distinguishing retained austenite from the crystallography of the band, since it is usually not wide enough to recognize any crystallographic poles. However, it is easily recognizable in a favorable configuration as shown in Figs. 35, 38, and 39 which will be discussed in the next paragraph. The FIM image, Fig. 37-a, shows an upside down Y shaped retained austenite film situated between martensite laths. This configuration is frequently observed in TEM micrographs. Fig. 37-c is the optical microscopy image of the tip which shows the general appearance of the tip at low magnifications. FIM image, a, is schematically drawn in b where the circles represent the probe hole on the regions selected for the analysis. The numbers inside the circles are the average C contents (in at%) at these sites. The sequence of the stripping process is schematically shown in (d) where each number in blocks corresponds to the ones in the circles in

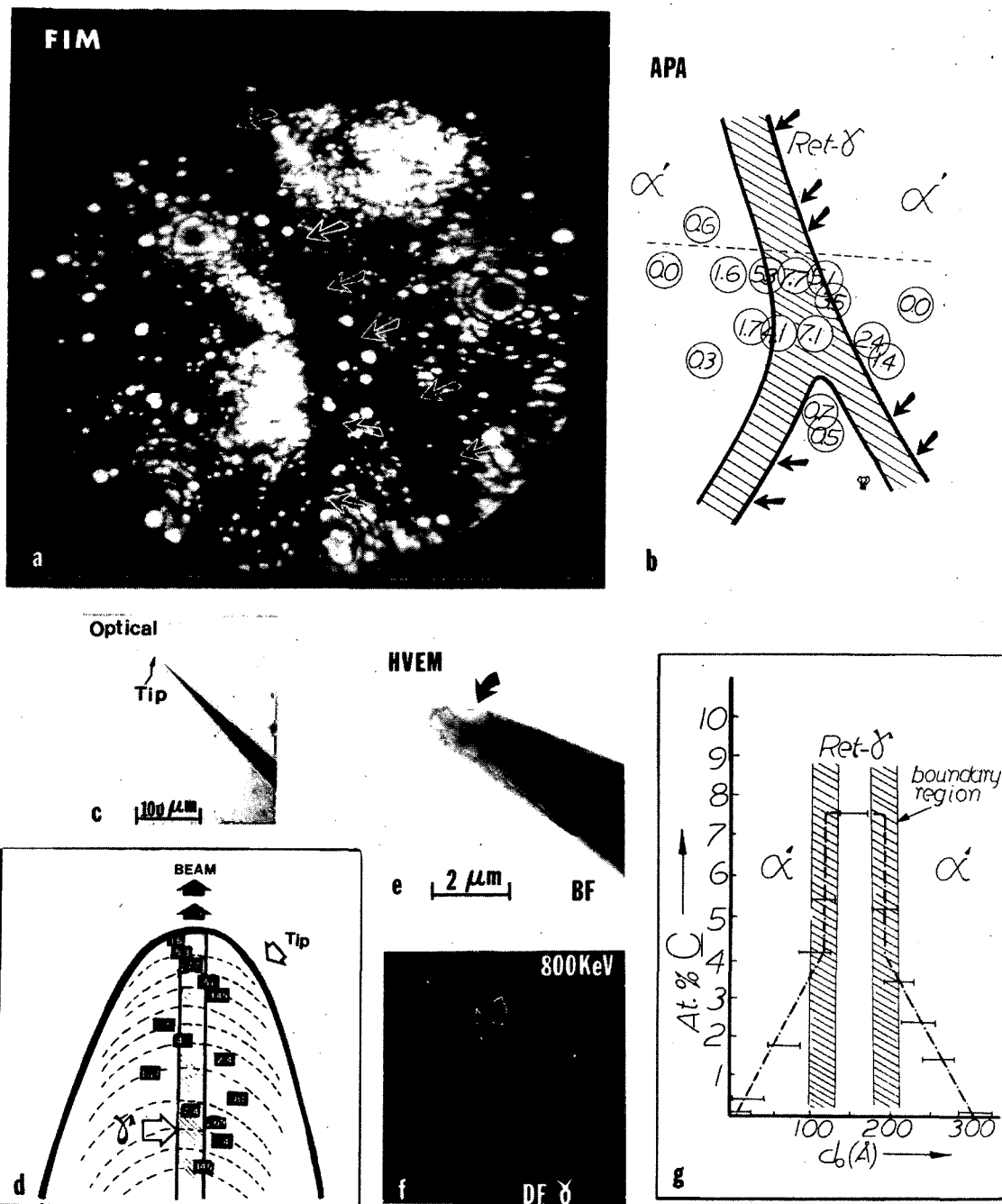


Fig. 37. (a) FIM image of the tip showing very thin retained austenite ( $\sim 50 \text{ \AA}$ ). (b) Schematic illustration of the image in (a); circular regions correspond to the probe hole and the numbers indicate at% C found at those regions. (c) Optical micrograph of the tip. (d) The data change during the evaporation sequence (the boxes correspond to area analyzed). (e) and (f) are TEM-BF and DF images of the tip. (g) Selected area analysis across the film (line AA' in (b)) (AQ-Alloy 4).

XBB 810-11492

(b). The C profile drawn far across the retained austenite film is shown in (g) where there appears to be a single peak. It should be noted that the probe hole used in this particular example is  $\sim 30 \text{ \AA}$  dia. Hence the single peak may be a result of the size of the effective aperture and the configuration of the retained austenite film with respect to the tip as well as the extremely thin width of the retained austenite film which is revealed by HVEM micrographs (e) and (f) where  $\gamma$  appears as a bright band (in DF) in this side (micrographs taken at 800kV). Nonetheless, there appears to be about 7 at% C at the retained austenite region.

It should be emphasized again that the shape of the C profile largely depends on the configuration of the retained austenite film with respect to the specimen tip. There are three possible such configurations:

- (i) retained austenite film perpendicular to the specimen axis;
- (ii) retained austenite film in oblique orientation;
- (iii) retained austenite film parallel to the specimen axis.

These configurations and their corresponding FIM images can be shown as in Fig. 38. The most favorable condition is certainly condition I as the probe hole is simply placed on the specimen tip and a sequential analysis carried out to strip atoms away from the tip layer by layer. Since there is no compositional variation within the area covered by the

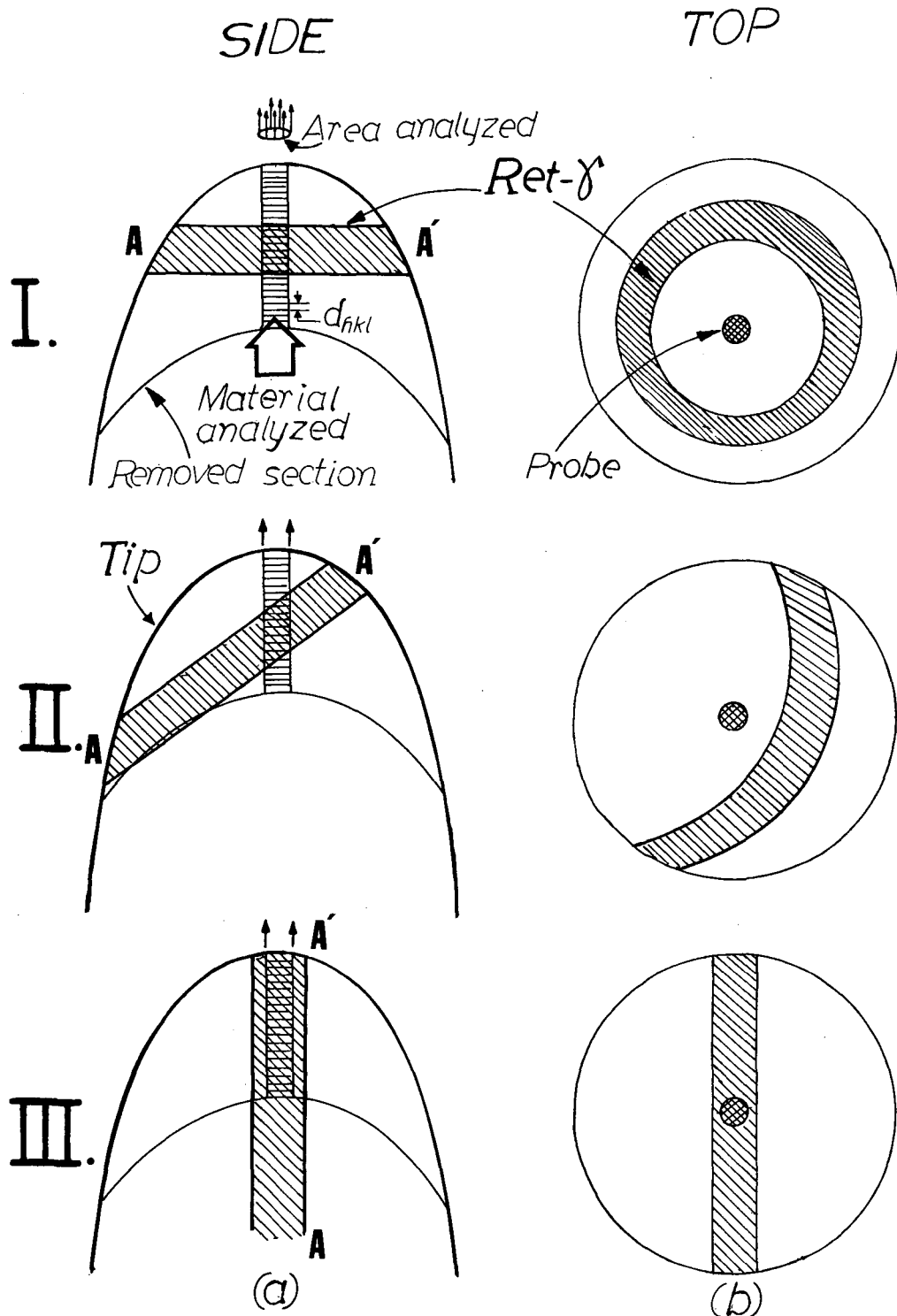


Fig. 38. Possible configuration of retained austenite film with respect to the tip. (a) Sideview (e.g., TEM image); (b) Projected image (e.g., FIM image). Case-I Sequential analysis; Case-II Selected area analysis. In the oblique orientation in Case-III sequential analysis is preferred (refer to Fig. 40).

XBL 8112-12738

effective aperture on the specimen plane, the spatial resolution of the analysis is basically the distance between the atomic layers (i.e.,  $|d_{hkl}|$  of austenite, or martensite) (depth resolution). This configuration gives an analysis close to the actual value and is essential for analysis of interfaces where the variations in the chemistry do not extend beyond several atomic planes. This configuration was always favored during the analysis in the current investigation, e.g., the analysis in Fig. 37. The FIM image 37-a is nearly in favorable orientation. Under these circumstances, the analysis of the phases ( $\alpha'$  and  $\gamma$ ) and  $\alpha'/\gamma$  interface are not subject to interference from each other as the probe hole always lies entirely over one of the phases or interface and does not pick up data from the adjacent regions.

A prolonged search for suitable regions required that the specimen tips be evaporated for long times (which frequently ended up blunting or flashing the tips) or many specimens exchanged for a favorable retained austenite configuration--an extremely time-consuming process. Nonetheless, such configurations were achieved after long trials. Another example is shown in Fig. 39-a where the plane of the retained austenite film is nearly but not exactly perpendicular to the tip axis. This configuration caused the retained austenite film to sweep obliquely across as the field evaporation continued (Fig. 39-b) (compare Fig. 39-a and b with Figs. 38, I, II, and III).

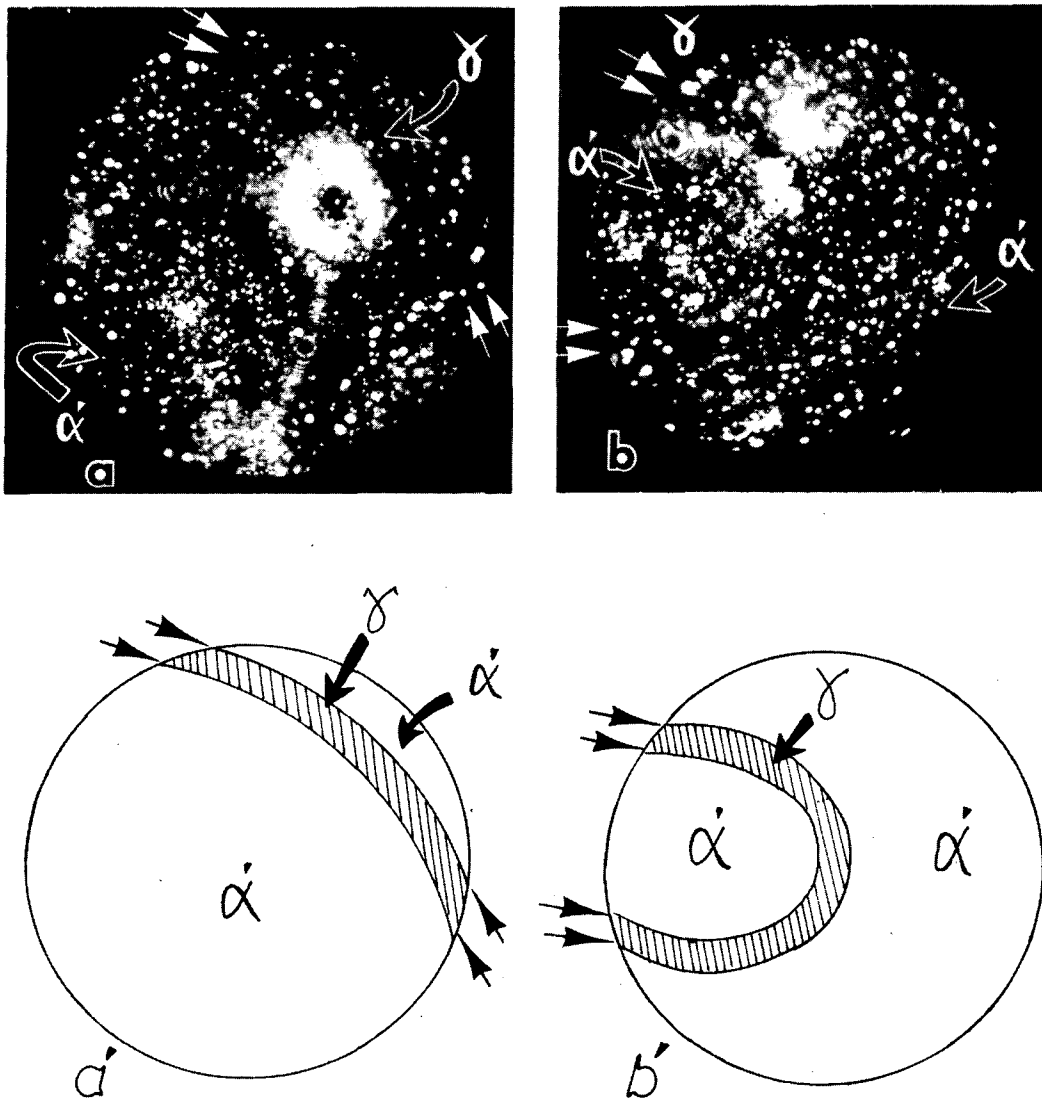


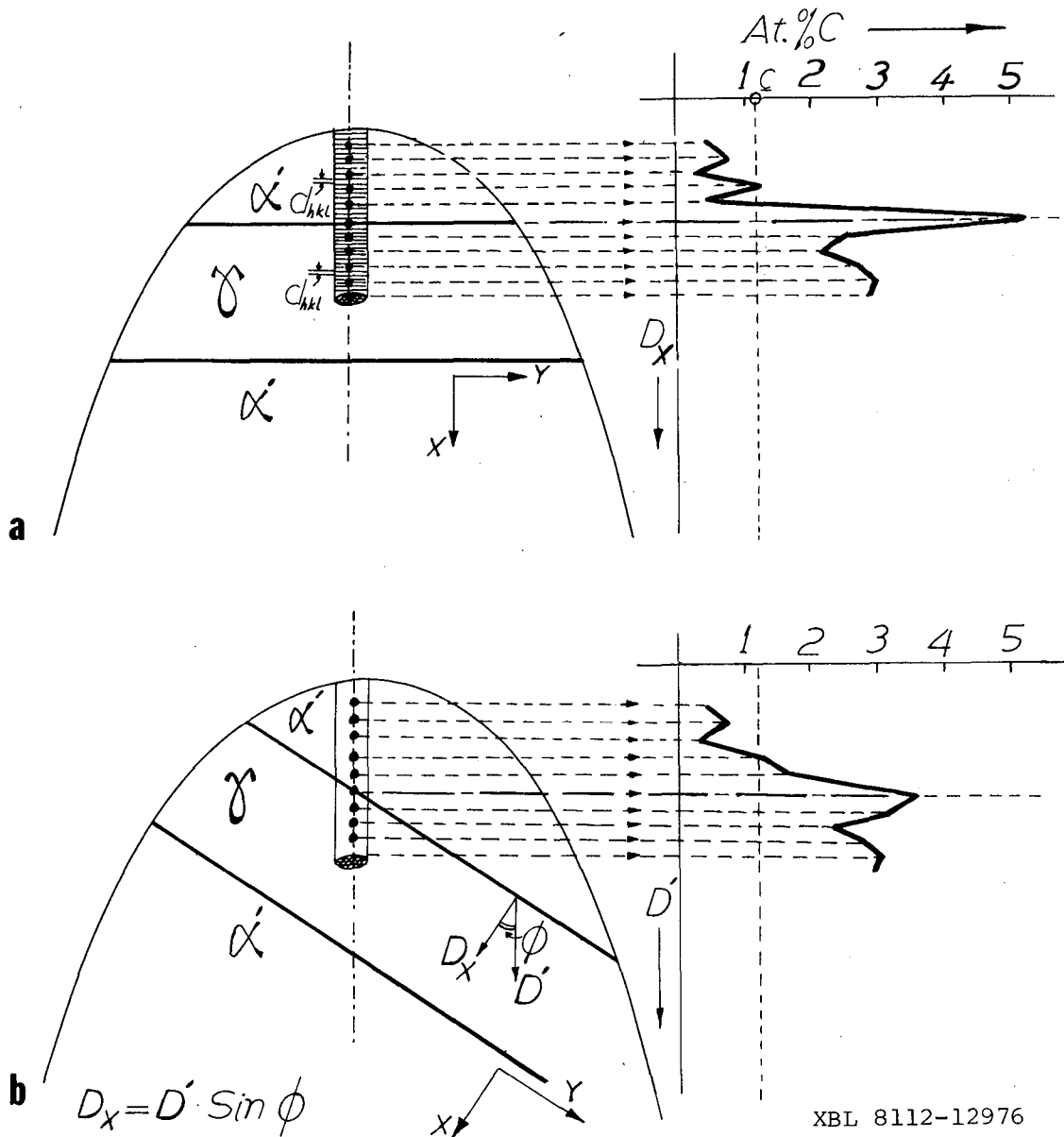
Fig. 39. FIM micrographs show the oblique configuration of retained austenite in martensite matrix. Note the regular change in the images from (a) to (b) which corresponds to the above geometry revealed during the evaporation sequence in A sequential analysis (refer to Fig. 38-IIa).

XBB 810-11424

The second configuration (Fig. 38-II) is the most commonly encountered case where the retained austenite film is obliquely oriented at the specimen tip. During the analysis of the interface the phases on both sides of the interface (i.e.,  $\alpha'$  and  $\gamma$ ) as well as the  $\alpha'/\gamma$ -interface region itself contribute to the analysis in the atom probe, because the effective aperture covers both the matrix and the interface. This results in a lower apparent concentration than actual and causes the broadening of the peak in the concentration profile at the interface region in a sequential analysis (Fig. 40). Note also that, since the interface is approached obliquely, the number of ions caught does not represent the true distance from the interface.

The third configuration is the most favorable for selected area analysis (e.g., as in Fig. 37) as the specimen is moved in the plane perpendicular to the tip axis and different regions on the surface chosen for analysis (i.e., interface, martensite or austenite region). However, this causes problems in the determination of the concentration at the interface. Because of the finite dimension of the probe hole (20-30 Å dia. effective aperture) and of the nature of the ion counting statistics, the spatial resolution (lateral spatial resolution) deteriorates. Therefore, the actual spatial resolution is determined mainly by the size of the effective aperture and the topography of the tip at the interface region. In this case, one has to take an average





XBL 8112-12976

Fig. 40. Schematic illustrations of the change in the tip geometry and the corresponding concentration profiles (e.g., for C). (a) Retained austenite is perpendicular to the long axis of the tip. This is the most desirable configuration and the concentration profile represents the true concentration change with distance  $D_x$  taken perpendicular to the  $\alpha'/\gamma$  interface. (b) Retained austenite is in oblique orientation with respect to the long axis of the tip. The concentration at and near the  $\alpha'/\gamma$  boundary is not the true value, but an average value which depends on the angle  $\phi$ . Hence the distance  $D'$  is not the true distance but a projection of  $D_x$ .

of the ions counted within the region covered by the periphery of the aperture, achieving only an average value within, say,  $20 \text{ \AA}$  area. Therefore, the measured concentration of the planes of the interface becomes much lower than the actual value lowering the peak height and gives rise to a broader peak. In the extreme case shown in Fig. 37, and especially if the retained austenite film is very thin ( $40\text{-}50 \text{ \AA}$ --little thicker than the aperture), the details in the profile, i.e., the peak at the interface would disappear and only one peak, corresponding to the average C content of the interface and retained austenite film, may appear. In this particular example, C atoms may have been uniformly distributed within both the interface regions and the retained austenite because of its thinness.

#### 4.4. DISCUSSIONS - MECHANISMS OF AUSTENITE STABILIZATION

Retained austenite in steels is normally associated with the plate martensitic structures<sup>(15,33,107)</sup> that form in high carbon steels. In such steels the microstructure consists of "lenticular" martensite crystals which criss-cross the prior austenite grains along the fixed crystallographic orientations with austenite remaining in "blocks" between the plates. Numerous factors are known to contribute to the presence of retained austenite in these structures which can amount to 5 to 20% by volume.<sup>(33)</sup>

For example, it has been established that<sup>(116,147,152)</sup> compressive stress will decrease the  $M_s$  temperature

(especially hydrostatic pressure) whereas a tensile stress will increase it. Plastic deformation of a few percent usually rises the martensite transformation start temperature  $M_d$  (107,147,152) ("strain induced" transformation) but larger amounts of deformation inhibits the transformation, (15,106,108,117,147-149) so that the amount of martensite formed decreases. (15,115,147) The temperature of deformation and the time of holding also affect the amount of retained austenite significantly as both changing the microstructure on the microscopical level (allowing C and N to diffuse into sinks, e.g., dislocations, subboundaries and small coherent precipitates which inhibit the transformation dislocation movement) (15,107,147-149) and allowing long range chemical changes to take place (partitioning of solute elements.) (62,107,119) This is important with respect to the favorable changes in the free energy of the austenite which at this "new state" (at lower temperatures) has different chemical composition than it had at high temperatures. However, this effect is very sluggish bearing the fact that the  $M_s$  temperature in plate martensitic steels are very low. The rate of cooling also affects a shift in the  $M_s$  temperature; (110) the higher the cooling rate the higher the  $M_s$  will be. The extent of this change depends on the alloy composition and previous austenitizing temperature (and time). Size effect is also significant as it has been observed that while almost complete transformation occurs in

bulk samples, only partial transformation occurs (with much austenite retained) in small spherical particles (e.g., 500 Å dia.)<sup>(150-151)</sup> of the same bulk composition. No transformations occur at all in smaller particles and they remain as austenite.<sup>(150)</sup>

As discussed at length in the preceding sections of this thesis, in the case of lath martensites the shape, size, distribution, amount, and chemical constituents of the "thin film" retained austenite are different from that in plate martensitic structures. The mechanisms responsible for the existence of retained austenite in lath martensites will be discussed in the light of the experimental evidences in the following sections.

#### 4.4.1. Chemical Stabilization:

The initiation and progress of the  $\gamma$  to  $\alpha'$  transformation are both controlled by the chemical and nonchemical energies of the system.<sup>(62,111)</sup> The chemical free energy depends largely on the chemical species of the phases. If any variation in the chemistry of the phases occurs through diffusion during cooling then the course of the transformation is altered. Thus partitioning of alloying elements (substitutionals such as Cr, Ni, Mn, or interstitials such as C and N) between the phases during the transformation will increase the driving force required to continue the transformation. This decreases the  $M_f$  temperature to lower values and hence the austenite may be retained as a

metastable phase. This phenomenon is called "chemical stabilization." (10)

It has been found in this study that although there is no noticeable change in the substitutional alloy content of either austenite or martensite, an appreciable increase in the C content of the austenite and a decrease in the martensite were recorded (Figs. 34, 35 and 36). From the metastable extension of the equilibrium diagram shown in Fig. 46 it can be seen that the austenite can accommodate nearly 4 wt% carbon at room temperature. In the current study, the analyses performed by AP and CBED techniques have revealed that the carbon content of the retained austenite is more than twice the nominal content in the bulk samples. Most of the AP data indicates that the C in  $\gamma$  is around 2.5 at% which would result in a decrease in  $M_s$  temperature of about 150°C (Fig. 41). It should also be noted that the  $M_f$  temperature corresponding to the above C level in austenite is even lower.

The amount of carbon enrichment in the retained austenite is determined by the extent of carbon redistribution by diffusion during quenching. Many critical variables affect this, such as the cooling rate of the sample (Appendix 5) the diffusion coefficient of carbon in  $\alpha'$  and  $\gamma$  (Appendix 4), the  $M_s$  (and  $M_f$ ) temperature of the bulk alloy, and the growth rate (especially sidewise growth) of martensite laths (Appendix 3).

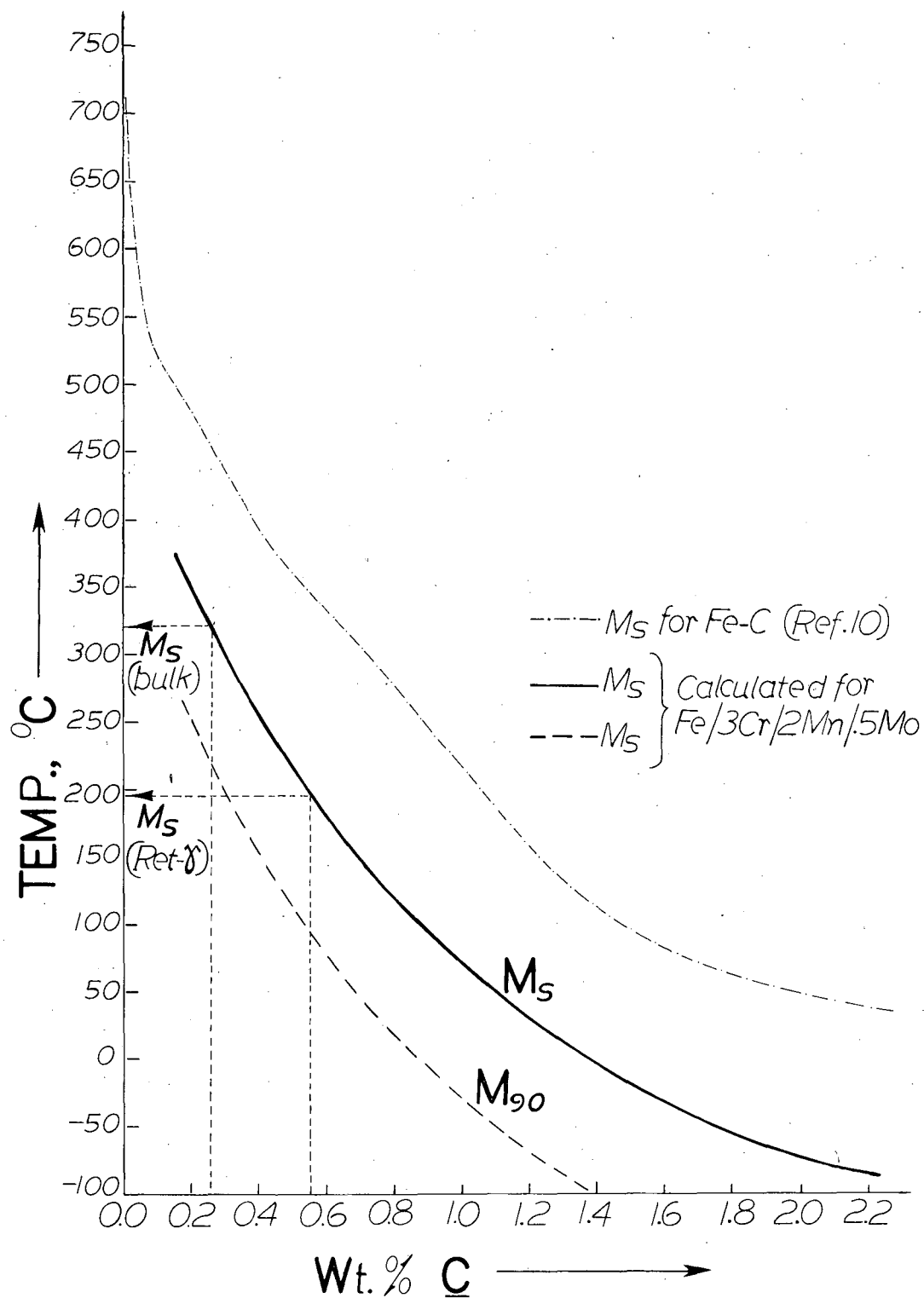


Fig. 41. The  $M_S$  and  $M_f$  vs. C content in steels. (Note Ref. 10 is now Ref. 33 in the text.) Note that  $M_f$  of retained austenite drops to much lower temperatures when C increases.

The cooling rate depends on the quenching medium and size and shape of the sample. Cooling curves determined for thin plate samples are plotted in Fig. 41-a for oil quenching. (It should be noted that the samples used for the spectroscopic analysis were much smaller in size.)

As presented in Appendix 5 analyses were made on determination of the effective diffusion distance for different shaped samples cooled in the different mediums used in this investigation. Table I in Appendix 5 shows that, even for fast cooling rates, it is possible to achieve the experimentally found average concentration in  $\gamma$ .

The critical time available for the carbon redistribution during cooling depends largely on the diffusivity of carbon in  $\alpha'$  and  $\gamma$ . Calculation of diffusion coefficients of carbon in both phases, i.e.,  $D_C^{\alpha'}$  and  $D_C^{\gamma}$  is discussed in Appendix 4. An average value for the diffusion coefficient of carbon in ferrite ( $D_C^{\alpha}$ ) has been calculated from the data in the literature<sup>(160-168)</sup> and equated to  $D_C^{\alpha'}$ . The diffusion coefficient in C and  $\gamma$  at low temperature is the extrapolation of the average value found from high temperature data.<sup>(166-168)</sup> The most representative values are as follows (activation energy is given in cal/mole):

$$D_C^{\alpha'} = 0.0173 \exp\left(-\frac{20180}{RT}\right) \quad (1)$$

$$D_C^{\gamma} = 0.010 \exp\left(-\frac{30880}{RT}\right) \quad (2)$$

These values are used to calculate the effective diffusion distances, <sup>(173)</sup> i.e.,  $d_{\text{eff}} \equiv 2(Dt)_{\text{eff}}^{\frac{1}{2}}$ , which can be travelled by a carbon atom in martensite during cooling ( $d_{\text{eff}}$  values are tabulated in Table I in Appendix 3). In order for this redistribution to affect austenite stabilization, carbon atoms must be able to move to the  $\alpha'/\gamma$  interface and on into the  $\gamma$ .

There is no quantitative analysis made on the determination of the growth rate of lath martensite in a system similar to the present case. Some investigators <sup>(156-159)</sup> worked with the bainite transformation where the bainitic ferrite crystals are similar in shape and size to lath martensite crystals. Two separate growth rates were determined; lengthwise and wide-wide growths. Growth in the long direction of the crystals is very rapid ( $10^4$  Å/sec) while thickening of the crystals is slow (average rate is  $10^3$  Å/sec) and occurs at a decelerating rate. Lath martensites grow lengthwise very fast and sidewise slowly <sup>(157,158)</sup> (as revealed in Ref. 33) although no quantitative determination was made on the growth rates. As the lath slowly thickens considerable carbon redistribution can take place. In fact, an analysis has been made on the estimation of the growth rate of laths from the known experimental data (Appendix 3). The value found gives a sidewise growth rate of about  $dz = 10^4 - 10^5$  Å/sec. From this, an estimation was made on the available time for carbon to redistribute itself



in the martensite, i.e., the effective diffusion distances in the  $M_s$ - $M_f$  range, as given in Appendix 5.

It is seen from the foregoing discussion that during the decelerating growth of the laths during cooling in the  $M_s$ - $M_f$  range, carbon atoms redistribute themselves in  $\alpha'$  and migrate towards  $\gamma$  where they are soluble. However,  $D_c^\gamma$  at this temperature range is not high enough for carbon to diffuse in  $\gamma$  through the whole film thickness. Except where the retained austenite thickness is very small (e.g., 40-50 Å) then the concentration across the interface is, on the average, at the same level (refer, e.g., to Fig. 37). However, in the most commonly observed cases where the retained austenite is wider (>100 Å) carbon diffusing from  $\alpha'$  accumulates at the semicoherent  $\alpha'/\gamma$  interface to very high values (10 at% or higher, e.g., see Figs 35 and 36) which has other consequences in the stabilization process discussed in the next section. Consequently, the overall concentration profile may be represented schematically as shown in Fig. 42 where the C level in martensite gradually decreases (with sharp peaks corresponding to carbon clusters at the dislocations) towards the interface, rising to high concentrations at the  $\alpha'/\gamma$  interface and dropping in  $\gamma$  where the average concentration is still twice (or higher) than that of the nominal concentrations. Although this carbon enrichment will provide some chemical stabilization it cannot fully account for the existence of retained austenite because the  $M_s$  temperature is not low enough (see Fig. 41). There

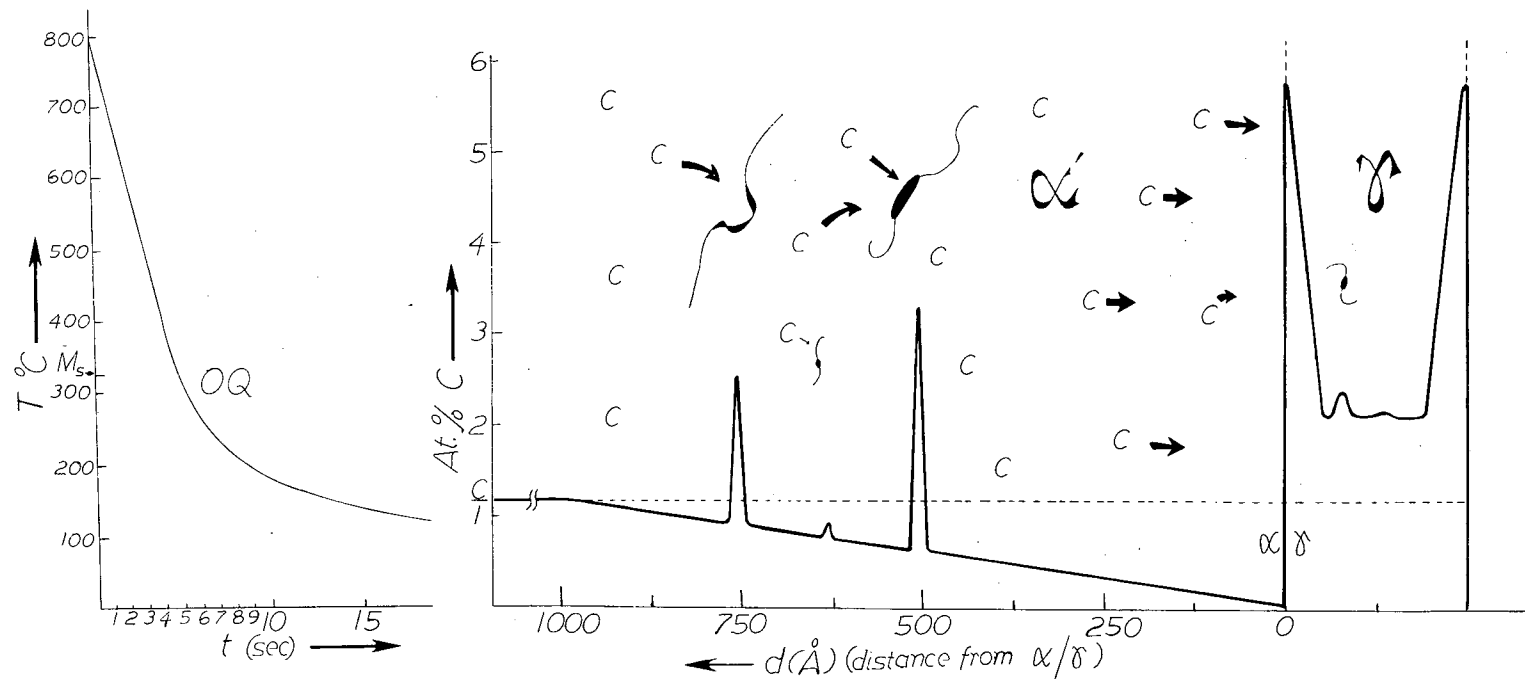


Fig. 42. (a) The cooling curve for oil quenched Alloy 4 samples (1mm dia.). (b) Schematic diagram showing the approximate carbon profile across the martensite austenite microduplex structure in the as quenched sample. Sharp peaks in the profile in martensite are due to carbon clustering at early stage of carbide formation.

XBL 818-10987

are other effects which also contribute to the total stabilization as will be discussed in the next sections.

#### 4.4.2. Thermal Stabilization:

The characteristic shape change of the martensitic transformation implies continuity across the interface which, consequently, must be substantially coherent. (25,177)

However, complete coherency can exist only under the circumstance that the deformation relating any pair of unit cells in the two lattices (fcc and bcc in steels) contains one principal strain which is effectively zero. Since this condition is not met between austenite and martensite phases in steels, the mismatch is corrected by periodic discontinuities (e.g., dislocations) (25,75,175,177) which ensure that strains do not accumulate over large distances. The interface thus contains regions of misfit as a network of dislocations (177) which become mobile under the application of suitable chemical (or mechanical) driving force. (1,2)

However, these interface dislocations can be immobilized (36,105-107,147-149) by interstitial solute atom segregation which form "Cottrell atmospheres" (178) to slow down or even cause complete cessation of martensite crystal growth. Therefore, austenite trapped between two such interfaces is retained as a metastable phase; this phenomenon is called "Thermal stabilization of austenite." (106-109)

In plate martensitic steels the amount of "blocky" austenite retained can be controlled by holding the sample

at a temperature above or below the  $M_s$ . (106-109,179-180)  
The amount of retained austenite increases as the temperature and time of hold is extended. (107) This is mainly attributed to carbon segregation to the dislocations at the interface to form "groupings" which oppose advancement of the interface resulting in thermal stabilization. Similar phenomena may be attributed to the case of lath martensites containing thin film retained austenite. When a lath nucleates, the interface advances quickly lengthwise and moves slowly sidewise by the movement of dislocations (1,175) (and/or ledges) (2,177) as the cooling is continued. The new bcc lattice is strained by the trapped C which diffuses towards the interface and into the  $\gamma$  to the extent that time and temperature permit. The carbon atoms diffusing into the interface segregate at the dislocations present at these sites. Hence there is dislocation-interstitial carbon interaction which produces a net force which opposes the interface movement (see Appendix 6). The stabilization phenomena may be explained in detail as follows.

The interaction of the elastic stress fields around interstitial solute atoms with that of semicoherent interface decreases the elastic strain energy which furnishes a driving force for the segregation of these solute atoms to the interface (108,178) (similar to "strain aging" (178) in steels). At high temperatures and low dislocation velocities (i.e., low velocity of interface propagation as in

isothermal martensite<sup>(36)</sup> or in the present case of lath martensite (see Appendix 3) carbon can diffuse over long distances under the influence of the strain field of the interface. The degree of stabilization is dependent upon the concentration<sup>(108)</sup> of the anchoring atoms at the interface. Thus stabilization is determined by the diffusion rate of carbon at a temperature, which changes, with a decreasing rate, during cooling. The binding of C to the dislocations increases with decreasing temperature<sup>(108,159)</sup> and so the effect of thermal stabilization will also increase with decreasing temperature. During the lath growth, this corresponds to the time towards the end of the transformation near  $M_f$ . Thus, the maximum effect may not be obtained because of decreased  $D_C^{\alpha'}$  at low temperatures consequently limiting the C diffusion.

It has been found in this study that the carbon content at the interface may attain values (5-10 at%, Figs. 35-37), high enough to stop the interface. An approximate analysis in Appendix 6 determined the concentration needed at the interface to prevent its further advancement. It should be noted that the concentration increase mainly occurs during cooling while the temperature is still high enough for carbon diffusion. However, the occurrence of more segregation of carbon at room temperature is unavoidable. This, rather than causing "Thermal-stabilization," further

increases the "stability" of retained austenite at ambient or lower temperatures (even at liquid nitrogen temperature).

#### 4.4.3. Mechanical Stabilization:

Stabilization of austenite by mechanical means has two components: (i) plastic deformation of  $\gamma$  slows the progress of the  $\gamma$  to  $\alpha'$  transformation. (ii) the residual stresses left within the sample affects the transformation.

During transformation to martensite, the parent austenite lattice is highly deformed ahead of the transformation front and contains high density of imperfections such as dislocations, faults, ledges, etc. (refer to Figs. 26 and 43). This situation results from the accommodation of strains created during the shear stress and dilatational (3,4,115-117) stress (volume increase).<sup>(24)</sup> It is more difficult to transform a distorted lattice to another lattice by a shear transformation.<sup>(15)</sup> Hence the progress of the transformation is controlled partly by the resistance offered by the matrix to the growth of the new crystals. (15,108,115,147,148) That is, the growth of individual laths of martensite can be viewed as taking place by the systematic motion of the interface consisting of arrays of dislocations movement of which will be impeded by the presence of obstacles, such as other dislocations in the parent phase.<sup>(15,118,148,159)</sup> When the plastic deformation takes place in  $\gamma$  during the formation of  $\alpha'$ , more dislocations will be generated and continually increasing driving

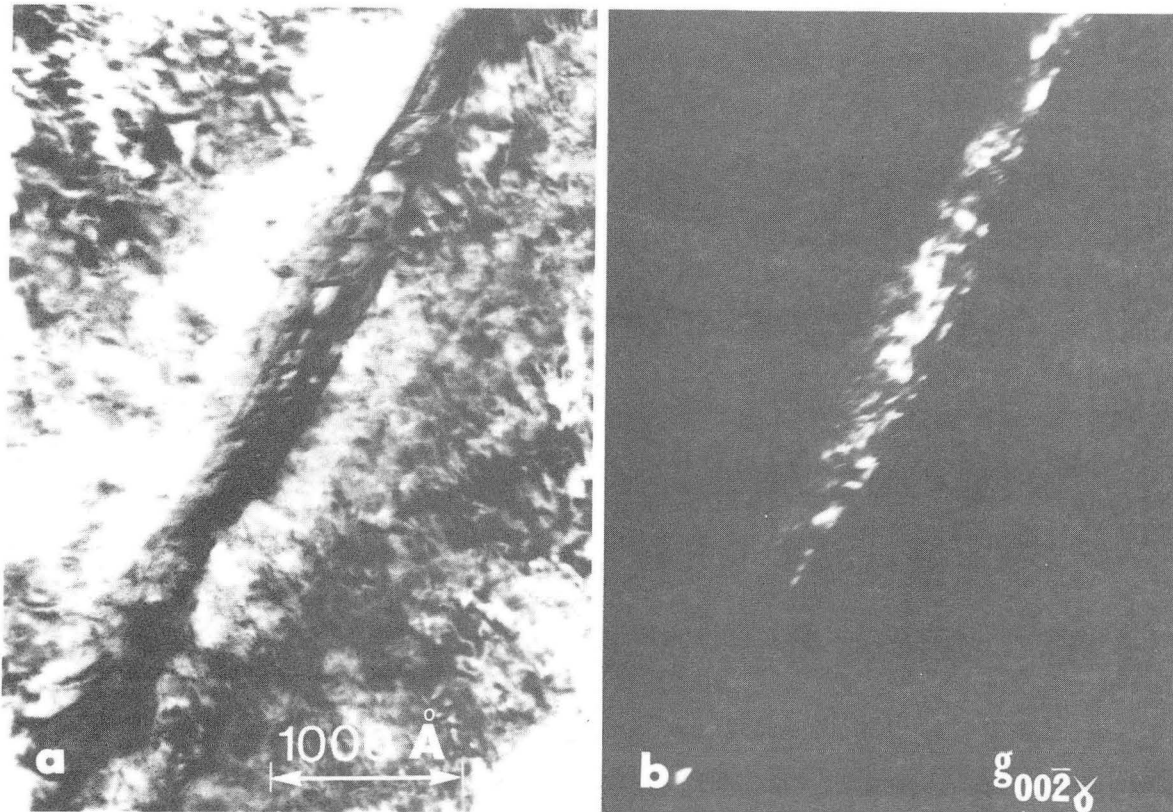


Fig. 43. High magnification BF (a) and DF (b) micrographs shows the contrast due to high dislocation density both in austenite and martensite (Alloy 5). Other defects, such as "ledges" are also apparent across the films.

XBB 817-7030

force must be provided before more martensite could form. Therefore, as the transformation proceeds it becomes progressively more difficult to transform the remaining  $\gamma$  some of which is ultimately retained as a thin metastable film between martensite crystals.

In addition to this direct obstruction to the movement of the coherent interface, there is also an effect of carbon redistribution in this deformed austenite. This happens at higher temperatures within the  $M_s$ - $M_f$  range where interstitial carbon segregates to the dislocations in austenite as revealed by Atom Probe analysis. Similar to deliberately applied "ausforming" process<sup>(185-187)</sup> this effectively increases the strength of austenite which in turn increases the "mechanical stability." Thus, further spontaneous transformation of  $\alpha'$  will be opposed as it must be accompanied with more deformation.

Samples quenched to ambient temperatures from the austenitizing temperature contain a high degree of residual strains.<sup>(186)</sup> In the case of the austenite to martensite transformation, stresses of the order of 50 ksi<sup>(10)</sup> resulting from quenching correspond to about 10% of the stresses created by the volume change during the fcc to bcc transformation. These residual strains which must be accommodated may also effect the local stabilization of austenite.<sup>(115, 116,147)</sup>



#### 4.4.4. Summary:

The overall stabilization of austenite is probably due to some combination of all the stabilization mechanisms discussed above. In terms of mechanical stabilization the internal stresses created by the volume change produce an energy barrier which must be overcome, i.e.,  $M_s$  reduced locally by about 5°C/ksi. This is the most important effect and always occurs irrespective of rate of cooling or changes in the chemical species. The measured residual strain corresponds to only 5-10% of the total expected by the lattice expansion. However, the stress effect should be less important in low carbon alloys because  $\Delta V^{\gamma-\alpha'}$  at  $M_s$  is smaller. The reduced plastic deformation is accommodated more readily and much less  $\gamma$  is preserved than in high carbon-high alloy steels.

Chemical stabilization is more important in low carbon steels because the  $M_s$  is higher and more diffusion can occur during the transformation. Hence C buildup causes the austenite, present as thin films, to persist even during quenching to liquid nitrogen temperatures.

There is also a thermal effect where carbon segregates to  $\alpha'/\gamma$  interfaces during growth pinning the transformation dislocation so that the interface is immobilized. Interface motion is also opposed by the austenite deformation which eventually leads to complete suppression. The remaining very highly deformed austenite is retained in the form of thin films and trapped between the martensite crystals.

#### 4.5. MECHANISMS OF DECOMPOSITION OF RETAINED AUSTENITE

##### 4.5.1. Mechanical Instability (Effect of Deformation and Volume Constraint):

The effects of deliberately induced plastic deformation on the behavior of thin film retained austenite were not included in this research program. However, some interesting structural features were observed (probably induced during the foil preparation) which are related to mechanical instability of the fcc phase.

In some instances, instead of retained austenite, martensite strips were observed at the lath boundaries. An example (from a 0.06C steel) is illustrated in Fig. 44 which shows a large area containing small twinned regions in different orientations between the martensite laths on either side. Analysis of the SAD pattern (44-c) revealed that the twins form on  $\{112\}$  planes of martensite. The DF micrograph, taken using a twin spot, reveals the contrast change corresponding to the twin variants contributing to this particular reflection. Measurements in the regions containing edge-on twins showed that they are only  $30 \text{ \AA}$  in thickness which gives rise to long streaks (or spikes) <sup>(122)</sup> extending from the twin reciprocal lattice points. Note that in the SAD pattern (Fig. 44-c), the zone axis is very near to  $(111)$  bcc. Extra reflections, formed by the intersection of the twin spikes with the Ewald sphere, are arranged such that

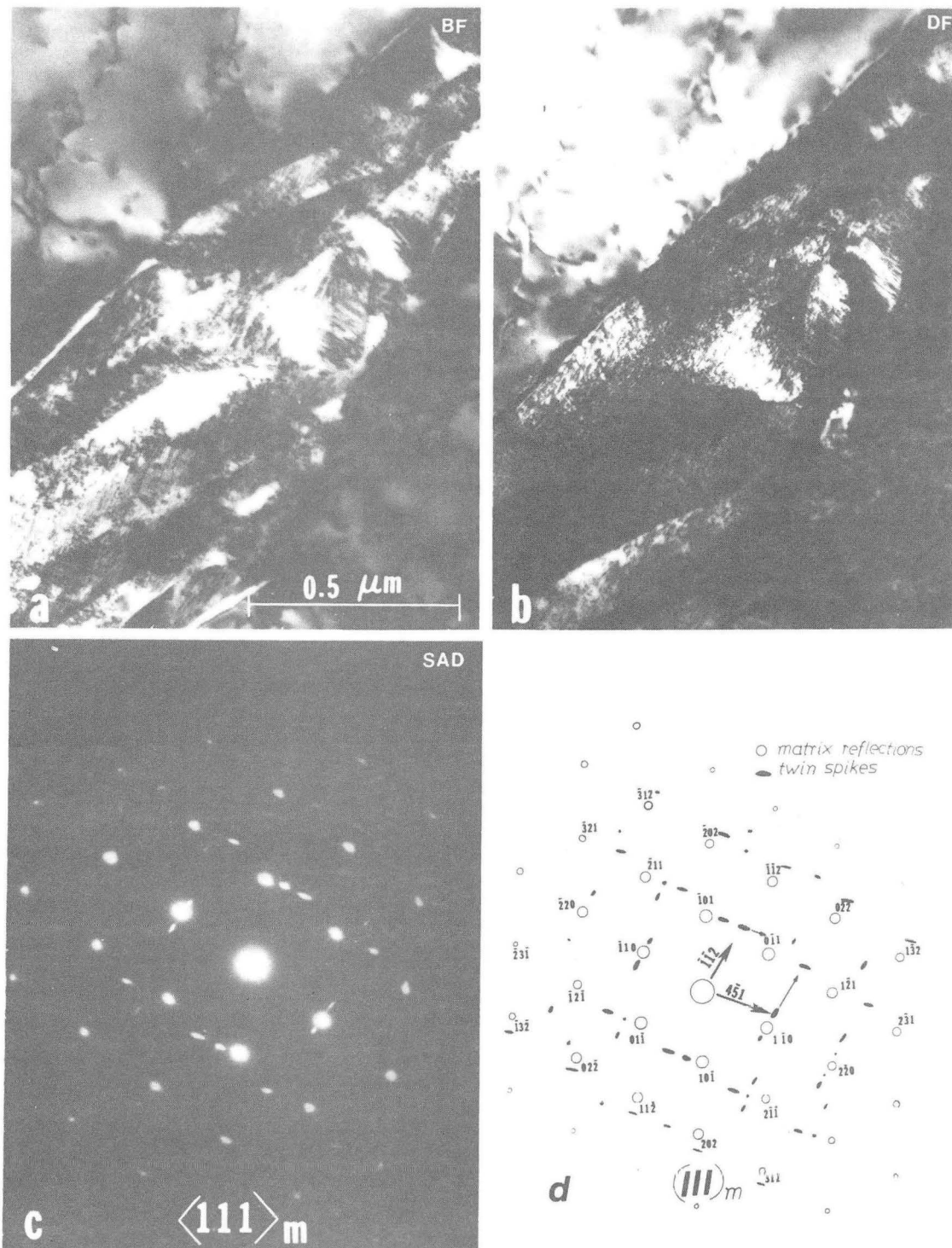


Fig. 44. (a) BF image--a wide region exhibiting twins in the form of a strip between the martensite laths. (b) DF is from the twin reflection near the matrix  $(\bar{1}01)$ . (c)  $(111)_B$  SAD pattern from the area covered by the matrix and the twins. (d) The analysis of the SAD pattern (Alloy 1).

XBB 810-11493

they lie along either  $[112]$  or  $[321]$  reciprocal lattice directions. Hence the twins are on  $(11\bar{2})$  or  $(2\bar{1}1)$  planes.

Similar twins were observed in a sample containing 0.17 wt% C. In the inset in Fig. 45 the dark contrast regions are expected to be retained austenite films extending into the perforation of the foil. Indeed some of these quite thick strips correspond to retained austenite as confirmed by CBED (refer to Section 4.3.2 or Appendix 3). However, others such as the one shown in Fig. 45 are composed of small twinned regions. A high magnification DF micrograph in Fig. 45-b taken by using a twin reflection (Fig. 45-d) reveals the contrast change corresponding to the individual twin crystals. Both the size of the twinned region ( $\sim 1 \mu\text{m}$ ) and the twins ( $50 \text{ \AA}$  width) are larger than those within the bulk of the sample (Fig. 44). The SAD pattern (c) shows two  $(110)_b$  superimposed patterns corresponding to the matrix and the twin, which are formed on  $(112)$  planes of martensite (Fig. 45-d).

Transformation twins are the common features in plate martensitic structures. <sup>(6,17,30,34,187)</sup> According to the phenomenological theory of the martensitic transformation, twinning is essential for lattice invariant shear to produce a lattice invariant plane (habit). <sup>(68,69)</sup>  $\{112\}_M$  twins, having the habit which originates from the  $\{110\}$  planes of austenite, are most often observed although  $\{110\}_M$  twins have also been reported. <sup>(34,188)</sup>

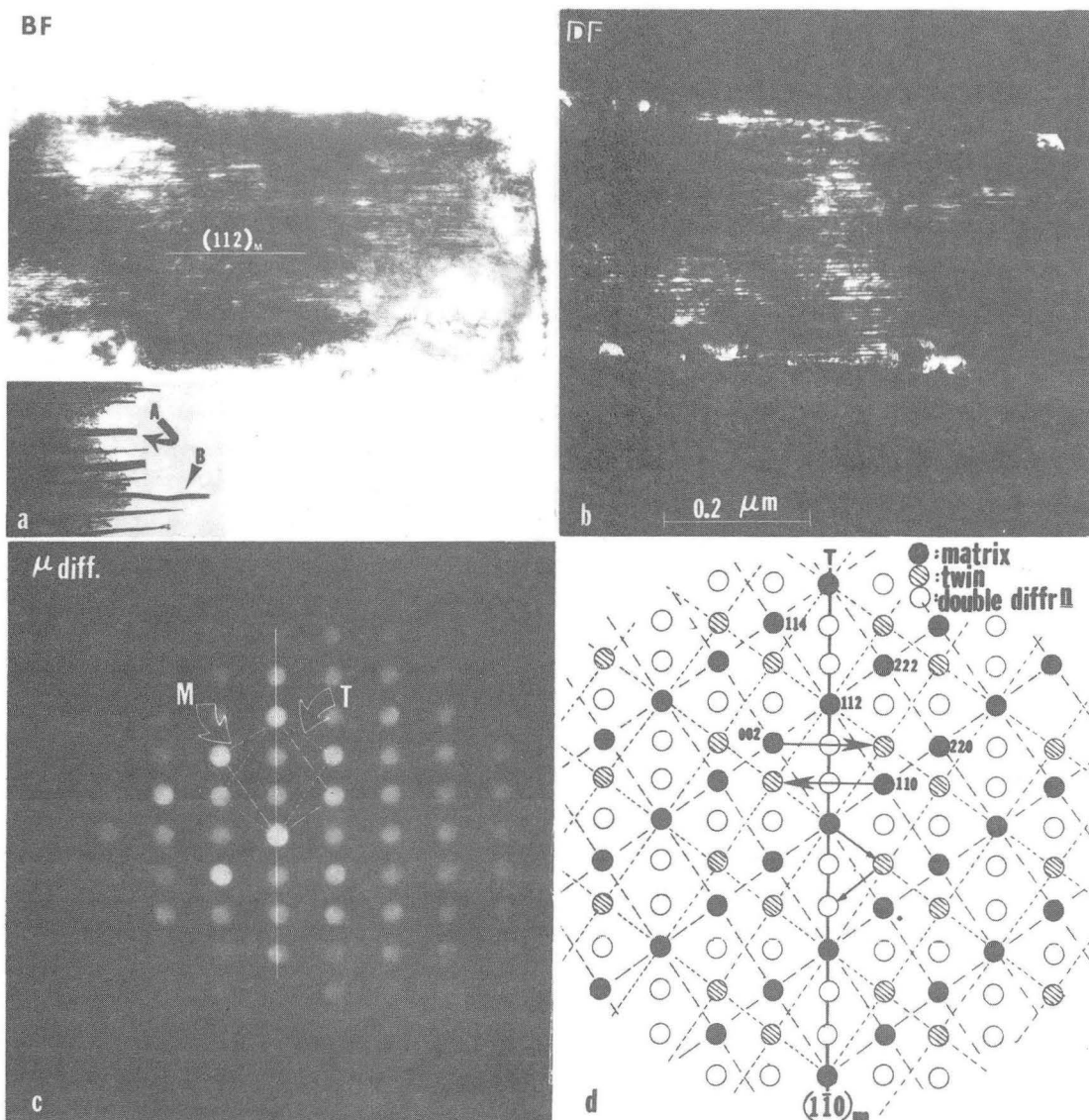


Fig. 45. (a) Twins formed in a pre-austenite strip in 0.17C steel. A low magnification image of the microstructure near the perforation shown in the inset in (a) reveals dark strips freely extending into the hole. Some of these strips (like A) are retained austenite (proven by CBED, discussed in Section 4.3.2.) and some others (like B) are transformed regions exhibiting twinned structure (BF). (b) DF micrograph (from a twin reflection) showing twin contrast which extended along the strip. (c) Microdiffraction pattern showing the arrangements of the reflections from the  $(1\bar{1}0)$  matrix,  $(112)$  twin and double diffraction formed by the dinteraction of the twin and matrix reflections.

XBB 810-10774

Observations, similar to described above, were made by earlier investigators<sup>(189-192)</sup> where small Fe precipitates in a metal matrix (e.g., Cu) were transformed martensitically either by deformation ( $\sim 10\%$ ) or by removal of the volume constraint (e.g., near the foil edge). In the present case, presumably the twinned regions in Figs. 44 and 45 transformed from the original retained austenite because of the local deformation during handling of the foil or through relaxation by the removal of the surrounding martensite matrix during thinning. Since the C content of the austenite is raised to near 1 wt% through partitioning it would only transform plate martensitically which contains transformation twins. In Fig. 44 an exceptionally wide original austenite region between the laths transformed into martensite, by deformation, which contains several variants of  $\{112\}$  twins which have very small size and orient themselves in a configuration to accommodate the stresses. Retained austenite may also transform by removing the constraint caused by the surrounding martensite.<sup>(192)</sup> As shown in Fig. 45, since there was no additional constraint around the strip (unlike the case in Fig. 44), very long and larger twins were free to form.

#### 4.5.2. Thermal Instability; Decomposition of Retained Austenite upon Tempering:

As discussed above, during cooling below  $M_s$  the receding austenite regions become increasingly resistant to transformation and small quantities persist to room temperature or below. However, during subsequent tempering at high temperatures (300-400°C), it will decompose thermally, by activated nucleation and growth, to cementite and ferrite. Whereas tempering in the interior of the laths follows the well known clustering and metastable carbide sequence, it appears that  $Fe_3C$  nucleates directly on the austenite-martensite interface. There will be a definite incubation period determined by the tempering temperature until the C concentration along the boundary is high enough to form a carbide embryo and grow with time to attain the critical size of a nuclei. At a sufficiently high tempering temperature,  $T_c$ , this situation is very favorable as far as the chemical and volume free energies are concerned<sup>(176)</sup> (neglecting all the other energies which have relatively small effects). Once the critical nuclei is formed, C diffuses from  $\gamma$  violently and literally pours into the new cementite at the boundary. The C depleted regions in austenite probably transform to ferrite with very low C content by a mechanism

which involves shear (similar to a massive transformation of  $\gamma$  into  $\alpha + \text{Fe}_3\text{C}$  at isothermal hold above  $M_s$  in the upper bainitic region).<sup>(192)</sup> This process is repeated along the  $\alpha'/\gamma$  boundary at the local regions in  $\gamma$ , where C achieves a concentration value in  $\text{Fe}_3\text{C}$ . Hence, islands of  $\text{Fe}_3\text{C}$  form and grow from  $\gamma$ . The easy growth direction must be along the film rather than into the martensite. The particles grow even larger than the retained austenite width leaving, in between, the low C austenite which shears into  $\alpha$ . Hence, the overall transformation is bainitic which involves diffusion and redistribution of C in  $\gamma$  and  $\alpha'$ , and the transformation of remaining  $\gamma$  into  $\alpha$  by the propagation of a coherent  $\alpha'/\gamma$ -interface by a shear process, the kinetics of which depends on the C rejection from  $\gamma$ . In this sense, the reaction is limited by carbon diffusion in  $\gamma$  and at the  $\alpha'/\gamma$ -interface, to form carbides.<sup>(120,121)</sup>

In order to treat the decomposition of this metastable austenite at lower tempering temperatures within the thermodynamical framework, it is necessary to establish  $\alpha/\gamma/\text{carbide}$  phase equilibria which can be derived from the calculated free-energy composition curves for ferrite, cementite and austenite. Some earlier investigators<sup>(153,193)</sup> have studied the subject in detail and arrived at  $\alpha/\text{Fe}_3\text{C}$  and  $\alpha/\gamma/\text{Fe}_3\text{C}$  metastable phase equilibria. The metastable Fe-C equilibrium diagram (Fig. 46) is drawn by using their data.<sup>(153,193)</sup>



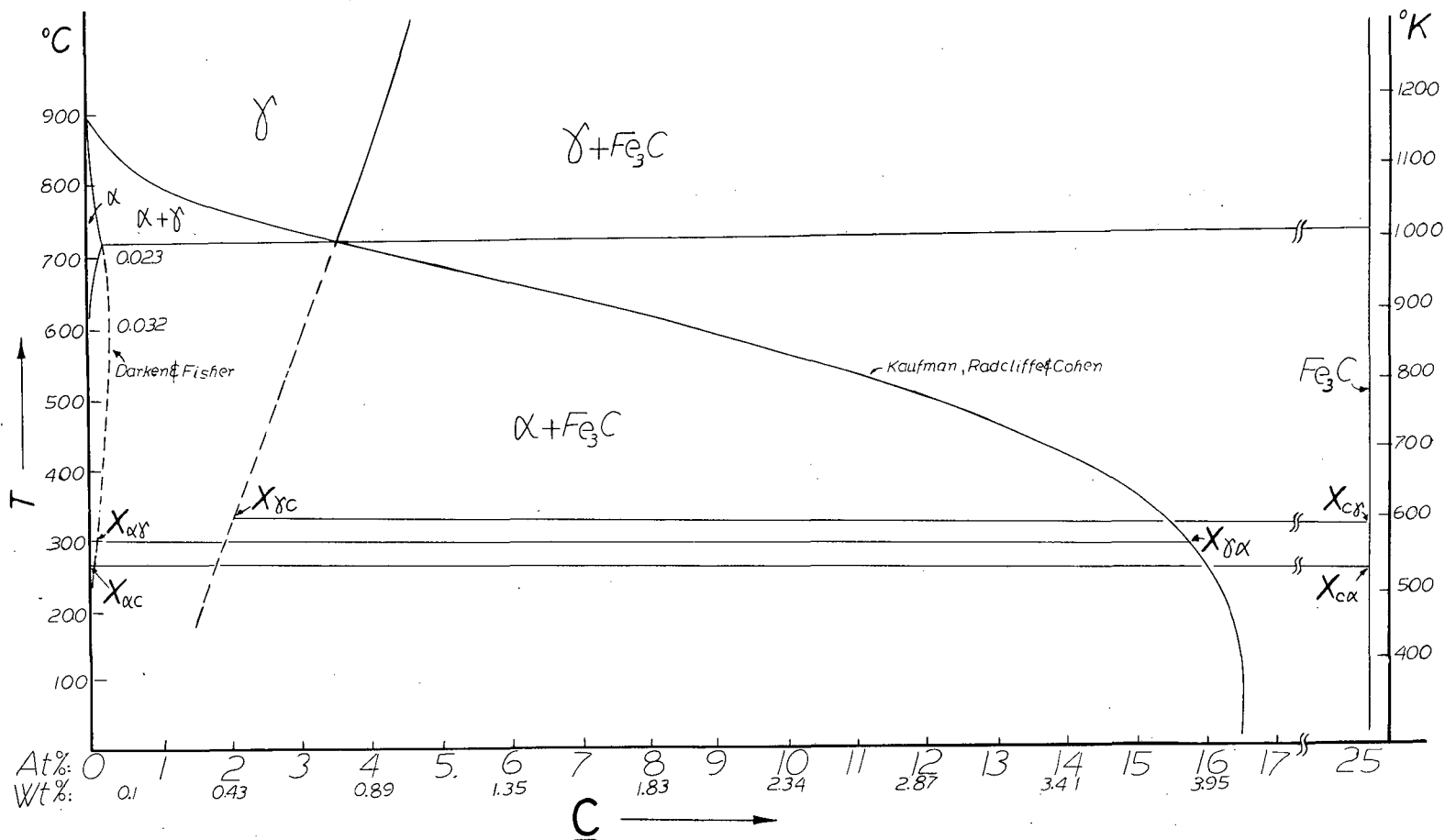


Fig. 46. A portion of the Fe-C phase diagram showing the metastable equilibrium lines between  $\gamma/\alpha$ ,  $\gamma/\text{Fe}_3\text{C}$ , and  $\alpha/\text{Fe}_3\text{C}$  (reproduced from Refs. 153 and 193).  $x_{\gamma\text{C}}$  is an extrapolation of the  $\gamma/\text{Fe}_3\text{C}$  solidus. (No alloying effect.)

XBL 8110-11738

In this diagram,  $x_{\alpha\gamma}$  is the atomic fraction (at. frac.) of C in  $\alpha$  at the  $\alpha/(\alpha + \gamma)$  phase boundary;

$x_{\alpha cm}$  at. frac. of C in  $\alpha$  at  $\alpha/(\alpha + Fe_3C)$  phase boundary;

$x_{\gamma\alpha}$  at. frac. of C in  $\gamma$  at  $\gamma/(\gamma + \alpha)$  phase boundary;

$x_{\gamma cm}$  at. frac. of C in  $\gamma$  at  $\gamma/(\alpha + cm)$  phase boundary;

$x_{cm\gamma}$  and  $x_{cm\alpha}$  at. frac. of C in  $Fe_3C$  at  $cm/(cm + \gamma)$  and  $cm/(cm + \alpha)$  phase boundaries, respectively. From this information one may draw a carbon concentration profile across the ferrite (martensitic) + austenite (retained) structure (Fig. 47). Here the average carbon concentration in the bulk material is taken to be 0.3 wt% (1.4 at%--horizontal broken lines in Fig. 47). The concentrations of the  $\alpha'/\gamma$ -interface and in  $\gamma$  are the average values from the atom probe analysis results (therefore the upper, dashed horizontal line in  $\gamma$  is  $x_{\gamma\alpha}$ ).

Once a nuclei of  $Fe_3C$  concentration is achieved in  $\gamma$ , it will start growing with a rate determined by the C diffusion in  $\gamma$  and through the  $\alpha'/\gamma$ -interface. Because of the favorable chemical potential, the nuclei will form in retained austenite, either on a defect within the film, or on the  $\gamma$  side of the  $\alpha'/\gamma$ -interface. As shown schematically in Fig. 48, C will probably diffuse into the carbide mainly from the austenite phase, in which C has high chemical potential, although some C will also diffuse from martensite, where  $D_C^{\alpha'}$  is very high, and a local equilibrium will be achieved between  $\alpha$  and  $Fe_3C$  at the new  $\alpha/Fe_3C$  interface.

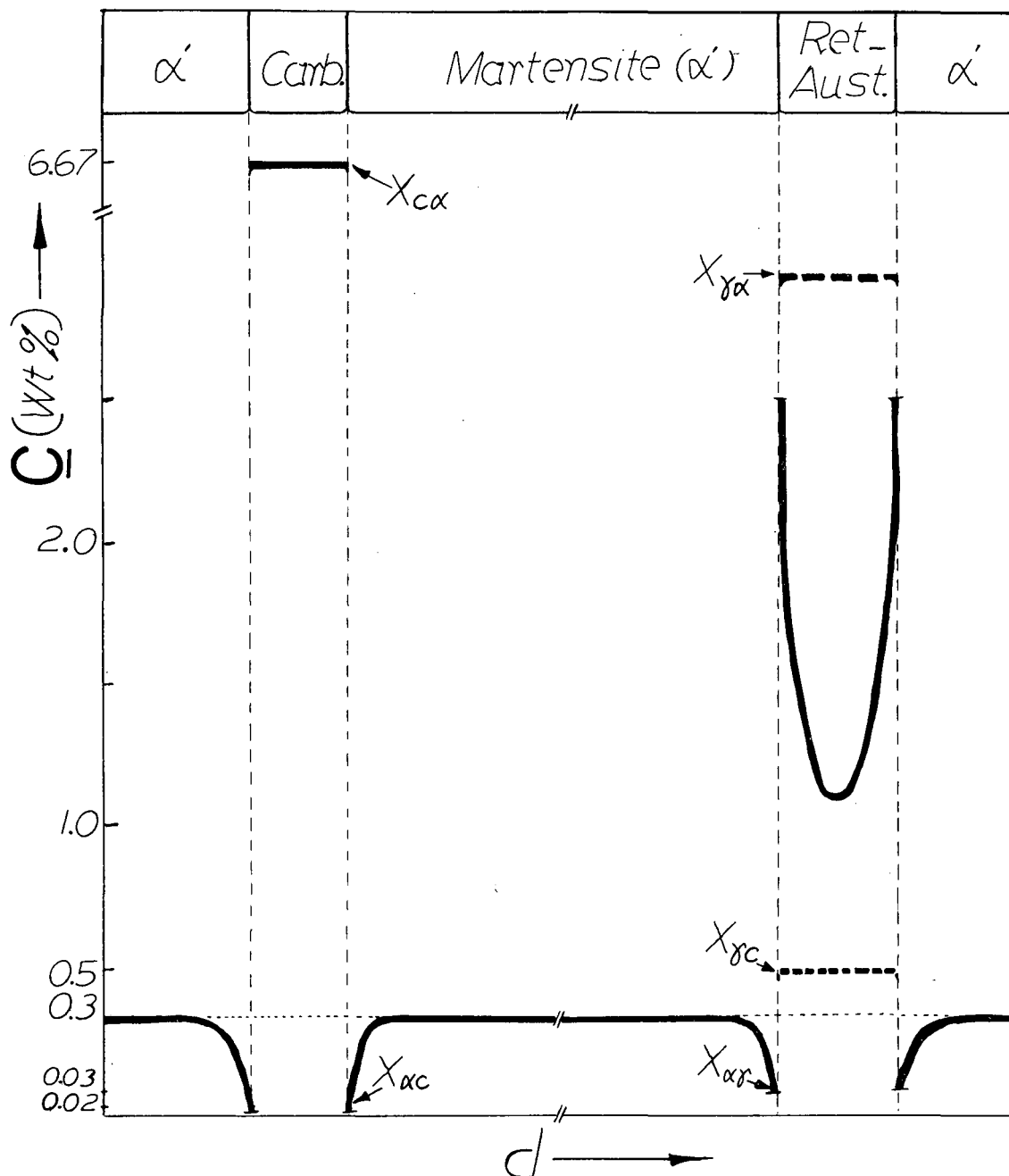


Fig. 47. Schematic representation of the C concentration through  $\alpha'$ , carbides,  $\alpha'/\gamma$  interface and retained austenite in the microstructure.

XBL 8110-11735



There will be C depleted regions in  $\gamma$ , as the C diffuses into the newly formed carbide "islands" along the interface. These regions will then transform into ferrite ( $\alpha$ ) probably by a shear mechanism. Hence, the overall configuration will be a discontinuous "stringer" of carbides along the  $\alpha'/\alpha$  boundary. An actual example of such a configuration is shown in the high magnification TEM images in Fig. 49 which were taken from a sample containing 0.3C tempered at 400°C for one hour.

Note that there should be a local equilibrium between  $\gamma$  and  $\text{Fe}_3\text{C}$  (with  $x_{\gamma\text{cm}} = 0.5$  from Fig. 46). That is, the decomposition reaction will continue until C in  $\gamma$  is 0.5 and cease there, at which point there will be a very small amount of  $\gamma$  left at the interface. Here we also assume that there is no "ferrite bridge" (as suggested by Darken and Fisher) (193) between  $\gamma$  and  $\text{Fe}_3\text{C}$  which may be the reason why the reaction  $\gamma \rightarrow \text{Fe}_3\text{C} + \alpha'$  is observed rather than the reaction  $\gamma \rightarrow \text{Fe}_3\text{C} + \alpha + \gamma$  ( $x_{\gamma\text{C}} = 0.5$ ). The first of these reactions has more driving force (larger -ve  $\Delta G_V$ ) in which case the remaining  $\gamma$  will transform to  $\alpha'$ .

This regime of the transformation temperatures corresponds to an upper bainitic region in a steel with a composition of retained austenite (Fig. 50). This is why the original as-quenched structure has been termed as "incomplete upper bainitic." (40,104,120,121,194)

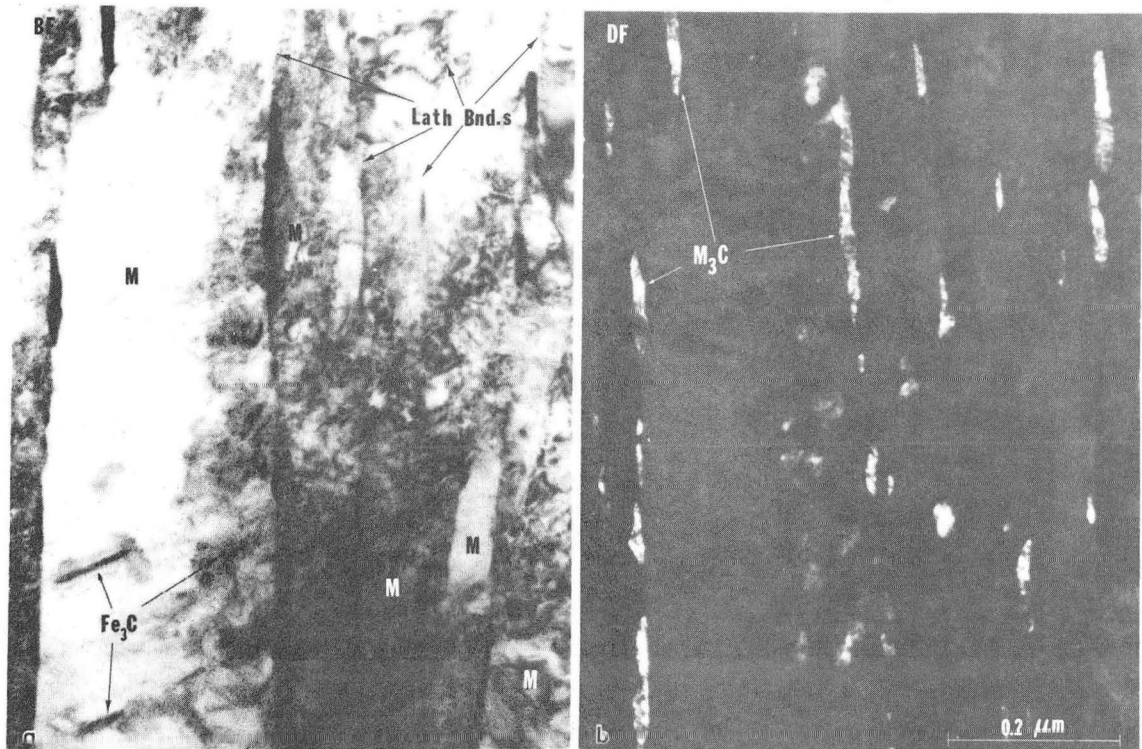


Fig. 49. BF (a) and DF (b) TEM images reveal the "stringers" of discontinuous but elongated carbides transformed from retained austenite at  $\alpha'/\alpha'$  boundary in a tempered specimen (Alloy 4 tempered at 400°C for 1 hour). XBB 821-2

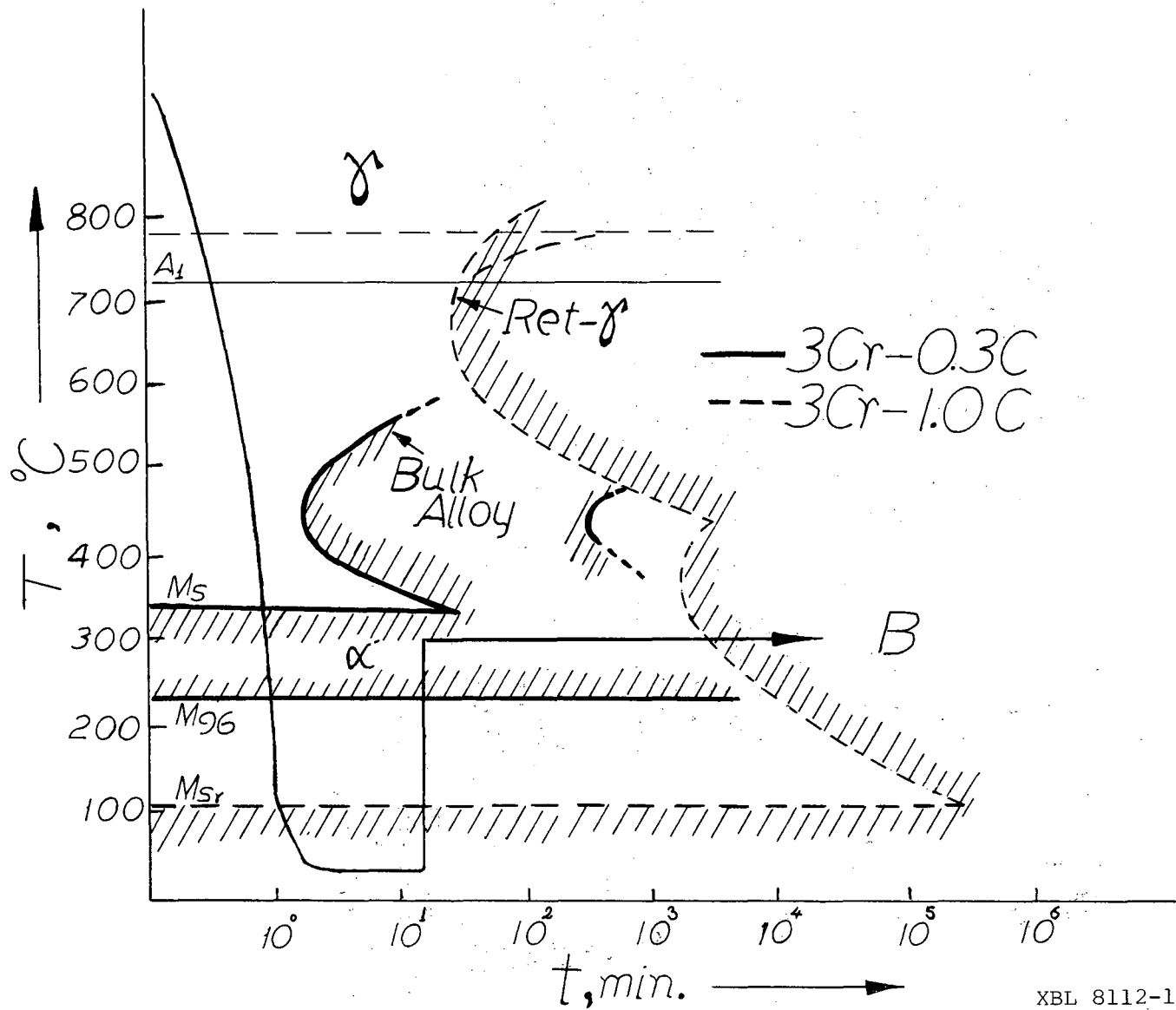


Fig. 50. Superimposed TTT diagrams for base steel and a hypothetical steel (Ref. 195) having the composition of retained austenite.

XBL 8112-13064

#### 4.6. CONCLUSIONS

(i) Retained austenite has been identified in a number of low and medium carbon steels as continuous films (width usually between 50 to 200 Å) with a total amount less than 5% by volume.

(ii) Although no partitioning of substitutional solute elements (such as Cr, Mn, Mo, Ni) was detected, a considerable amount of carbon does partition into the austenite (2-3 at% or 0.6-0.8 wt%) and to the  $\alpha'/\gamma$ -interface (around 10 at% or 2.5 wt%). Correspondingly, carbon drops to very low values in the martensite near the boundary. The high carbon content produces considerable chemical stabilization of the austenite.

(iii) Thermal and mechanical stabilizations appear to be responsible for the presence of  $\gamma$ . In thermal stabilization the movement of the  $\alpha'/\gamma$  interface is pinned by the high density of carbon clusters at the interface. The retained austenite is mechanically stabilized because of the accommodation of the stresses created during the  $\gamma$  to  $\alpha'$  transformation which highly deforms  $\gamma$  ahead of the interface inhibiting its further advance.

(iv) Removing the volume constraint and recovering the films from their defects may cause the retained austenite (containing high carbon) to decompose to plate martensite.



(v) Metastable austenite persists during low temperature aging (i.e., 200°C). It decomposes, however, to a morphology very similar to "upper bainite" during aging at higher temperatures (i.e., 300-400°C).

## 5.1. APPENDIX-1

A COMPUTER PROGRAM TO PLOT STEREOGRAPHIC PROJECTION AND  
COMPOSITE STEREOGRAPHIC PROJECTIONS FOR MARTENSITE AND  
AUSTENITE HAVING DIFFERENT ORIENTATION RELATIONSHIPS

An existing main-frame computer program was modified to plot stereographic projections (s-p) for any crystal system by a PDP-11 minicomputer.\* This may also provide a handy method of indexing electron diffraction patterns (e.g., Ref. 94). For orientation relationship analysis one can superimpose composite s-p for each phase. The angular relationships between the planes and/or the directions can be discerned from this by inspection. Data consists of the lattice parameters ( $a_0$ ,  $b_0$ ,  $c_0$ ), the angles between the principal directions ( $\alpha$ ,  $\beta$ ,  $\gamma$ ) indices of the central pole, that of a pole on the great circle and the radius of the great circle.

Three very commonly observed O.R.s between  $\alpha'$  and  $\gamma$  are plotted in Fig. A1-1. In all of these cases there is at least one common direction (or plane) in both phases (center). The other pole (on the great circle) may be coincident for both phases; in which case both stereograms are plotted regularly. If none of the poles in each phase are coincident, then the second stereogram is simply rotated about the center in an appropriate amount (e.g., for G-T O.R., the austenite stereogram is rotated  $2.5^\circ$  with respect to martensite, i.e., the angle between  $(1\bar{1}1)_\gamma$  and  $(\bar{1}10)_\alpha$ ).

---

\*Program can be supplied upon request by the author.

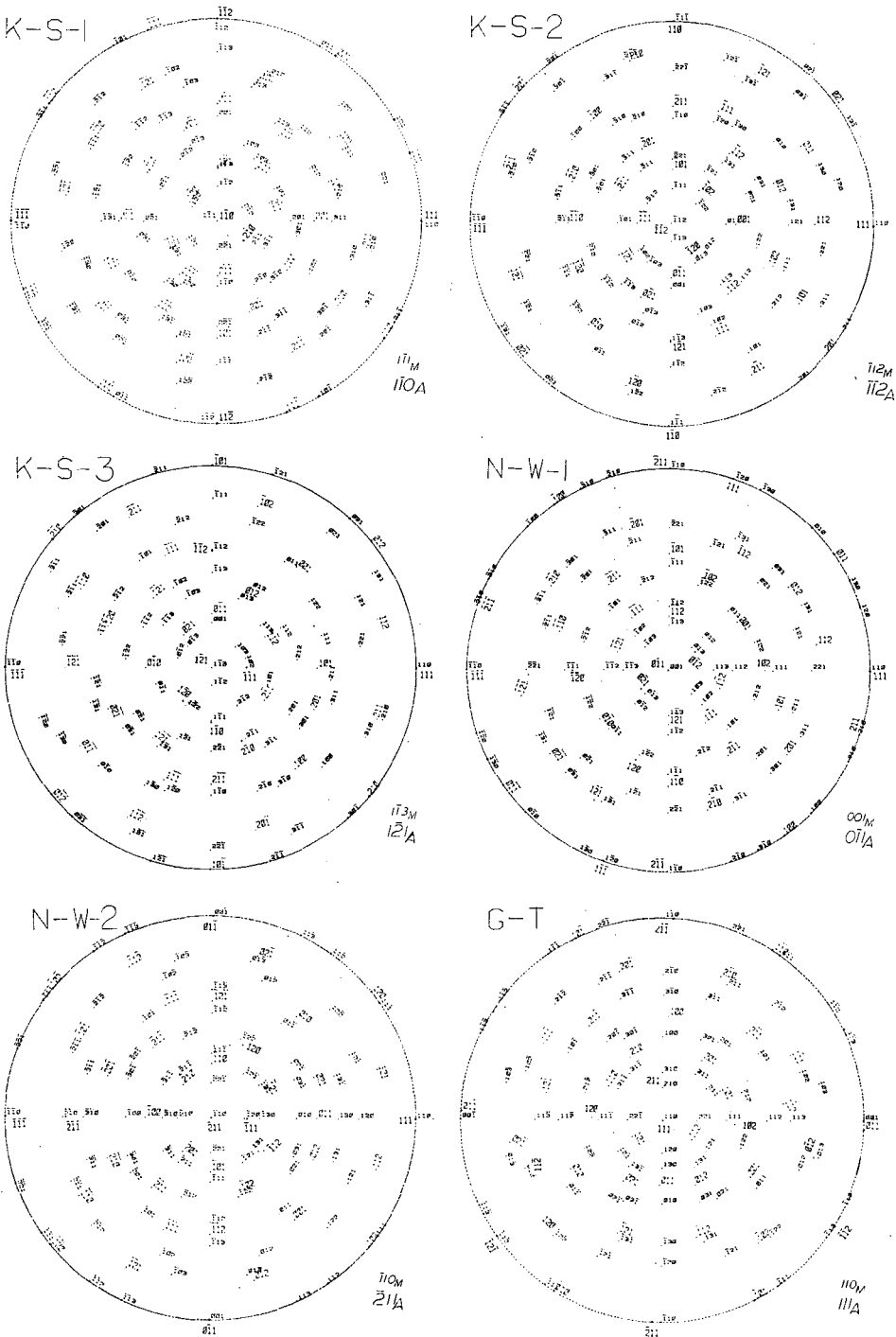


Fig. A1-1. Computer plotted stereographic projections for austenite and martensite for different Orientation Relationships. XBL 825-9884

## 5.2. APPENDIX-2

VARIATION OF THE LATTICE PARAMETERS OF AUSTENITE AND  
 MARTENSITE WITH ALLOYING ADDITIONS AND AN ATTEMPT TO  
 MEASURE LATTICE PARAMETER OF MARTENSITE BY CBED TECHNIQUE

For calculating the lattice parameter of retained austenite, the formula<sup>(140,141)</sup> " $a = 3.555 + 0.04 \times \text{wt\% C}$ " was used. This formula has been adjusted so that it accounts for the state of retained austenite, because there is a volume constraint in retained austenite by the surrounding martensite matrix. However, in our case retained austenite strips are free from any kind of matrix constraints (see Fig. A2-1c). Hence, instead, the formula for the equilibrium austenite lattice parameter<sup>(24,140-142)</sup> should be used. That is,  $a = 3.573 + 0.033 \text{ wt\% C}$  (see, e.g., Ref. 141). Note also that other alloying elements, interstitials, such as N, and substitutionals, in steels also effect the lattice parameter in retained austenite although slightly.<sup>(24)</sup> In the particular case above, the alloy contains 2 wt% Si whose effect is negligible, because of the small amount (less than 1 in 10000 at 2 wt% Si). Nonetheless, the below formulae which relate the lattice parameter change in equilibrium  $\gamma$  as a function of the alloying elements in steels are given for further information:<sup>(142)</sup>

$$(i) \ a_0 (\pm 0.0016) = 3.5780^* + 0.0330C + 0.0220N + 0.0095Mn \\ (\pm 0.0110) (\pm 0.00015) - 0.0002Ni + 0.006Cr + 0.0220N$$

\*3.5730 according to Ref. 141.

$$\begin{aligned}
 & (\pm 0.00004) (10.0003) (\pm 0.0034) + 0.0056\text{Al} \\
 & - 0.0004\text{Co} + 0.0015\text{Cu} + 0.0031\text{Mo} + 0.0051\text{Nb} \\
 & + 0.0039\text{Ti} (\pm 0.0004) (\pm 0.0012) (\pm 0.0009) + 0.0018\text{V} \\
 & + 0.0018\text{W} (\pm 0.0004) (\pm 0.0003) \dots \text{ (In wt\%)}
 \end{aligned}$$

$$\begin{aligned}
 \text{(ii) } a_o (\pm 0.0021) &= 3.5770 + 0.0065\text{C} + 0.0056\text{N} \\
 & (\pm 0.00004) (\pm 0.0003) (\pm 0.0011) + 0.0010\text{Mn} (\pm 0.0029) \\
 & (\pm 0.0002) - 0.0002\text{Ni} + 0.0006\text{Cr} + 0.0028\text{Al} \\
 & - 0.0004\text{Co} + 0.00014\text{Cu} (\pm 0.00045) (\pm 0.0002) (\pm 0.0007) \\
 & + 0.0053\text{Mo} + 0.0079\text{Nb} + 0.0032\text{Ti} (\pm 0.0006) (\pm 0.0027) \\
 & (\pm 0.0010) + 0.0017\text{V} + 0.0057\text{W} (\pm 0.0004) (\pm 0.0012) \text{ (at\%)}
 \end{aligned}$$

Many attempts have been tried to determine the lattice parameter of the martensite matrix with different carbon content. Because of the heavy dislocation density, residual stresses, and multiple scattering, there was not enough volume in martensite to contribute to form a CBED pattern; although very small diameter ( $<100 \text{ \AA}$ ) electron probes, which were produced by a Field Emission Gun, were used. An example of a martensite (111) CBED pattern is shown in Fig. A2-1a. In the central disc, the parallel concentric fringes are extinction contours due to the foil thickness. There is no other feature (e.g., HOLZ lines, Kikuchi lines) which would otherwise be present in a CBED pattern, such as the one in Fig. A2-1b which was taken from retained austenite. Further study will be continued on this aspect of the research by exploring new methods to prepare dislocation free matrix.

The formulae which relate the lattice parameters (a and c) of martensite to C content are given below for further use:

$$a (\text{\AA}) = 2.8664 - 0.01303 \text{ wt\% C} \quad (\text{Ref. 24, 141})$$

$$c (\text{\AA}) = 2.8664 + 0.1162 \text{ wt\% C} \quad (\text{Ref. 24, 141})$$

Cr ( $a_0 = 2.8847$ )<sup>(139)</sup> or Mo ( $a_0 = 3.1469$ )<sup>(139)</sup> can be used as reference material.

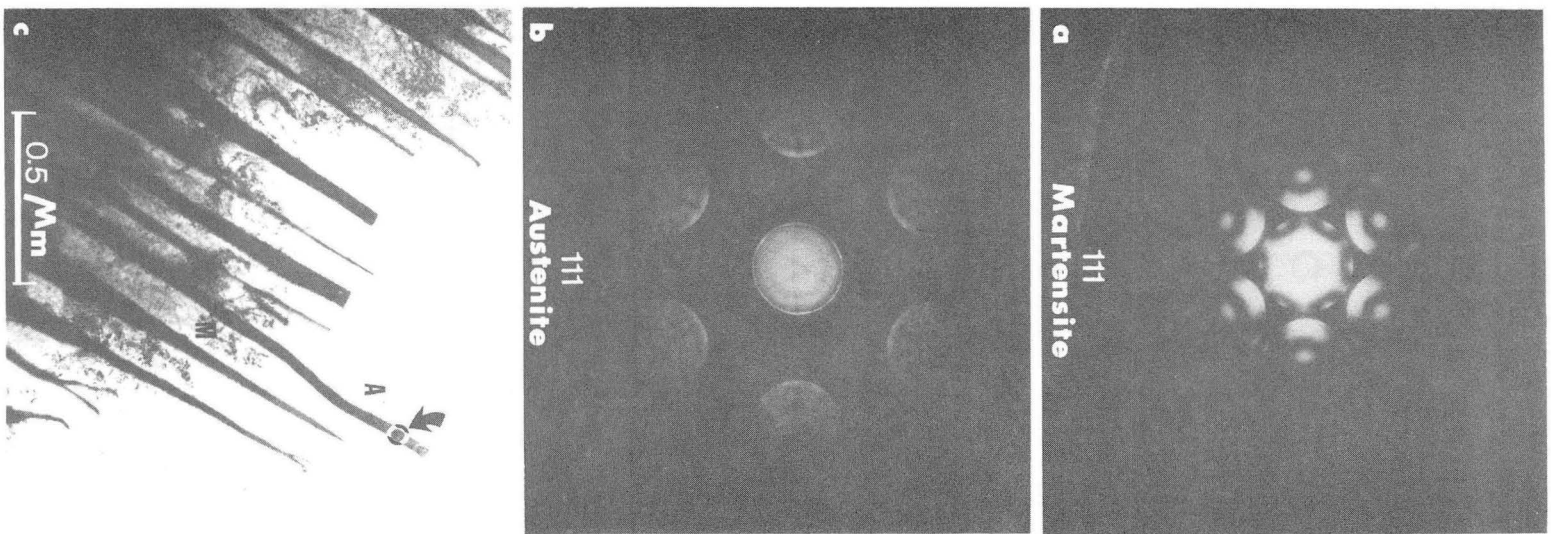


Fig. A2-1. CBED patterns for martensite (a) and austenite (b) in (111) zone axis orientations. Details of the HOLZ lines are missing in pattern (a) due to heavy dislocations in martensite. Pattern (b) which reveals HOLZ lines was taken from the region shown in (c). Note in (c) that the austenite "fingers" are free from surrounding matrix.

XBB 825-4328

## 5.3. APPENDIX-3

CRITICAL DIFFUSION TIME DURING LATH GROWTH AND THE  
PREDICTION OF THE GROWTH RATE OF MARTENSITE LATHS

The concentration gradient, determined by AP, showed that while C is depleted in  $\alpha'$  near the boundary it is increased in  $\gamma$  to twice that of the bulk value and rises to much higher values (5-10 at%) at the  $\alpha'/\gamma$  interface. An approximation on the distance that C had to travel to form this concentration profile can be obtained. Assuming the thickness of the boundary ( $d_b$ ) to be 20 Å; austenite half thickness to be 80 Å (Fig. A3-1d); and taking  $C_o = 1.2$  at%, the distance,  $d_x$ , to be travelled by C to achieve the C profile, is found to be 600 Å from the two-dimensional geometry of the boundary region.

This C redistribution takes place during quenching between  $M_s$  and  $M_f$  (330 and 260°C for 2 Mn alloy, respectively). However, one can make an assumption that the quenching is interrupted for a time period of  $t_c$  at  $T_c$  (Fig. A3-1b). For  $T_c$  equal to 290°C (536°K), and from  $d_x = 2\sqrt{D_C^{\alpha'}} t_c$  (diffusion distance travelled by C during  $t_c$  where  $D_C^{\alpha'}$  is the diffusion coefficient of C in  $\alpha'$ , Appendix 4) at  $T_c$  one finds  $t_c$  to be about 0.04 Sec. (This figure is a lower bound for  $t_c$  which applies provided that adequate driving force exists for C to diffuse in  $\alpha'$ .)

This is a period during which the carbon concentration gradient is formed and is a measure of the time that lath



thickens to its final dimension. Hence, taking this as the available time for the growth, one can find an approximate value for the sidewise growth rate. Taking the average lath thickness between 0.1 to 0.5  $\mu\text{m}$ , the growth rate lies between  $10^4$  to  $10^5$   $\text{\AA}/\text{sec}$ . The growth rate predicted for plate martensite is  $10^5$   $\text{cm}/\text{sec}$ . (154,155) ( $10^{13}$   $\text{\AA}/\text{sec}$ .); for bainite it has been measured to be  $10^{-6}$   $\text{cm}/\text{sec}$ . ( $10^2$   $\text{\AA}/\text{sec}$ .). (156-158)

From the study in Ref. 33 (the only observations on this subject) by the rough measurements made using Fig. 11 of this reference one may predict the sidewise growth rate of martensite laths to be about  $3 \times 10^4$   $\text{\AA}/\text{sec}$ . This value lies within the qualitatively predicted range found in the above appendix. [However, it should be strongly mentioned here that the lath growth is not linear and proceeds at a decelerating rate as the temperature decreases within the  $M_s$ - $M_f$  range (probably exponentially). This is actually the case in bainite growth. (158,159) As  $T$  decreases,  $D_c$  also decreases continuously; hence  $t_c$  can be different. However, this discrepancy is not expected to be very large. The reason to keep the sidewise growth rate in a large range (i.e.,  $10^4$  to  $10^5$   $\text{\AA}/\text{sec}$ .) is partly because of this discrepancy.]

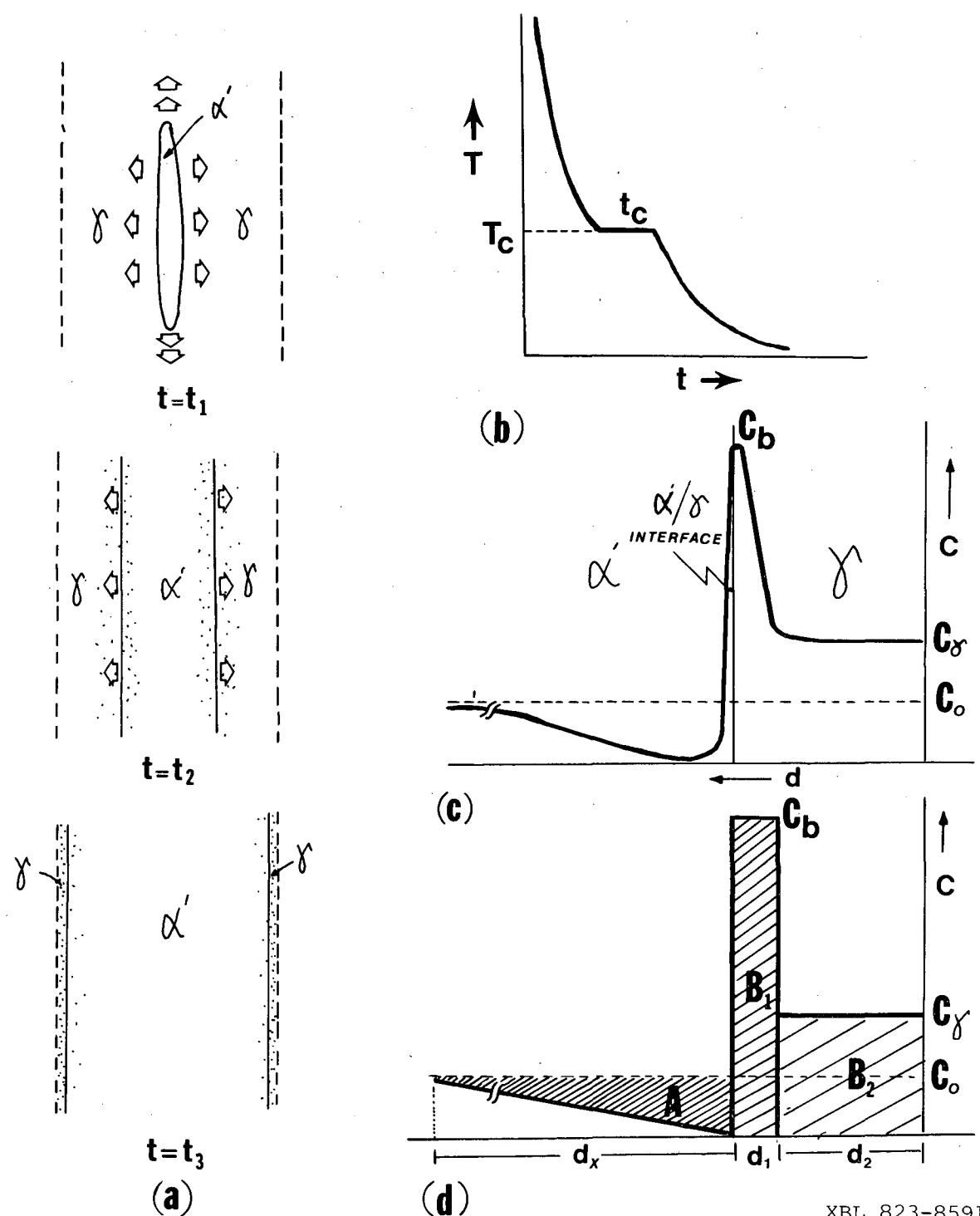


Fig. A3-1. (a) Schematic illustration of the possible sequence of sidewise and lengthwise growth of laths (arrows). The dots represent the C redistribution. (b) The step at  $T_c$  in the cooling curve is a hypothetical interruption ( $t_c$ ) which is equivalent to the time elapses during cooling between  $M_S$  and  $M_F$ . (c) Approximate C profile similar to those determined by FIM-APA. (d) Illustration of the amount of C in each region.

XBL 823-8591

## 5.4. APPENDIX-4

## DIFFUSION COEFFICIENTS OF CARBON IN MARTENSITE AND AUSTENITE

A number of investigations in the literature have reported the measurements of the diffusion coefficients of carbon in ferrite ( $D_C^\alpha$ ). These determinations have been done theoretically as well as experimentally using different techniques and employing statistical methods. The values given lie within the similar range and the most frequently cited ones are as follows:

$$D_C^\alpha = 0.008 \exp\left(-\frac{19800}{RT}\right) \quad \dots (1) \quad (160)$$

$$D_C^\alpha = 0.02 \exp\left(-\frac{20100}{RT}\right) \quad \dots (2) \quad (161)$$

$$D_C^\alpha = 0.002 \exp\left(-\frac{19817}{RT}\right) \quad \dots (3) \quad (162)$$

$$D_C^\alpha = 0.05 \exp\left(-\frac{21100}{RT}\right) \quad \dots (4) \quad (163)$$

$$D_C^\alpha = 0.004 \exp\left(-\frac{19160}{RT}\right) \quad \dots (5) \quad (164)$$

$$D_C^\alpha = 0.02 \exp\left(-\frac{21110}{RT}\right) \quad \dots (6) \quad (165)$$

The values of  $D_C^\alpha$  given here are more or less in the temperature range between ambient temperatures and 500°C and hold for the composition of C of about 0.3 wt% (no alloying element effect). These values are plotted in Fig. A4-1a. The best fit (represented by the dotted line in the figure) corresponds to  $D_C^{\alpha'} = 0.0173 \exp\left(-\frac{20180}{RT}\right)$ . It should be noted that because of the tetragonality of martensite  $D_C^{\alpha'}$  is

a little lower than  $D_C^\alpha$  (because of the increase in activation energy).

The same sort of analyses were performed for the diffusion of C in  $\gamma$ , i.e.,  $D_C^\gamma$ ; frequently cited values are as follows:

$$D_C^\gamma = 0.08 \exp\left(-\frac{31000}{RT}\right) \quad \dots\dots(7) \quad (166)$$

$$D_C^\gamma = 0.33 \exp\left(-\frac{35500}{RT}\right) \quad \dots\dots(8) \quad (167)$$

A recent theoretical analysis also stated that <sup>(168)</sup>

$$D_C^\gamma = 0.0001 \exp\left(-\frac{26143}{RT}\right) \quad \dots\dots(9)$$

These values are all for high temperature (i.e.,  $T > 700^\circ\text{C}$ ) in the austenite range. For our purpose of interest for the calculations in the text the extrapolated values were used, for the retained austenite, the best fit of which gives

$$D_C^\gamma = 0.010 \exp\left(-\frac{30880}{RT}\right)$$

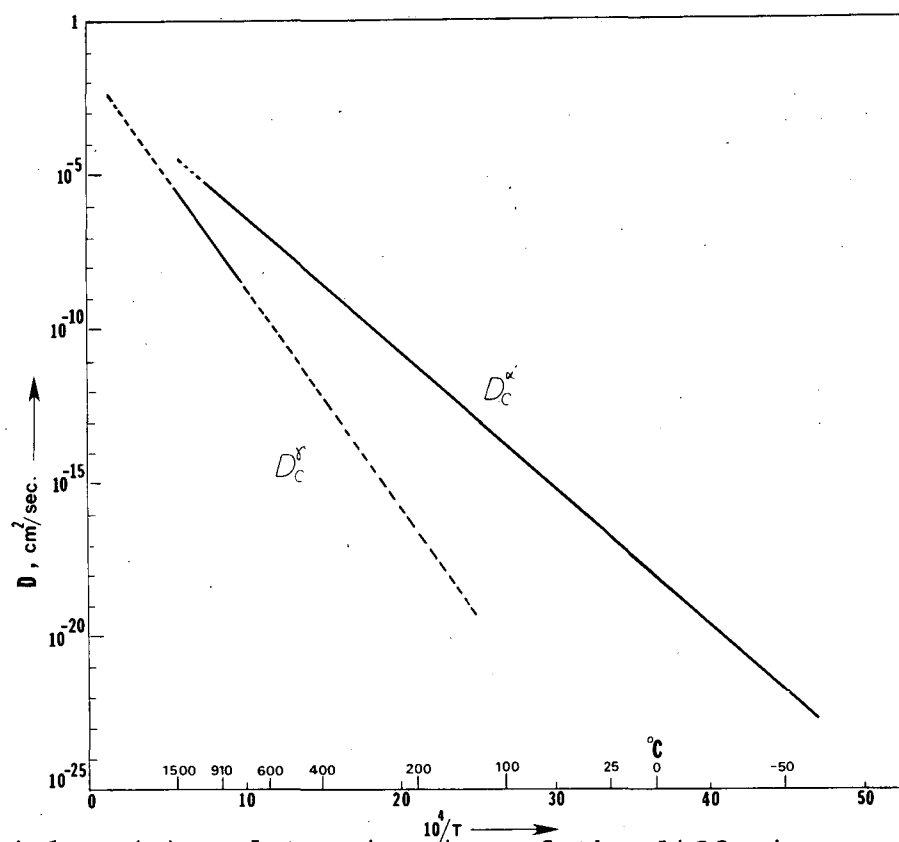
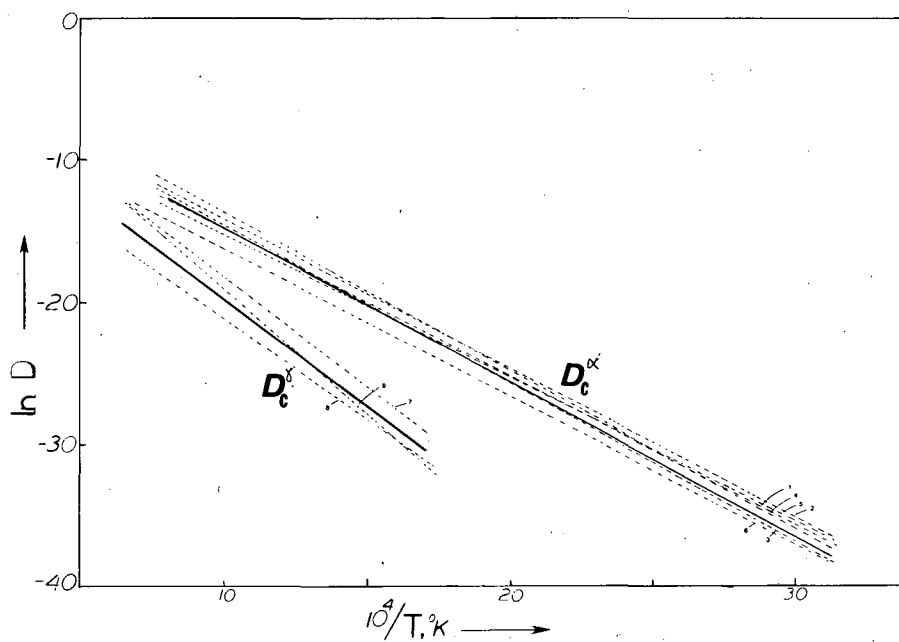


Fig. A4-1. (a) Redetermination of the diffusion coefficients of carbon in martensite ( $D_C^{\alpha}$ ) and austenite ( $D_C^{\delta}$ ) (the numbers on the curves correspond to the eqn. numbers in the text). (b) Lines of the average values of  $D_C^{\alpha}$  and  $D_C^{\delta}$ .

XBL 825-9773

## 5.5. APPENDIX-5

EFFECTIVE DIFFUSION DISTANCE FOR CARBON DURING THE  
TRANSFORMATION WITHIN  $M_s$ - $M_f$  RANGE

C diffuses to  $\alpha'/\gamma$  interface during quenching, as well as to the dislocations within laths. The assumption is that the lath boundaries behave as infinite sinks for C. Also, the boundaries are considered to be fixed in space and all of the complications resulting from their movement during quenching are ignored. The diffusion problem is reduced to one with boundary conditions where  $C_b = 0$  (carbon concentration at the interface on  $\alpha'$  side).<sup>(169)</sup> The effective diffusion distance is given by (see Ref. 173 for further discussion):

$$(Dt)_{\text{eff.}} = \frac{1}{\alpha} \left(\frac{k}{h}\right) \left(\frac{V}{A}\right) \int_{25^\circ}^{M_s} \frac{D(T)}{(T - 20^\circ)} dT \dots (3)$$

where  $\alpha$ : thermal diffusivity (= 0.070 cm<sup>2</sup>/sec)<sup>(172)</sup>

$$\frac{h}{k} = \left( \frac{\text{heat transfer coefficient of the quenching medium}}{\text{thermal conductivity of the specimen}} \right) = 1.58 \text{ cm}^{-1}, \text{ brine quench}$$

$\frac{A}{V}$ : Area to Volume ratio of the specimen

T: Temperature of the specimen (Austenitizing temperature)

$T_q$ : Temperature of the quenching medium.

Here the value of  $D(T)$  is taken from the previous appendix (new value for  $D_c$ ). The effective diffusion distance for various sample geometries for ice brine and oil quenching

can be calculated by numerical analysis of the integral.

The limits of integral were chosen as  $M_s$  and  $M_f$  (not  $25^\circ\text{C}$  since we are only interested in the C diffusion within  $M_s$ - $M_f$  range, although some diffusion still occurs below  $M_f$ ). The sample considered for the analysis contains 0.27 wt% C with  $M_s$  and  $M_f$  values  $350^\circ\text{C}$  and  $250^\circ\text{C}$ , respectively.

Sample		$(Dt)_{\text{eff.}}, \text{cm}^2$	$x = 2\sqrt{(Dt)_{\text{eff.}}}, \text{\AA}$
A	IB	$2.18 \times 10^{-11}$	661
	AO	$3.9 \times 10^{-11}$	882
B	IB	$3.40 \times 10^{-11}$	831
	AO	$6.14 \times 10^{-10}$	1109

$(h/k)^{(172)}$ : 1.58 still brine (IB)  
 $\sim 1.00$  agitated oil (AO)

Sample dimensions: A: 0.1 cm x 0.1 cm x 1.5 cm  
 B: 0.1 cm x 1.0 cm x 1.5 cm

## 5.6. APPENDIX-6

## INTERSTITIAL ATOM-DISLOCATION INTERACTION

Solute atoms segregating to the dislocations reduce the elastic energy of the local regions around the dislocations by an amount determined by the binding energy between the interstitial atom and the dislocation core.<sup>(178)</sup> Therefore, the movement of a dislocation is hindered by this amount ( $\Delta F_i$ ).<sup>(178,182,183)</sup> Hence, whether an applied or available chemical driving force could move the dislocations can be predicted. For example, in a martensitic transformation, the austenite/martensite interface contains dislocation networks.<sup>(1,2,25)</sup> The amount of drag force opposing to interface movement because of the carbon build-up at the dislocations (i.e., "Cottrell Atmospheres"<sup>(178)</sup>) may be determined as follows. The available free energy for austenite to martensite transformation at  $M_s$ , i.e.,  $\Delta G^{\gamma \rightarrow \alpha'}$ , is 300-400 Cal/mole.<sup>(19,24,78,111,184)</sup> The amount of carbon at the  $\alpha'/\gamma$  interface is about 10 at% (from the atom probe data in the text) or about  $10^{13} - 10^{14}$  carbon atoms/cm<sup>2</sup>; the separation between the dislocations at the interface is about 15 Å (the average of the values given in Refs. 25, 108, 159, 178). The density of dislocations,  $\delta$ , then, is  $10^{14}$ /cm<sup>2</sup>. These values correspond to about 1 carbon atom per dislocation at the interface plane. Therefore, the total binding energy of carbon atoms at the dislocations at the interface,  $(\Delta F_i)_T$ , is about  $10^{14}$  eV (given that  $F_i = 1$  eV/atom/



dislocation, for carbon in Fe).<sup>(178)</sup> The chemical force available to move the dislocations by one Burgers vector,  $\Delta F_C$ , is approximately  $10^{12} - 10^{13}$  eV/cm<sup>2</sup>. Noting that  $\Delta F_C$  and  $(\Delta F_i)_T$  are of opposite sign and have comparable magnitude, and  $\alpha'/\gamma$  interface movement is then prevented by pinning of the dislocations by C atoms at the interface.

## 6. ACKNOWLEDGEMENTS

I appreciate and acknowledge the opportunities created by Professor G. Thomas who has supervised and supported the projects involved in this thesis. I am grateful to Dr. R. M. Fisher whose invaluable advice and interests were stimulating. Deep appreciation and thanks are also extended to Professors P. M. Kelly and K. E. Easterling, and Drs. B. V. Narasimha Rao, W. M. Kriven and J. W. Steeds whose interests, suggestions, and help made direct contributions to different parts of this research.

The continuous moral support from my parents and friends, Channing and Ulrich, and from Madeleine Penton, who has also kindly typed the manuscript, has been valuable. I thank Ondrej Krivanek and Peter Rez for showing me "the real world of microscopy."

Atom Probe Analyses were made in collaboration with Drs. S. J. Barnard, G. D. W. Smith (Oxford University), M. K. Miller and S. S. Brenner (U.S. Steel Co.).

Professors I. Finnie and A. G. Evans critically reviewed and commented on the manuscript.

I gratefully acknowledge the Science Scholarship from TUBITAK-BAYG (Turkey) and appreciate the research facilities and technical staff provided by Lawrence Berkeley Laboratory.

This work was supported by the Director, Office of Energy Research, Office of Basic Energy Science, Material Science Division of the U.S. Department of Energy under Contract No. DE-AC03-76SF00098.

## 7. REFERENCES

1. M. Cohen and C. M. Wayman, "Treaties in Metallurgy," J. K. Tien and J. F. Elliott (eds), TMS-ASM (1981).
2. J. W. Christian, "Physical Properties of Martensite and Bainite," Special Report #93, The Iron and Steel Inst. (1965), 1-25.
3. G. V. Kurdjumov and A. G. Khachaturyan, Acta Met., 23 (1975), 1077-1088.
4. Z. Nishiyama, "Symp. on Mart. Trans.," Mem. of the Ins. of Sci. and Ind. Res., Osaka Univ., XXII (1965), 1-39.
5. M. Cohen, "Phase Transformations in Solids," R. Smaluchowski, J. E. Mayer, and W. A. Weyl (eds), John Wiley and Sons (1951), Ch. 17, 588-660.
6. C. M. Wayman, Metallography, 8 (1975), 105-130.
7. M. Cohen, G. Olson, and P. C. Clapp, Proc. ICOMAT '79, MIT Press (1979), 1-11.
8. A. L. Roitburd and G. V. Kurdjumov, Mat. Sci. and Eng., 39 (1979), 141-167.
9. C. M. Wayman, "Int. to Crystallography of Martensitic Transformations," Macmillan Co., New York (1964).
10. Z. Nishiyama, "Martensitic Transformations," Academic Press, New York (1978).
11. G. K. Bansal and A. H. Heuer, I-Acta Met., 20 (1972), 409-417; II-ibid., 22 (1974), 1281-1289.
12. G. M. Wolten, Acta Crystallogr., 17 (1964), 736-765.

13. E. C. Subbaro, H. S. Maiti, and K. K. Srivastava, *Phys. Stat. Sol.*, A, 21 (1974), 9-40.
14. C. J. Altstetter and C. M. Wayman, *Acta Met.*, 10 (1962), 992-
15. P. M. Kelly and J. Nutting, *JISI*, 197 (1961), 199-211.
16. T. Bell and W. S. Owen, *JISI*, 203 (1967), 428-435.
17. G. Thomas, *Met. Trans.*, 2 (1972), 2373-2386.
18. A. R. Marder and G. Krauss, *Trans. ASM*, 62 (1969), 957-969.
19. M. Cohen, E. S. Machlin, and V. G. Paranjpe, "Thermodynamics in Physical Metallurgy," *ASM* (1949), 242-271.
20. E. S. Machlin and M. Cohen, *Trans. AIME (JOM)*, 4 (1952), 489-500.
21. L. Kaufman and M. Cohen, *Progr. Metal Phys.*, 7 (1958), 165-246.
22. S. R. Pati and M. Cohen, *Acta Met.*, 17 (1969), 189-199.
23. C. L. Magee and R. G. Davies, *Acta Met.*, 20 (1972), 1031-1043.
24. J. M. Moyer and G. S. Ansell, *Met. Trans.*, 6A (1975), 1785-1791.
25. G. Olson and M. Cohen, *Acta Met.*, 27 (1979), 1907-1918.
26. A. R. Troiano and A. B. Greninger, *Metal Progress*, 50 (1946), 30-
27. D. S. Lieberman, *Acta Met.*, 6 (1958), 680-693.
28. F. C. Frank, *Acta Met.*, 1 (1953), 15-21.

29. F. Osmond, "Microscopic Analysis of Iron-Carbon Alloys," Bulletin del a Soc. d'Encouragement pour L'Industrie National, 10 (1895), 480-490.
30. P. M. Kelly and J. Nutting, Proc. Roy. Soc. (A), 259 (1960), 45-58.
31. C. M. Wayman, Adv. Mat., H. Heman (ed.), 3 (1968), Interscience, New York, 147-160.
32. W. S. Owen, F. J. Schoen, and G. R. Srinivasan, Proc. "Phase Transformations" (ASM) (1968), 157-180.
33. G. Krauss and A. R. Marder, Met. Trans., 2 (1971), 2243-2257.
34. K. Shimizu and Z. Nishiyama, Met. Trans., 3 (1972), 1055-1068.
35. T. Maki and C. M. Wayman, Acta Met., 25 (1977), 681-693.
36. F. J. Schoen, J. L. Nilles, and W. S. Owen, Met. Trans., 2 (1971), 2489-2494.
37. V. Raghavan and M. Cohen, Met. Trans., 2 (1971), 2408-2418.
38. J. Christian, Proc. ICOMAT '79, Cambridge, MIT Press (1979), 220-234.
39. K. Wakasa and C. M. Wayman, Acta Met., 29 (1981), 991-1012.
40. B. V. Narasimha Rao and G. Thomas, Proc. ICOMAT '79, Cambridge, MIT Press (1979), 12-21.
41. S. K. Das and G. Thomas, Trans. ASM, 62 (1969), 659-665.

42. D. H. Huang and G. Thomas, *Met. Trans.*, 2 (1971), 1587-1594.
43. J. Y. Koo and G. Thomas, *Met. Trans.*, 8A (1977), 525-533.
44. G. Thomas, *Battelle Colloquim on Fundamental Aspects of Structural Alloy Design*, R. I. Jaffee and B. A. Wilcox (eds), Plenum Publ. Co. (1977).
45. B. V. Narasimha Rao and G. Thomas, *Met. Trans.* 11A (1980), 441-457.
46. M. K. Miller, P. A. Beaven, and G. D. W. Smith, *Surface and Interface Ana.*, 1, No. 5 (1979), 149-160.
47. S. S. Brenner, *Surface Science*, 70 (1978), 427-451.
48. M. K. Miller, Ph.D. Thesis, Univ. of Oxford (1977).
49. E. G. Bain, *Trans. AIME*, 70 (1924), 24-46.
50. A. Gilbert and W. S. Owen, *Acta Met.*, 10 (1962), 45-54.
51. T. Maki, S. Shimooka, T. Arimoto, and I. Tamura, *Trans. JIM*, 14 (1973), 62-67.
52. G. S. Ansell, M. J. Carr, and J. R. Strife, *Japan Inst. of Metals, Proc. 1st JIM Symp. on "New Aspects of Martensitic Transformations,"* Kobe, Japan (1976), 53-58.
53. Y. Tanaka and K. Shimizu, *Trans. JIM*, 21 (1980), 34-45.
54. R. G. Davies and C. L. Magee, *Met. Trans.*, 2 (1971), 1939-1947.
55. R. F. Mehl and D. M. Van Winkle, *Societe Francaise de Metallurgie*, L, No. 7 (1953), 465-475.

56. A. J. Baker, P. M. Kelly, and J. Nutting, "Phase Transformations," ASM, Ch. 20 (1970), 899-916.
57. V. G. Paranjpe, M. Cohen, M. B. Bever, and C. F. Floe, Trans. AIME (JOM), 188 (1950), 261-267.
58. T. Bell and W. S. Owen, Trans. AIME, 239 (1967), 1940-1949.
59. M. G. A. Biswas and I. Codd, JISI, 204 (1968), 494-497.
60. A. R. Marder and G. Krauss, Trans. ASM, 62 (1967), 651-660.
61. N. C. Low, P. R. Howell, and D. V. Edmonds, Metal Sci., Sept. (1979), 507-515.
62. W. J. Harris and M. Cohen, Trans. AIME, 180 (1949), 447-470.
63. O. P. Maximova and É. I. Éstrin, Fiz. Met. Metalloved, 9 (1960), 426-435.
64. G. V. Kurdjumov and G. Sachs, Zeit. für Phys., 64 (1930), 325-343.
65. Z. Nishiyama, Sci. Rep. Tohoku Univ., 23 (1934), 637-664.
66. G. Wassermann, Mitt. K-W-I, Eisenforsch., 17 (1935), 149-155.
67. A. B. Greninger and A. R. Troiano, Metals Trans., 185 (1949), 590-594.
68. M. S. Wechsler, D. S. Lieberman, and T. A. Read, Trans. AIME (JOM), 197 (1953), 1503-1515.

69. J. S. Bowles and J. K. Mackenzie, *Acta Met.*, 2 (1954);  
I: 130-137, II: 138-147, III: 224-234.
70. B. A. Bilby and F. C. Frank, *Acta Met.*, 8 (1960), 239-402.
71. A. G. Crocker and B. A. Bilby, *Acta Met.*, 9 (1961), 678-688.
72. D. S. Lieberman, "Phase Transformations," ASM (1968), Ch. 1, 1-58.
73. H. Knapp and U. Dehlinger, *Acta Met.*, 4 (1955), 289-297.
74. C. L. Magee, "Phase Transformations," ASM (1968), Ch. 3, 115-155.
75. G. B. Olson and M. Cohen, "A Perspective on Martensite Nucleation," *Ann. Rev. Mat. Sci.* 11 (1981), 1-30.
76. C. Zener, *Trans. AIME*, 167 (1946), 550-595; *Phy. Rev.*, 74 (1948), 639-650.
77. H. Beisswenger and E. Scheil, *Arch. Eisenhüttenwes*, 27 (1956), 413-420.
78. J. C. Fisher, J. H. Hollomon, and D. Turnbull, *Metals Trans.*, 185 (1949), 691-700.
79. A. R. Entwistle, *Met. Trans.*, 2 (1971), 2395-2407.
80. T. Swan and G. Krauss, *Met. Trans.*, 7A (1976), 41-48.
81. K. J. Irvine and F. B. Pickering, *JISI*, 196 (1960), 66-81.
82. J. S. Pascover and S. V. Radcliffe, *Trans. AIME*, 242 (1968), 673-682.
83. G. R. Speich and P. R. Swann, *JISI*, 201 (1965), 480-485.



84. J. M. Chilton, C. J. Barton, and G. R. Speich, *JISI*, 206 (1970), 184-193.
85. J. D. Bolton and E. R. Petty, *Metal Sci.*, 9 (1975), 166-170.
86. D. S. Sarma, J. A. Whiteman, and J. H. Woodhead, *Metal Sci.*, Nov. (1976), 391-395.
87. T. Davenport, "Solid-Solid Phase Transformations," ASM, Pittsburgh, 1980, H. I. Aaronson and C. M. Wayman (eds), in Press.
88. B. V. Narasimha Rao, J. Y. Koo, and G. Thomas, *Proc. 33rd EMSA Conf., Claitors Publ. Div.* (1975), 30-31.
89. B. V. Narasimha Rao, M. Sarikaya, and G. Thomas, *Proc. 37th EMSA Conf., Claitors Publ. Div.* (1979), 538-539.
90. D. J. H. Cockayne, *Zeitsch. Naturforsch.*, 27 (1972), 452-460.
91. J. B. Warren, "Int. to Analytical E.M.," J. J. Hren, J. I. Goldstein, and D. C. Joy (eds), Plenum Press (1979), 369-386.
92. B. V. Narasimha Rao and G. Thomas, *Proc. ICOMAT '77, Kiev, USSR* (1978), 57-62.
93. B. V. Narasimha Rao, *Met. Trans.*, 10A (1979), 645-648.
94. K. W. Andrews, D. J. Dyson, and S. R. Keown, "Interpretations of Electron Diffraction Patterns," Hilger, London (1971).
95. P. L. Ryder and W. Pitsch, *Phil. Mag.*, 15 (1967), 437-446.

96. M. Von Heimendal, W. Bell, and G. Thomas, *J. Appl. Phys.*, 35 (1964), 3614-3620.
97. K. Wakasa, C. M. Wayman, H. Kubo, and K. Shimizu, *Scripta Met.*, 14 (1980), 261-268.
98. H. K. D. H. Bhadeshia and D. V. Edmonds, *Proc. ICOMAT '79*, Cambridge, MIT Press (1979), 28-33.
99. M. Sarikaya, B. V. Narasimha Rao, and G. Thomas, *Proc. 38th EMSA Conf.*, Claitors Publ. Div. (1980), 365-366.
100. P. M. Kelly, Private Communication (1981).
101. M. Sarikaya, *Proc. 34th EMSA Conf.*, Claitors Publ. Div. (1981), 436-437.
102. M. P. Nemirovskiy and Yu. R. Nemirovskiy, *Fiz. Met. Metalloved.*, 39, No. 4 (1975), 782-786.
103. T. V. Eterashvili, L. M. Utevskiy, and M. N. Spasskiy, *Fiz. Metal. Metalloved.*, 48, No. 4 (1979), 807-815.
104. G. Thomas and M. Sarikaya, *Proc. "Solid-Solid Phase Transformations,"* H. I. Aaranson and C. M. Wayman (eds) (1981), in press.
105. M. Sarikaya, K. E. Easterling, and G. Thomas, *Proc. EUREM, Electron Microscopy*, Vol. 1 (1980), 176-177.
106. E. R. Morgan and T. Ko, *Acta Met.*, 1 (1954), 36-48.
107. R. B. G. Yeo, *Trans. AIME*, 224 (1962), 208-215.
108. K. R. Kinsman and J. C. Shyne, *Acta Met.*, 15 (1967), 1527-1543.
109. E. P. Klier and A. R. Troiano, *Trans. AIME*, 162 (1945), 175-185.

110. G. S. Ansell, S. J. Donache, and R. W. Messler, Jr.,  
Met. Trans., 2 (1971), 2443-2449.
111. C. Zener, Trans. AIME, 185 (1949).
112. J. McMahon and G. Thomas, Proc. 3rd Int. Conf. Strength  
of Metals and Alloys, 1, Institute of Metals, London  
(1973), 180-185.
113. V. F. Zackay, E. R. Parker, and W. E. Wood, Proc. 3rd  
Int. Conf. Strength of Metal and Alloys, 1, Institute  
of Metals, London (1973), 175-179.
114. H. K. D. H. Bhadeshia and D. V. Edmonds, Metal Science,  
13 (1979), 325-330.
115. H. C. Fiedler, B. L. Averbach, and M. Cohen, Trans. ASM,  
47 (1952), 267-290.
116. S. A. Kulin, M. Cohen, and B. L. Averbach, Trans. AIME  
(JIM), 4 (1952), 661-668.
117. J. R. Patel and M. Cohen, Acta Met., 1 (1954), 1530-  
1538.
118. R. H. Richman and G. F. Bolling, Met. Trans., 2 (1971),  
2451-2462.
119. J. C. Fisher, Trans. AIME, 185 (1949), 688-693.
120. G. Thomas, Met. Trans., 9A (1978), 439-450.
121. M. Sarikaya, A. K. Jhingan, and G. Thomas, Met. Trans.  
(1982), in press.
122. P. B. Hirsh, R. Howie, R. B. Nicholson, D. W. Pashley,  
and M. J. Whelan, "E.M. of Thin Crystals," Butterworths,  
London (1965).

123. R. L. Miller, *Trans. ASM*, 57 (1964), 892; *ibid.*, 61 (1968), 592.
124. N. Zaluzec, "Int. to Analytical E.M.," J. J. Hren, J. I. Goldstein, and D. C. Joy (eds), Plenum Press (1979), 111-167.
125. R. Sinclair, R. Gronsky, and G. Thomas, *Acta Met.*, 24 (1976), 789-797.
126. J. W. Steeds, "Intr. to Analytical E.M.," J. J. Hren, J. I. Goldstein, and D. C. Joy (eds), Plenum Press (1979), 387-422.
127. D. C. Joy, *ibid.*, 223-224.
128. B. V. Narasimha Rao and G. Thomas, *Proc. 35th EMSA Conf.*, Claitors Publ. Div. (1977).
129. P. G. Self, H. K. D. H. Bhadeshia, and W. M. Stoobs, *Ultramicroscopy*, 6 (1981), 29-40.
130. O. L. Krivanek, *Proc. 38th EMSA Conf.*, Claitors Publ. Div. (1980), 86-89.
131. M. Sarikaya and O. L. Krivanek, Unpublished Research, Univ. of California, Berkeley, Spring 1980.
132. S. S. Brenner, M. K. Miller, and R. M. Fisher, *Proc. 28th IFES*, L. Swanson and A. Bell (eds), Portland (1981), 220-222.
133. P. W. Bach, J. Beyer, and C. A. Verbraak, *Scripta Met.*, 14 (1980), 205-210.
134. S. S. Brenner and J. T. McKinney, *Surface Sci.*, 23 (1970), 88-111.

135. P. J. Turner and J. M. Papazian, *Metals Sci.*, 7 (1973), 81-86.
136. E. W. Müller, "Methods of Surface Analysis," A. W. Czanderna (ed.), Elsevier, Amsterdam (1975), 329-378.
137. T. J. Wilkens, G. D. W. Smith, and D. A. Smith, *Metallography*, 7 (1974), 403-430.
138. P. M. Jones, G. M. Rackham, and J. W. Steeds, *Proc. Roy. Soc. (A)*, London, 354 (1977), 197-222.
139. W. B. Pearson, "Handbook of Lattice Spacings and Structures of Metals," Pergamon Press, New York (1958), 656.
140. C. S. Roberts, *Trans. AIME*, 197 (1953), 203-204.
141. N. Rindley, H. Stuart, and L. Zwell, *Trans. AIME*, 245 (1969), 1834-1836.
142. W. Steven and A. G. Haynes, *JISI*, 183 (1956), 349-360.
143. S. J. Barnard, G. D. W. Smith, M. Sarikaya, and G. Thomas, *Scripta Met.*, 15 (1981), 387-392.
144. M. K. Miller, P. A. Beaven, and G. D. W. Smith, *Met. Trans.*, 12A (1981), 1197-1204.
145. M. Sarikaya, G. Thomas, J. W. Steeds, S. J. Barnard, and G. D. W. Smith, *Prod. "Solid-Solid Phase Transformations,"* H. I. Aaranson and C. M. Wayman (eds), Pittsburgh, Penn. (1981), in press.

146. G. D. W. Smith, A. J. Garrat-Reed, and J. B. Vander Sande, Proc. Conf. on "Quantitative Analysis with High Spatial Resolutions," UMIST/Manchester (1981), Metal Soc., London, J. W. Arrowsmith, Ltd., Bristol. 238-249.
147. A. W. McReynolds, Jrnl. Appl. Phys., 20 (1949), 896-907.
148. B. Edmondson and T. Ko, Acta Met., 2 (1954), 235-241.
149. J. Philibert and C. Crussard, C. R. Akad. Sci., Paris, 240 (1955), 190-200.
150. K. E. Easterling and P. Swann, Acta Met., 15 (1971), 117-121.
151. C. L. Magee, Met. Trans., 2 (1971),
152. P. C. Maxwell, A. Goldberg, and J. C. Shyne, Met. Trans., 5 (1974), 1305-1318.
153. L. Kaufman, S. V. Radcliffe, and M. Cohen, "Decomposition of Austenite by Diffusional Processes," V. F. Zackay and H. I. Aaronson (eds), Interscience, New York (1962), 313-352.
154. R. F. Bunshah and R. F. Mehl, J. Met., 5 (1953), 1250-1255.
155. R. B. G. Yeo, Trans. ASM, 58 (1965), 114-115.
156. G. R. Speich and M. Cohen, Trans. AIME, 218 (1960), 1050-1059.
157. G. R. Speich, "Decomposition of Austenite by Diffusional Processes," V. F. Zackay and H. I. Aaronson (eds), Interscience, New York (1962), 353-371.

158. R. F. Goodenow and R. F. Hehemann, Discussion to above paper.
159. F. J. Schoen and W. S. Owen, *Met. Trans.*, 2 (1971), 2431-2441.
160. C. J. Smithsells, "Metals Reference Book, Vol. II, 3rd Ed., Butterworths, Washington (1962), 594.
161. G. G. Homar, "Diffusion in BCC Materials," ASM, Gathinburg (1964), 77-86.
162. R. P. Smith, *Trans. AIME*, 224 (1962), 105-111.
163. R. M. Fisher and L. S. Darken, U.S. Steel Co., Monroeville, Unpublished Research.
164. A. E. Lord and D. N. Beshers, *Acta Met.*, 14 (1966), 1659-1672.
165. M. Hillert, *Acta Met.*, 7 (1959), 653-658.
166. C. Wells, W. Batz, and R. F. Mehl, *Trans. AIME*, 188 (1950), 553-560.
167. R. P. Smith, *Acta Met.*, 1 (1953), 578-587.
168. H. K. D. H. Bhadeshia, *Metals Sci.*, 15 (1981), 477-479.
169. J. Crank, "Mathematics of Diffusion," 2nd ed., Clarendon Press, Oxford (1975), Ch. 4.
170. H. Scott, *Trans. ASM*, 22 (1934), 68-96.
171. R. Schumann, "Metallurgical Engineering," 2, Addison-Wesley (1952), 259-283.
172. M. A. Grossman, M. Asimov, and S. F. Urban, "Hardenability of Alloy Steels," ASM, Cleveland (1939), 124-146.

173. G. R. Speich, *Trans. AIME*, 245 (1969), 2553-2564.
174. R. F. Hehemann, "Phase Transformations," ASM (1970), Ch. 9, 397-432.
175. J. W. Christian, *Met. Trans.*, 13A (1982), 509-538.
176. J. W. Christian, "The Theory of Transformations in Metals and Alloys," 2nd ed., Pergamon Press, Oxford (1975), Ch. 1.
177. G. B. Olson, *Acta Met.*, 27 (1981), 1475-1484.
178. A. H. Cottrell and B. A. Bilby, *Proc. Phys. Soc.*, LXII (1948), 49-62.
179. E. G. Ramachandran and C. Dasarathy, *Acta Met.*, 8 (1960), 274-275.
180. B. Edmonson, *Acta Met.*, 5 (1957), 208-215.
181. J. R. L. Guimaraes and J. C. Shyne, *Met. Trans.*, 2 (1971), 2063-2065.
182. S. Harper, *Phys. Rev.*, 83 (1951), 709-712.
183. F. S. Ham, *Jrn. App. Phys.*, 30, No. 6 (1958), 915-926.
184. H. K. D. H. Bhadeshia, *Metal. Sci.*, April (1981), 175-177.
185. A. J. McEvily, Jr., R. H. Bush, F. W. Schaller, and D. J. Schmatz, *Trans. ASM*, 56 (1963), 753-767.
186. "The Making, Shaping and Treating of Steels," H. E. McGannon (ed.), U.S. Steel Co., 9th ed. (1971), 1101.
187. O. Johari and G. Thomas, *Trans. ASM*, 58 (1965), 563-578.



188. M. Dechamps and L. M. Brown, *Acta Met.*, 27 (1979), 1281-1291.
189. K. R. Kinsman, G. Das, and R. F. Hehemann, *Acta Met.*, 25 (1977), 359-365.
190. K. R. Kinsman, Proc. 28th EMSA Conf., Claitors Publ. Div. (1970), 520-521.
191. K. E. Easterling and H. M. Miekko-oja, *Acta Met.*, 15 (1967), 1133-1141.
192. R. F. Heheman, K. R. Kinsman, and H. I. Aaronson, *Met. Trans.*, 3 (1972), 1077-1085.
193. L. S. Darken and R. M. Fisher, "Decomposition of Austenite by Diffussional Processes," V. F. Zackay and H. I. Aaronson (eds), Interscience, New York (1962), 249-294.
194. M. Sarikaya, B. G. Steinberg, and G. Thomas, *Met. Trans.* (1982), in press.
195. "Atlas of Isothermal Transformation and Cooling Transformation Diagrams," ASM, Metals Park, Ohio (1977), 218.

This report was done with support from the Department of Energy. Any conclusions or opinions expressed in this report represent solely those of the author(s) and not necessarily those of The Regents of the University of California, the Lawrence Berkeley Laboratory or the Department of Energy.

Reference to a company or product name does not imply approval or recommendation of the product by the University of California or the U.S. Department of Energy to the exclusion of others that may be suitable.

TECHNICAL INFORMATION DEPARTMENT  
LAWRENCE BERKELEY LABORATORY  
UNIVERSITY OF CALIFORNIA  
BERKELEY, CALIFORNIA 94720